Near-Field Radiative Heat Transfer (NFRHT)– A Personal Account and its Recent Development

J.-B. Xu (许建斌)[1], and Y.-G. Ma (马云贵)[2]

[1]Department of Electronic Engineering & Materials Science and Technology Research Center, The Chinese University of Hong Kong, Shatin, NT, Hong Kong SAR, China

[2]College of Optical Science & Engineering, International Research Center of Haining Advanced Photonics, Center of Optical & Electromagnet Research, State Key Lab of Modern Optics, Zhejiang, University, Hangzhou, China

jbxu@ee.cuhk.edu.hk; yungui@zju.edu.cn

Session of Thermal Radiation: Principles, Progress, & Potentials, Photonics & Electromagnetics Research Symposium (PIERS) 2024, Chengdu, China, April 21-25, 2024

Outline

- Introduction
- History of NFRHT until 1971
- Nanotechnology in 1980's
- Revisit of NFRHT since the late 1980's
- NFRHT since 2000's
- Our recent progress
- Brief Outlook

Blackbody Radiation

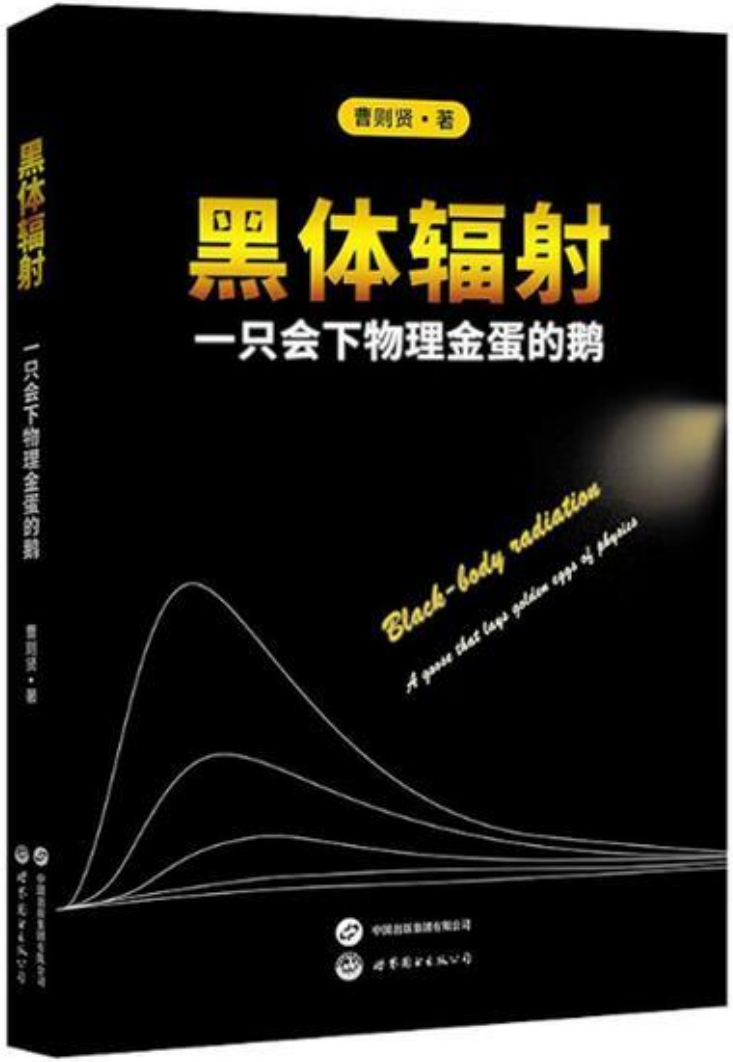

A goose that lays eggs of physics

by Cao, Zexian; 曹则贤 (2024)

Blackbody radiation is "one of the most beautiful theories in modern physics".— Hendrik Antoon Lorentz, Nobel Prize 1902, 洛伦兹

Giants behind Blackbody Radiation

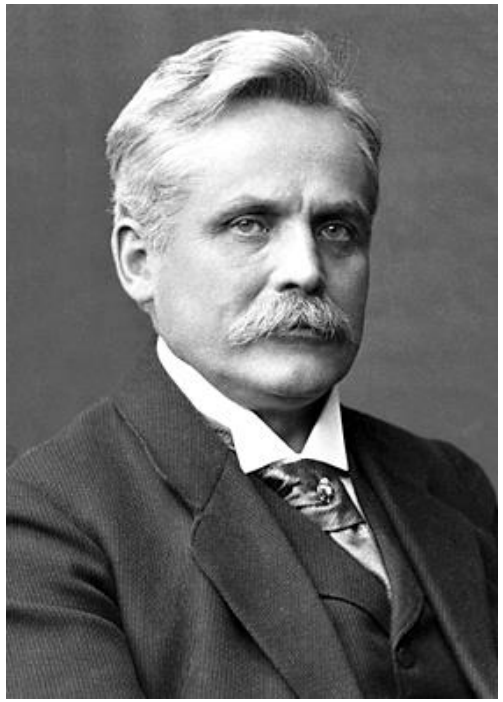

Wilhelm Wien, 1911,
Nobel Prize

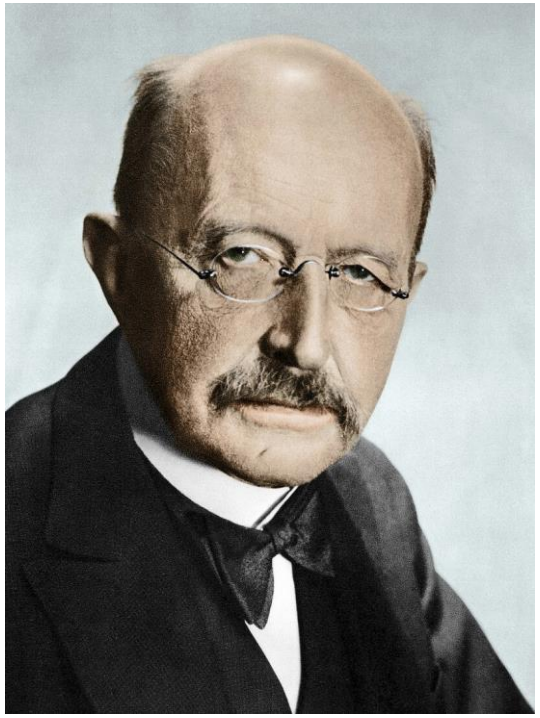

Max Karl Planck, 1918,
Nobel Prize

Max Plank, The Theory of Heat Radiation (1913), Wärmestrahlung

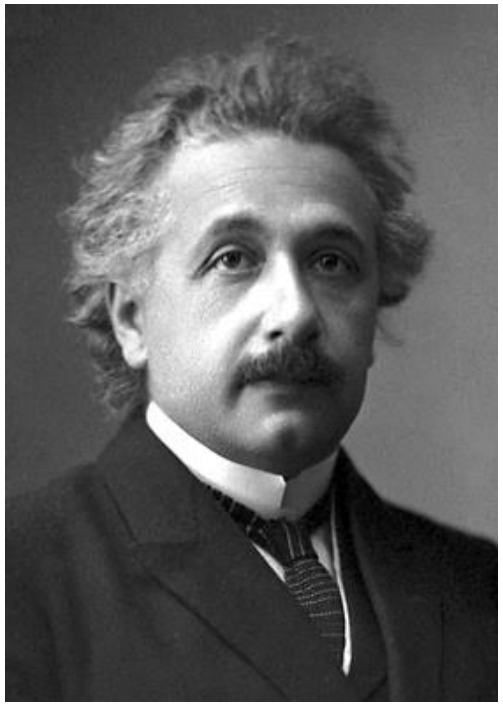

Albert Einstein, 1921,
Nobel Prize

Satyendra Nath Bose

Ideal Blackbody Radiation

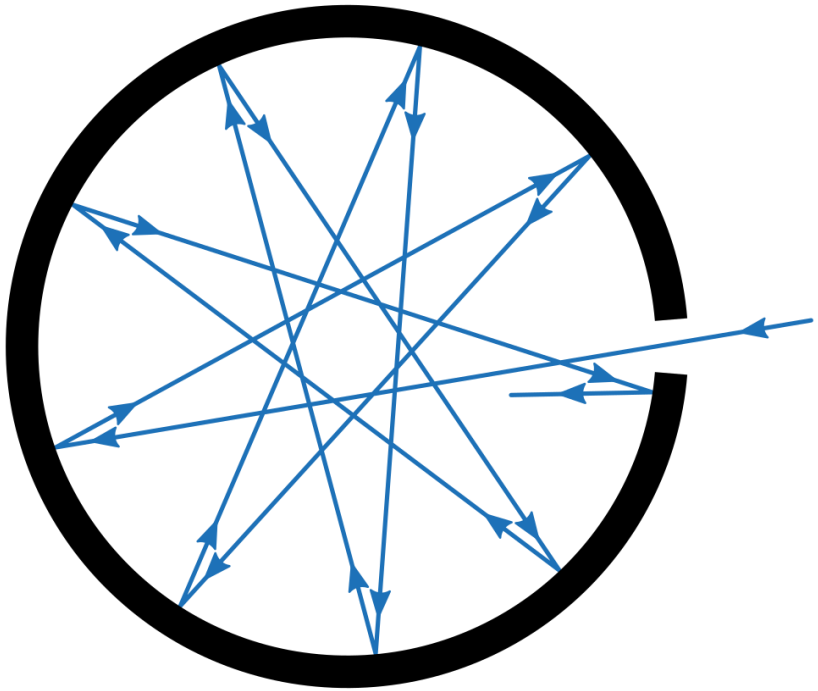

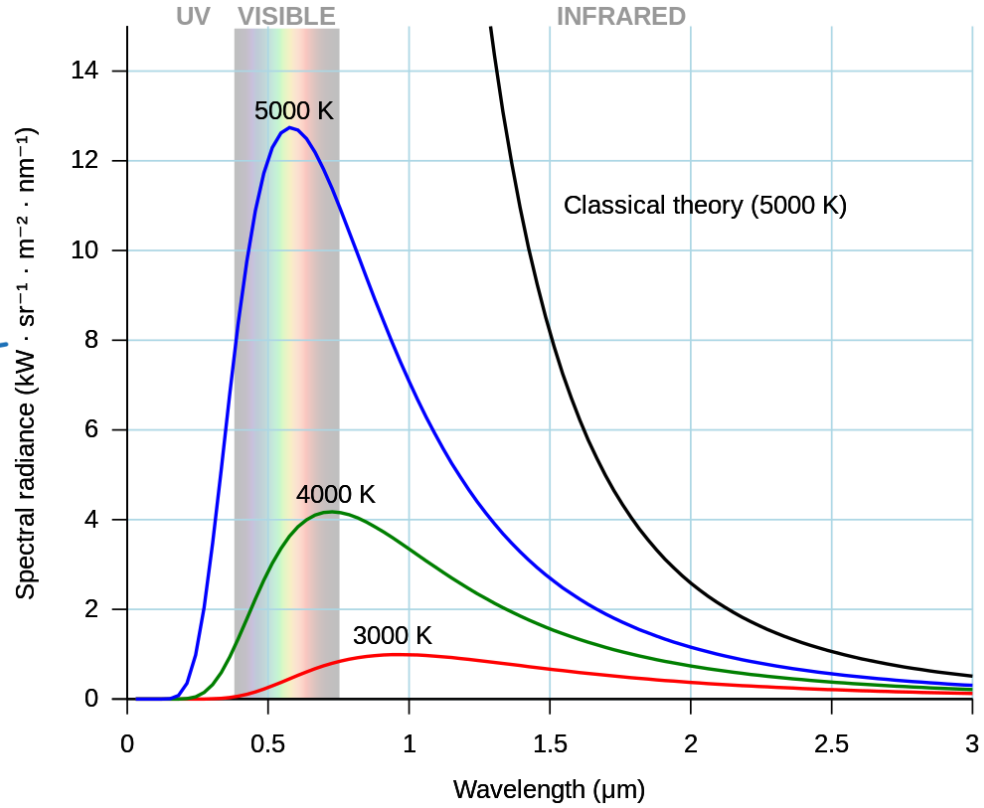

The Stefan–Boltzmann law

$$P/A = \varepsilon\sigma T^4$$

$$\sigma = \frac{2\pi^5 k^4}{15c^2h^3}$$

An approximate realization of a black body as a tiny hole in an insulated enclosure

$$\overline{E} = \frac{\sum_{n=0}^{\infty} E \cdot P(E)}{\sum_{n=0}^{\infty} P(E)} = \frac{\sum_{n=0}^{\infty} nh\nu e^{-nh\nu/kT}}{\sum_{n=0}^{\infty} e^{-nh\nu/kT}} = \frac{h\nu}{e^{h\nu/kT}-1}$$

https://en.wikipedia.org/wiki/Black_body

Figs in Near-Field Blackbody Radiation

Prof. Chang-Lin Tien, President of UC Berkely, 1990-1999

https://en.wikipedia.org/wiki/Chang-Lin_Tien

Dr. Clifford MacDonald Hargreaves, Research Staff, Philips Research Labs, 1960-2000

https://www.scribd.com/document/206202246/Philips-Research-80-Years1

https://www.jstor.org/stable/pdf/4140509.pdf

https://www.amazon.com/Philips-Stirling-Engine-Clifford-Hargreaves/dp/0444884637

No conclusion based on both theory and experiment

Early References:

1. Rytov, Sergei Mikhailovich (1953). "[Theory of Electric Fluctuations and Thermal Radiation]". Academy of Sciences Press (in Russian).
2. Emslie, A. G. (1961). "Radiation transfer by closely spaced shields".
3. Cravalho, E. G.; **Tien, C. L.;** Caren, R. P. (1967). "Effect of Small Spacings on Radiative Transfer Between Two Dielectrics". Journal of Heat Transfer. 89 (4): 351–358. doi:10.1115/1.3614396.
4. Domoto, G. A.; **Tien, C. L.** (1970). "Thick Film Analysis of Radiative Transfer Between Parallel Metallic Surfaces". Journal of Heat Transfer. 92 (3): 399–404. doi:10.1115/1.3449675.
5. Boehm, R. F.; **Tien, C. L.** (1970). "Small Spacing Analysis of Radiative Transfer Between Parallel Metallic Surfaces". Journal of Heat Transfer. 92 (3): 405–411. doi:10.1115/1.3449676.

https://en.wikipedia.org/wiki/Near-field_radiative_heat_transfer

Figs in Near-Field Blackbody Radiation

Volume 30A, number 9 PHYSICS LETTERS 29 December 1969

ANOMALOUS RADIATIVE TRANSFER BETWEEN CLOSELY-SPACED BODIES

C. M. HARGREAVES
Philips Research Laboratories, N.V. Philips' Gloeilampenfabrieken, Eindhoven, The Netherlands

Received 22 November 1969

Measurements show the existence of a proximity effect on the radiative energy transfer between two conducting plates due to the dominance of the near-field coupling over cut-off effects at small distances.

We have measured the transfer of electromagnetic energy between two parallel metal plates at different temperatures as a function of their separation, particularly when this distance becomes comparable with and smaller than the dominant wavelengths present. At such small distances there are reasons for expecting anomalous effects.

This may be argued by first considering the energy density in an *isothermal* cavity (cube of side l, temperature T). As the cavity is made smaller and smaller, the spacing of the lowest permissible frequencies and hence the energy difference between adjacent modes becomes relatively greater with respect to kT. Further, for $l \ll \hbar c\pi/kT$, it is just these lowest modes that are principally excited, so that these in fact effectively govern the energy density in the cavity. As a result, the radiation density becomes less than in a larger cavity at the same temperature and the spectrum of the radiation becomes non-Planckian. Although this must have been realized previously, it seems to have been first stated explicitly only in 1952 [1], 30 years after the analogous cut-off of lattice vibrations in crystals had been described [2,3]. The cut-off of electromagnetic waves in small cavities also forms the basis of a method of calculating the retarded Van der Waals force between metal bodies [4] and the temperature correction to this force [5].

Such cut-off effects may plausibly also give rise to a proximity effect in the radiative energy transfer between two bodies (e.g. parallel plates) at different temperatures. At first sight, by analogy with the lowered radiation density in an isothermal cavity, one might expect a decrease of the radiative transfer as the plates are brought nearer each other. However, there is also energy transfer between the plates by virtue of a "near-field" coupling: the thermally-induced fluctuation field of the charges in each plate extends somewhat above the surface and is "felt" by the charges in the other plate. The consequent movement and damping of these charges constitute a transfer of energy between the plates. It is evident that this coupling will increase as the plates are brought closer together. However, it is not a priori evident in how far these two modes of energy transfer are properly separable and, if separable, to what extent complementary.

Our measurements were made with two optically-flat surfaces A, B, coated with chromium about 1000 Å thick. The separation and parallelism of the plates could be finely adjusted by means of piezo-electric ceramic pillars. The

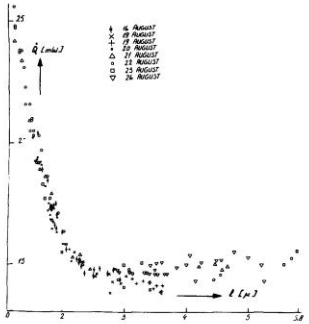

Fig. 1.

First paper appeared on sub-thermal wavelength, 1969, but with a few uncertainties

https://www.sciencedirect.com/science/article/pii/0375960169902643

Volume 30A, number 9 PHYSICS LETTERS 29 December 1969

apparatus was mounted in a vessel evacuated to $< 10^{-5}$ Torr. A guard-enclosure surrounding one of the plates (A) and held at the same temperature ensured that, of the energy supplied to A, nearly all was transferred by radiation to the plate B. Losses via supports and wires amounted to ~ 1%. The measurements were carried out by holding the temperature T_B constant and recording the power that had to be supplied to A to keep T_A constant, for various values of the plate separation. This distance was determined from capacitance measurements. The chromium film on plate B (glass) is divided into three sectors, permitting a check on the parallelism both capacitively and from the interference colours (between the sectors). Direct contact or contact via a dust particle is betrayed by a rise in the loss angle of the capacitance and also by abnormal changes in interference colour in response to the controls.

For $T \approx 300^{\circ}$K, $\hbar c\pi/kT \approx 25\ \mu$, so anomalous effects should be expected at distances of a few microns. At distances of this order, spurious effects can be excluded only when the optical flats are brought together in a state of extreme cleanliness. The results of about 160 measurements, with $T_A = 323^{\circ}$K and $T_B = 306^{\circ}$K, are shown in the figure. The reproducibility both from day to day and between measurements at a given distance after repeated separation of the plates leads us to believe that the curve represents a true proximity effect. The absence of a clear minimum in the curve suggests that the two modes of energy transfer may indeed be complementary until, as the separation is reduced, the near-field coupling becomes dominant. Measurements at lower temperature (near 77°K) are in preparation; here the proximity effect should be observable from about 8μ.

The only published theoretical work relating to this problem is that of Rytov [6]. He has studied the spectral energy density in a plane-parallel cavity as a function of the wall separation. For a non-isothermal cavity, in the special case that one wall is a nearly-perfect reflector, Rytov gives expressions for the energy transfer by a single Fourier component of the spectrum. The total energy transfer should therefore be calculable by numerical methods but the theory as it stands cannot be extended to the case of completely arbitrary walls. Mention should also be made of a paper by Olivei [7] in which a related problem - energy transfer by wave penetration at a dielectric boundary - is treated by a classical optics approach.

References

1. D. Bijl, Phil. Mag. 43 (1952) 1342.
2. M. Planck, Theorie der Wärmestrahlung, 4th edition, (J. A. Barth, Leipzig 1921), p. 218.
3. C. Schaeffer, Z. f. Physik, 7 (1921) 287.
4. H. B. G. Casimir, Proc. Kon. Ned. Akad. Wetenschappen 51 (1948) 793.
5. F. Sauer, Dissertation Göttingen 1962; the results are summarized in Proc. Kon. Ned. Akad. Wetenschappen B68 (1965) 231.
6. S. Rytov, Theory of electric noise and thermal radiation, (Publishing House Academy of Sciences, USSR, 1953). Translation by H. Erkku.
7. A. Olivei, Rev. de Physique appl. 3 (1968) 225.

* * * * *

https://catalog.crl.edu/Search/Results?lookfor=%22Philips+research+reports.+Supplements%2C%22&type=Series

Full paper appeared in Philips Research Lab Report, 1973, p. 1-80

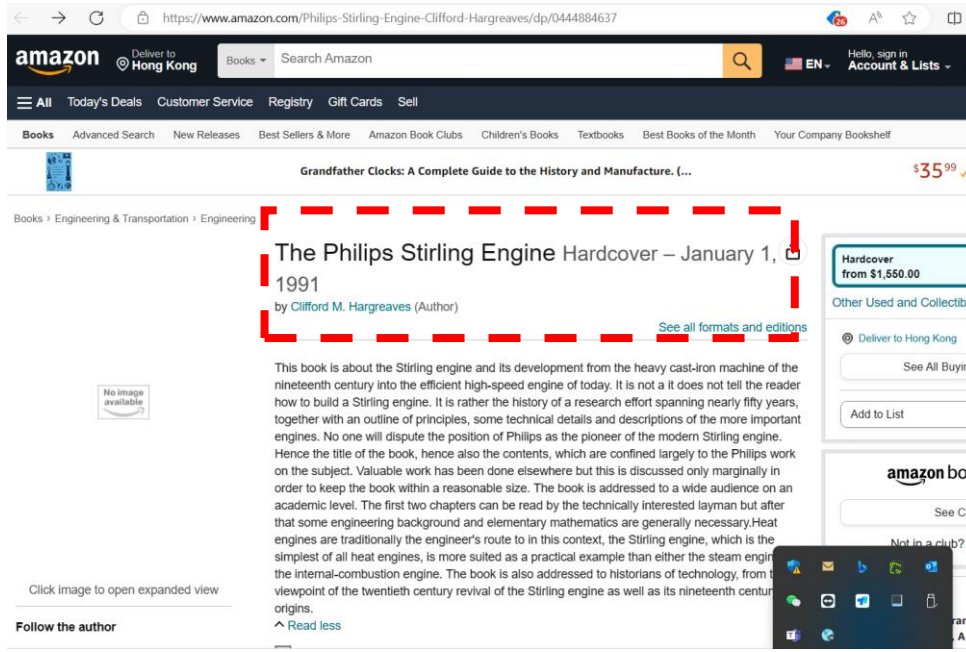

C. M. Hargreaves was more engaged in R&D of Stirling Engine

https://www.amazon.com/Philips-Stirling-Engine-Clifford-Hargreaves/dp/0444884637

D. Polder & M. Van Hove's Prediction

First theoretically conclusive prediction on NFRHT

Choi for suggesting this problem. Thanks are also due to Professor Choi, Professor John Hernandes, Professor K. S. Dy, and Dr. N. D. Lang for reading the manuscript and making helpful comments.

*Research supported by the National Aeronautics and Space Administration through its University Sustaining Program.
†Present address: Public Interest Research Group, Washington, D. C. 20005.

[1]E. Wigner and J. Bardeen, Phys. Rev. 48, 84 (1935); J. Bardeen, *ibid.* 49, 653 (1936).
[2]H. B. Huntington, Phys. Rev. 81, 1035 (1951).
[3]N. D. Lang and W. Kohn, Phys. Rev. B 1, 4555 (1970); N. D. Lang, Solid State Commun. 7, 1047 (1969); N. D. Lang and W. Kohn, Phys. Rev. B 3, 1215 (1971).

PHYSICAL REVIEW B VOLUME 4, NUMBER 10 15 NOVEMBER 1971

Theory of Radiative Heat Transfer between Closely Spaced Bodies

D. Polder and M. Van Hove
Philips Research Laboratories, N. V. Philips' Gloeilampenfabrieken, Eindhoven, Netherlands
(Received 28 January 1971)

A general formalism is developed by means of which the radiative heat transfer between macroscopic bodies of arbitrary dispersive and absorptive dielectric properties can be evaluated. The general formalism is applied to the heat transfer across a vacuum gap between two identical semi-infinite bodies at different temperatures. The peculiarities arising when the gap width is of the order of, or smaller than, the dominant thermal radiation wavelengths are studied and quantitatively evaluated for the case of two metal bodies. The predicted strong increase with diminishing gap width is in qualitative agreement with experimental results.

I. INTRODUCTION

Consider a set of bodies of macroscopic dimensions with arbitrary dispersive and absorptive dielectric properties. These bodies emit thermal radiation depending on the local temperature. With the aid of the fluctuation-dissipation theorem and electromagnetic theory we shall derive a formula for the heat flux at an arbitrary point due to the radiating bodies. Integration of this heat flux over a closed surface gives the net power dissipated in the absorbing matter contained in the enclosed volume.

By this method we intend to determine and discuss the net heat transfer between two semi-infinite absorbing bodies with arbitrary dielectric properties at slightly different temperatures separated by vacuum of width d. The heat transfer between closely spaced bodies differs from that when the spacing is large for two reasons. Firstly, when the separation d is comparable to, or smaller than, the dominant vacuum wavelengths at the temperatures considered, interference effects must be expected in the waves multiply reflected between the two surfaces. Secondly, the evanescent fields normally present in thermal equilibrium at the outer surface of each body can reach over to the opposite body and transfer energy if the distance is sufficiently small. As will be explicitly shown for metal bodies, the latter mechanism of energy transfer is the dominant one for small distances, giving rise to a strong increase of heat transfer with decreasing d.

Rytov has developed a treatment of problems of this kind. Rytov's work and ours differ in the following respects. One difference is merely formal: Rytov starts from random thermal exciting electromagnetic fields, for which he writes down a correlation function, in which a constant factor C appears. In Ref. 1, C is determined *a posteriori* by reproducing Kirchhoff's law for radiation emitted into vacuum. In Ref. 2, C is obtained from Nyquist's formula, and a discussion of the zero correlation radius used by him (and by us) appears. In our work we take electric currents rather than fields as the random thermal sources and use the fluctuation-dissipation theorem to determine their statistical properties; this rather simplifies the formal treatment.

The second difference is that Rytov's study of the heat transfer across a gap is confined to the case of one semi-infinite absorbing body at temperature T separated by vacuum from an almost perfect mirror at zero temperature: The mirror is described by the approximate boundary conditions of Leontovich, which state that the magnetic fields are the same as if the mirror were perfect. In our work we study the heat transfer between two arbitrary identical semi-infinite bodies at different temperatures, while exact boundary con-

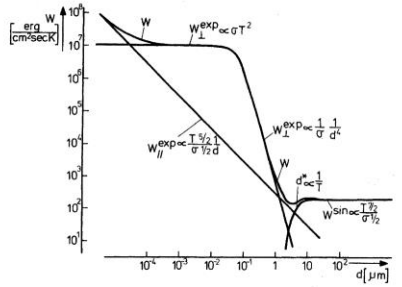

FIG. 6. Approximate integrated contributions to the net heat transfer as obtained in Sec. VII and their sum W as functions of d in the case $T = 315$ K, $\epsilon = -i4\pi\sigma\omega^{-1}$, and $\sigma = 7.0\times10^{16}$ sec^{-1}. W^{sin} has been calculated with the frequency cutoff described in the text. The T, σ, and d dependence of the various contributions and of d^* are included. Below $d = 10^{-2}$ μm = 100 Å these curves lose their physical meaningfulness, owing to electronic and atomic effects.

$$\omega_{min} \approx (4\pi)^{-1} c^2 \sigma^{-1} d^{-2} \quad . \tag{38}$$

To integrate these results over frequency we specify that $\epsilon = -i4\pi\sigma/\omega$. The various regions of validity of the expressions obtained will be described by comparing d to the dominant wavelength λ_{max} defined by Eq. (29).

For $d \ll |\epsilon(\lambda_{max})|^{1/2}\lambda_{max}/(2\pi)$, since

$$\int_0^\infty dx\, x^{7/2} e^x/(e^x-1)^2 = 13.1 \ ,$$

Eqs. (31) and (34) yield

$$W_\parallel^{exp} \approx 0.156\, k^{7/2} c^{-1} \hbar^{-5/2} \tau^{5/2} \sigma^{-1/2} d^{-1}$$

$$\approx 4.46\, T^{5/2} \sigma^{-1/2} d^{-1} \ . \tag{39}$$

Equation (35) gives a heat transfer negligible with respect to W^{sin}.

For

$$d \ll |\epsilon(\lambda_{max})|^{-1/2}\lambda_{max}/(2\pi) \ ,$$

the $\perp$ polarization yields, with $\int_0^\infty dx\, x^3 e^x/(e^x-1)^2 = 7.20$,

$$W_\perp^{exp} \approx 0.574\, k^3 \hbar^{-2} c^{-2} \sigma T^2 = 1.52\times10^{-15} \sigma T^2 \ . \tag{40}$$

For

$$d \gg |\epsilon(\lambda_{max})|^{-1/2}\lambda_{max}/(2\pi)$$

we have, using Eq. (37),

$$W_\perp^{exp} \approx 7.3\times10^{-3} k c^2 \sigma^{-1} d^{-4} \times[5.6 + \ln(4\pi\, 10^{-2} k\hbar^{-1} c^{-2}) + \ln(\sigma T d^2)]$$

$$= 908 \sigma^{-1} d^{-4}[\ln(\sigma T d^2) - 20.4] \ , \tag{41}$$

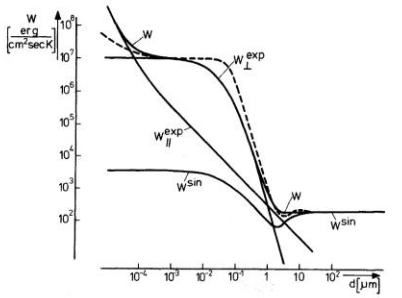

FIG. 7. Numerically integrated contributions to the net heat transfer and their sum W as functions of d for the case of Fig. 6, with (dashed curve) the total approximate result of Fig. 6 superimposed.

because

$$\int_{x_{min}}^\infty dx\, x e^x/(e^x-1)^2$$

$$\approx \int_{x_{min}}^{0.01} dx/x + \int_{0.01}^\infty dx\, x e^x/(e^x-1)^2$$

$$\approx \ln(0.01\, x_{min}^{-1}) + 5.6 \ , \tag{42}$$

where $x_{min} = \hbar\omega_{min}/kT$ [cf. Eq. (38)].

The theoretical approximate results as functions of d are represented in a specific case in Fig. 6; here $\sigma = 7.0\times10^{16}$ sec^{-1} and $T = 315$ K, so that $\lambda_{max} \approx 9.2$ μm. Notice the remarkably large contribution of W^{exp} owing to a very intense spectrum.

With the knowledge of the d, σ, and T dependence of the total heat transfer as given by the above approximations (and brought together in Fig. 6) we can, for example, predict that the dip occurring near $d = \frac{1}{4}\lambda_{max}$ will disappear if σ is chosen smaller; then also the height of the shoulder diminishes and sensibly approaches the $d \to \infty$ value; and vice versa, large conductivities favor a dip and a large ratio of shoulder height to $d \to \infty$ value.

A temperature increase will in first approximation shift the dip up along the d^{-4} slope in Fig. 6, while it reduces the ratio of shoulder height to $d \to \infty$ value.

One should in fact take into account the temperature dependence of σ (e.g., $\sigma \propto T^{-1}$), but this only influences quantitatively the features just mentioned.

Fig. 7 shows computed result based on the exact formulas in the same physical situation. These confirm the discussed expectations.

In the foregoing example, condition (28) was satisfied. We now consider a more realistic situation and try to treat the case of chromium near room temperature. In the (infrared) frequency region corresponding to such temperatures, the condition $|\epsilon| \gg 1$ is not everywhere fulfilled for chromium. Thus, the analytic approximations lose their reliability and we have to concentrate on numerical integration.

To obtain $\epsilon(\omega)$ for chromium we apply the method of curve fitting of a theoretical expression for $\epsilon(\omega)$ satisfying the Kramers-Kronig relations to experimental optical data (taken over from Ref. 6 and later measurements by these authors). The expression $\mathrm{Im}\epsilon = -4\pi\sigma\omega^{-1}$ has the free parameter σ and gives $\mathrm{Re}\epsilon$ through the Kramers-Kronig relations. But it is simpler and more realistic to use an expression provided by Drude's theory of conductivity, incorporating a low-frequency conductivity σ and a mean free flight time ω_0^{-1}, which we may consider as free parameters:

$$\mathrm{Re}\epsilon = 1 - \frac{4\pi\sigma\omega_0}{\omega^2+\omega_0^2} \ , \quad \mathrm{Im}\epsilon = -\frac{4\pi\sigma\omega_0^2}{\omega(\omega^2+\omega_0^2)} \ . \tag{43}$$

A reasonable fit to experimental data in the frequency range of interest is found for $\sigma = 3.5\times10^{16}$ sec^{-1} and $\omega_0 = 1.41\times10^{14}$ sec^{-1}. The resulting $\epsilon(\omega)$ is represented in Fig. 8, together with experimental curves and $\mathrm{Im}\epsilon = -4\pi\sigma\omega^{-1}$ as used in the preceding example. And Fig. 9 shows the corresponding heat transfer W.

Comparison of Figs. 9 and 7 shows at once that the $d \to \infty$ value has diminished rather than been augmented, although $|\epsilon|$ has diminished: The reason for this lies in the fact that now the argument of ϵ has changed markedly in the short-wavelength region. Nevertheless, the curve of Fig. 9 has the same general characteristic shape as that of Fig. 7; in particular, the distance at which the small-separation effects appear has not changed, being in first approximation only dependent on temperature.

In Ref. 5, Hargreaves published measurements of radiative heat transfer between flat chromium bodies with a mean temperature of $T \approx 315$ K in the separation range $1 < d < 10$ μm. We find very good agreement with experiment as regards the shape of the curves and the critical distance below which the small-separation effect becomes noticeable.

The absolute values of the heat currents, though of the same order of magnitude, do not coincide, however, not even for $d \to \infty$: It appears after examination of more recent, as yet unpublished, measurements by the same author that the discrepancy lies in a difference between bulk chromium (on which our calculations are based) and the chromium layers used in the experiments.

[4]S. M. Rytov, *Theory of Electric Fluctuations and Thermal Radiation* (Air Force Cambridge Research Center, Bedford, Mass., 1959), AFCRC-TR-59-162.
[5]M. A. Leontovich and S. M. Rytov, Zh. Eksperim. i Teor. Fiz. 23, 246 (1952).
[6]E. G. Cravalho, C. L. Tien, and R. P. Caren, Trans. ASME Ser. C 89, 351 (1967).
[5]C. M. Hargreaves, Phys. Letters 30A, 491 (1969).
ties and Electronic Structure of Metals and Alloys, edited by F. Abelés (North-Holland, Amsterdam, 1966), p. 196; and J. Opt. Soc. Am. 56, 1137 (1966).

https://journals-aps-org.easyaccess1.lib.cuhk.edu.hk/prb/pdf/10.1103/PhysRevB.4.3303

Figs in Near-Field Blackbody Radiation

Prof. Hendrik Casimir

https://en.wikipedia.org/wiki/Hendrik_Casimir

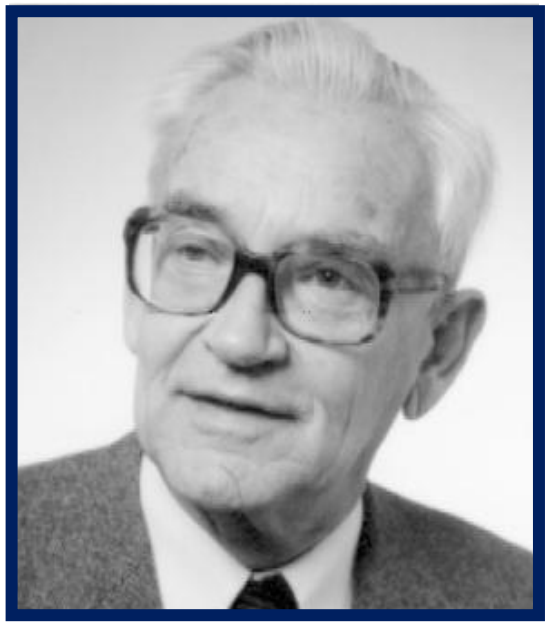

Prof. Dirk Polder

https://en.wikipedia.org/wiki/Dirk_Polder

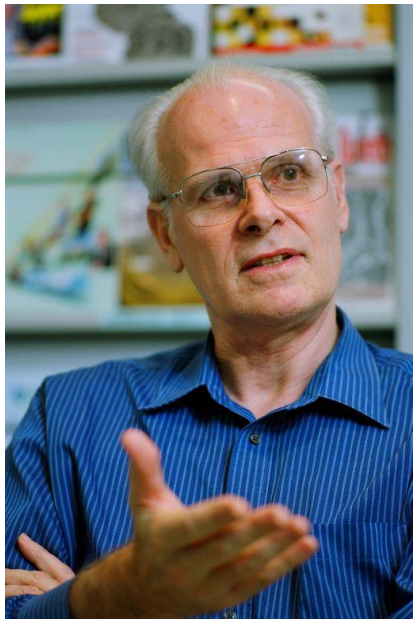

Prof. Michel A. Van Hove, HKBU

https://www.icts.hkbu.edu.hk/vanhove

Prof. Léon Van Hove, CERN

https://en.wikipedia.org/wiki/L%C3%A9on_Van_Hove

Pioneers of Nanotechnology

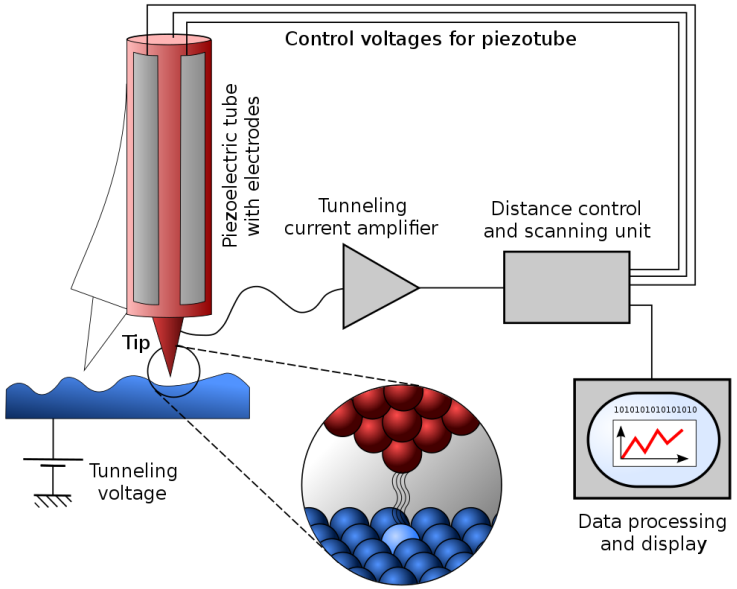

Schematic view of an STM

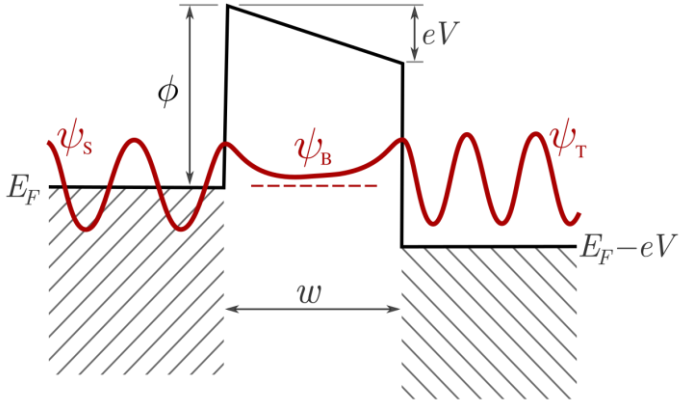

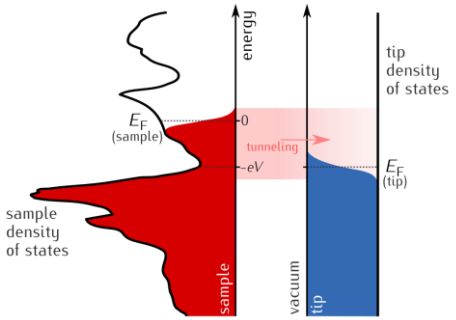

Gerd Binnig and Heinrich Rohrer with the scanning tunneling microscope (STM), Nobel Laureate 1986

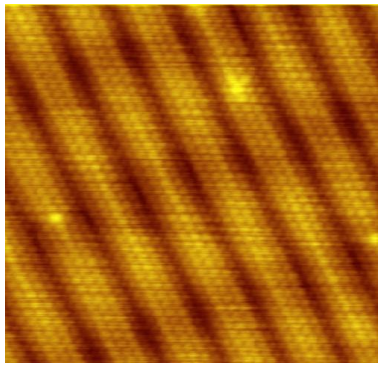

Atomic image of reconstruction on a clean (100) surface of gold

Electronic Feedback Control System is technically the key for SPMs.

https://www.ibm.com/history/gerd-binnig

https://en.wikipedia.org/wiki/Scanning_tunneling_microscope#

2016 Reunion at Kavli Prize

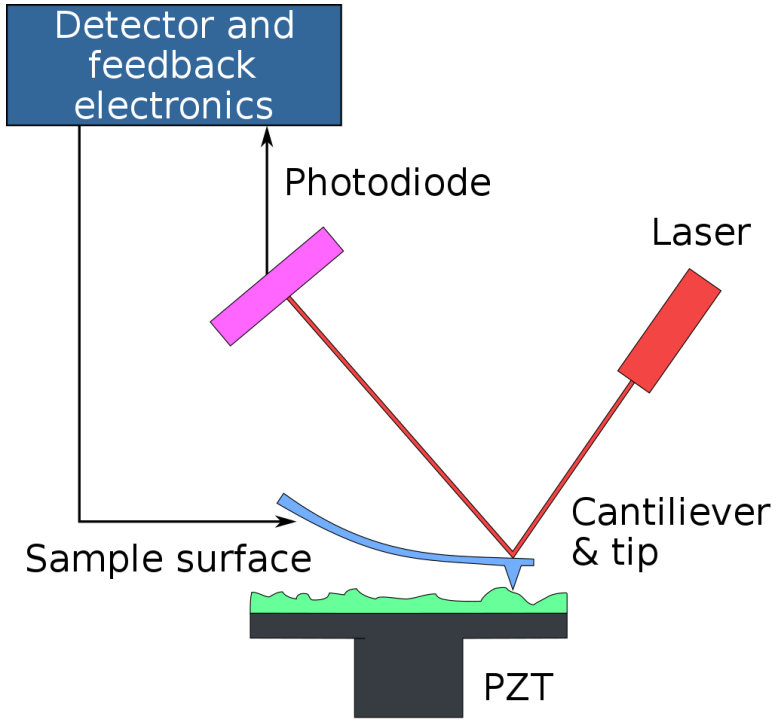

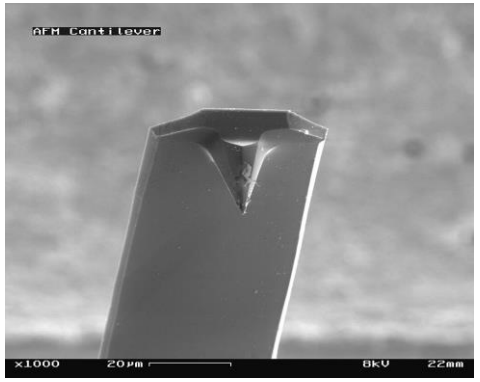

https://en.wikipedia.org/wiki/Atomic_force_microscopy

Commercialization

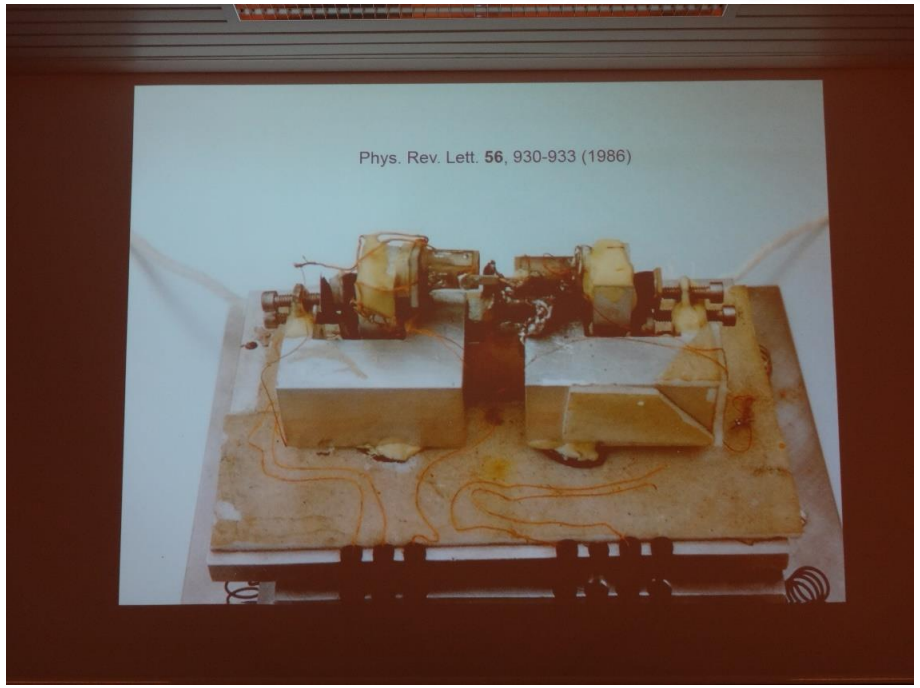

2016 International Scanning Probe Microscopy Conference, Grindelwald, Switzerland, June 12-15, 2016
First AFM, photo by Ch. Gerber

Special session to celebrate 30th Anniversary of AFM Invention, June 12-15, 2016
Professor Emeritus Virgil Elings, Founder of Digital Instruments, then Veccco, now Brucker

Research Links

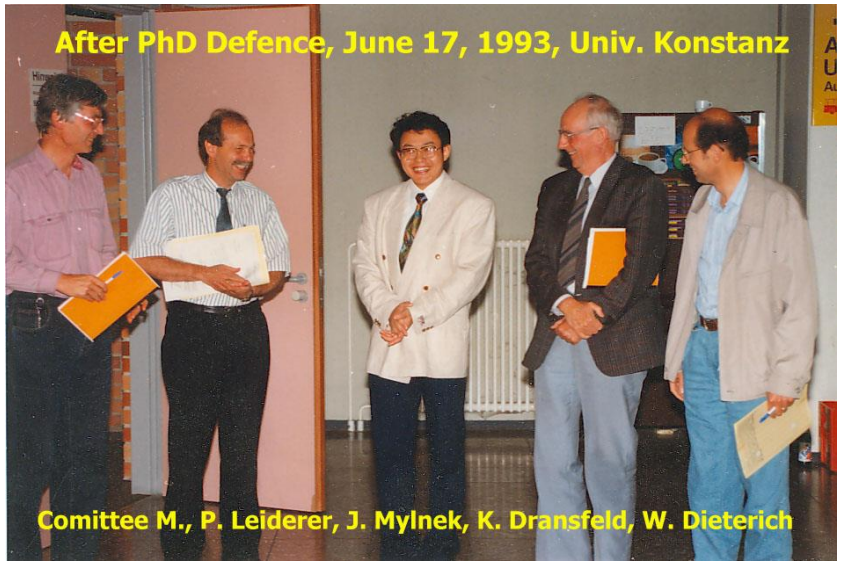

Doctor Exam, Jürgen Mlynek (Chair), now Chairman of the Strategic Advisory Board of the European Quantum Technology Flagship Initiative; Universität Konstanz (June 1993)

University of Konstanz (an Elite University), Germany (1988-1993, under supervision of Prof. Dr. Klaus Dransfeld)

Nanoscience and Nanotechnology:
STM/AFM; C_{60}; Nano-phase Materials, QDs (Louis E. Brus), superlattices, clusters, nanowires, etc.

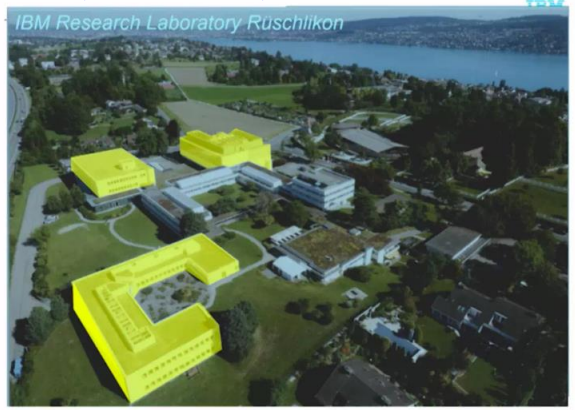

IBM Zurich Research Lab, Switzerland

Yellow Buildings: The Binning and Rohrer Nanotechnology Center, 17 May, 2011, operated by ETH and IBM

https://www.youtube.com/watch?v=dtSt04tYT9E

Trailblazers of Nanotechnology

Dr. H. K. Wickramasighe's group (IBM, Yorktown Heights) developed various types of SPM, with ultra-high sensitive detection technique (hydrodyne optics), SThM, KPFM, EFM, dynamic AFM, s-SNOM, SIR-M, etc., in 1980's-1990s. Prior to SPM, he was engaged in ultrasonic and photoacoustic microscopies with Eric Ash and Calvin F Quate, in Imperial College and Stanford..

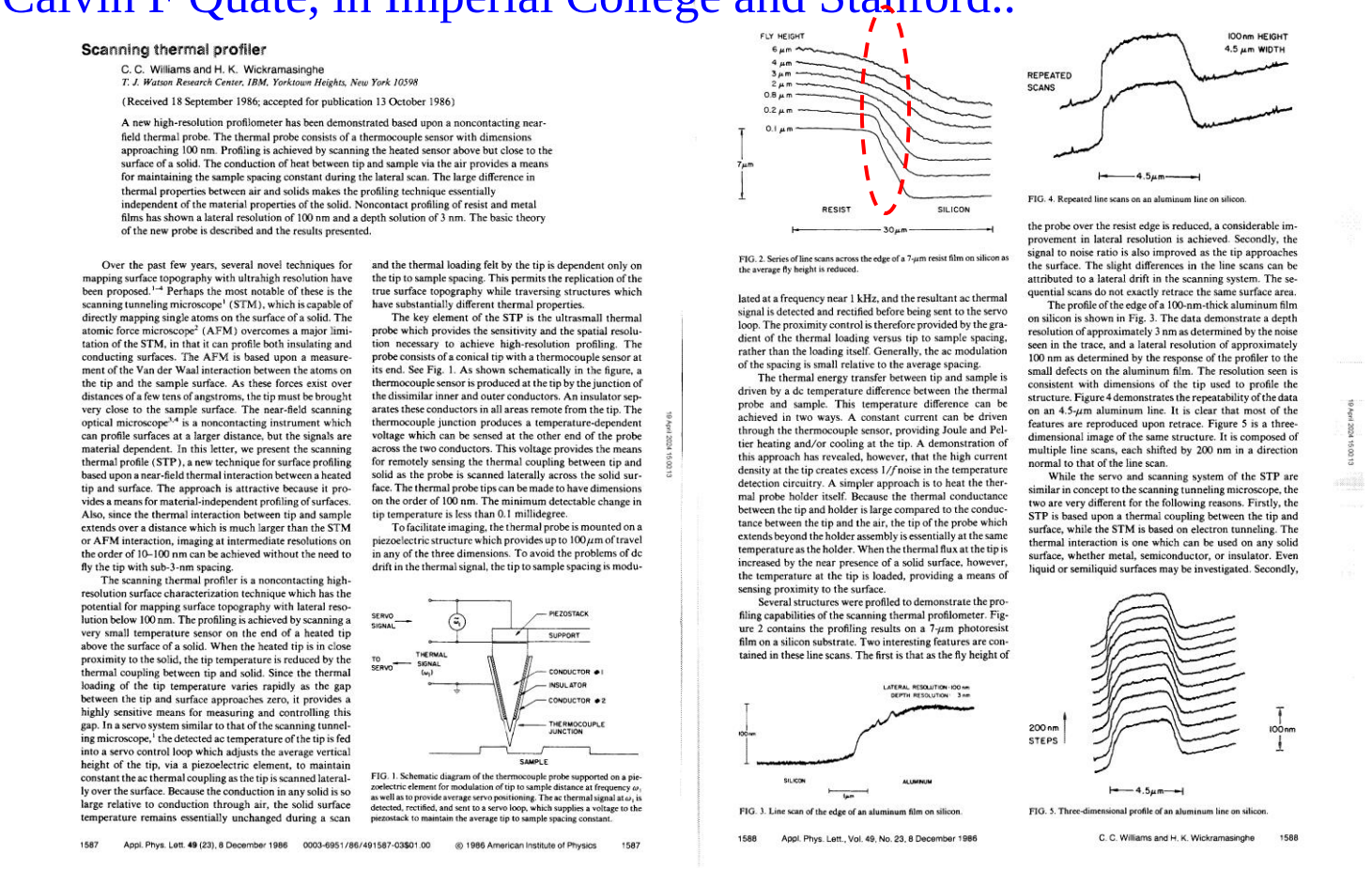

Scanning thermal profiler

C. C. Williams and H. K. Wickramasinghe
T. J. Watson Research Center, IBM, Yorktown Heights, New York 10598

(Received 18 September 1986; accepted for publication 13 October 1986)

A new high-resolution profilometer has been demonstrated based upon a noncontacting near-field thermal probe. The thermal probe consists of a thermocouple sensor with dimensions approaching 100 nm. Profiling is achieved by scanning the heated sensor above but close to the surface of a solid. The conduction of heat between tip and sample via the air provides a means for maintaining the sample spacing constant during the lateral scan. The large difference in thermal properties between air and solids makes the profiling technique essentially independent of the material properties of the solid. Noncontact profiling of resist and metal films has shown a lateral resolution of 100 nm and a depth solution of 3 nm. The basic theory of the new probe is described and the results presented.

Over the past few years, several novel techniques for mapping surface topography with ultrahigh resolution have been proposed.[1-4] Perhaps the most notable of these is the scanning tunneling microscope[1] (STM), which is capable of directly mapping single atoms on the surface of a solid. The atomic force microscope[2] (AFM) overcomes a major limitation of the STM, in that it can profile both insulating and conducting surfaces. The AFM is based upon a measurement of the Van der Waal interaction between the atoms on the tip and the sample surface. As these forces exist over distances of a few tens of angstroms, the tip must be brought very close to the sample surface. The near-field scanning optical microscope[3,4] is a noncontacting instrument which can profile surfaces at a larger distance, but the signals are material dependent. In this letter, we present the scanning thermal profile (STP), a new technique for surface profiling based upon a near-field thermal interaction between a heated tip and surface. The approach is attractive because it provides a means for material-independent profiling of surfaces. Also, since the thermal interaction between tip and sample extends over a distance which is much larger than the STM or AFM interaction, imaging at intermediate resolutions on the order of 10–100 nm can be achieved without the need to fly the tip with sub-3-nm spacing.

The scanning thermal profiler is a noncontacting high-resolution surface characterization technique which has the potential for mapping surface topography with lateral resolution below 100 nm. The profiling is achieved by scanning a very small temperature sensor on the end of a heated tip above the surface of a solid. When the heated tip is in close proximity to the solid, the tip temperature is reduced by the thermal coupling between tip and solid. Since the thermal loading of the tip temperature varies rapidly as the gap between the tip and surface approaches zero, it provides a highly sensitive means for measuring and controlling this gap. In a servo system similar to that of the scanning tunneling microscope,[1] the detected ac temperature of the tip is fed into a servo control loop which adjusts the average vertical height of the tip, via a piezoelectric element, to maintain constant the ac thermal coupling as the tip is scanned laterally over the surface. Because the conduction in any solid is so large relative to conduction through air, the solid surface temperature remains essentially unchanged during a scan and the thermal loading felt by the tip is dependent only on the tip to sample spacing. This permits the replication of the true surface topography while traversing structures which have substantially different thermal properties.

The key element of the STP is the ultrasmall thermal probe which provides the sensitivity and the spatial resolution necessary to achieve high-resolution profiling. The probe consists of a conical tip with a thermocouple sensor at its end. See Fig. 1. As shown schematically in the figure, a thermocouple sensor is produced at the tip by the junction of the dissimilar inner and outer conductors. An insulator separates these conductors in all areas remote from the tip. The thermocouple junction produces a temperature-dependent voltage which can be sensed at the other end of the probe across the two conductors. This voltage provides the means for remotely sensing the thermal coupling between tip and solid as the probe is scanned laterally across the solid surface. The thermal probe tips can be made to have dimensions on the order of 100 nm. The minimum detectable change in tip temperature is less than 0.1 millidegree.

To facilitate imaging, the thermal probe is mounted on a piezoelectric structure which provides up to 100 μm of travel in any of the three dimensions. To avoid the problems of dc drift in the thermal signal, the tip to sample spacing is modulated at a frequency near 1 kHz, and the resultant ac thermal signal is detected and rectified before being sent to the servo loop. The proximity control is therefore provided by the gradient of the thermal loading versus tip to sample spacing, rather than the loading itself. Generally, the ac modulation of the spacing is small relative to the average spacing.

FIG. 1. Schematic diagram of the thermocouple probe supported on a piezoelectric element for modulation of tip to sample distance at frequency ω_1 as well as to provide average servo positioning. The ac thermal signal at ω_1 is detected, rectified, and sent to a servo loop, which supplies a voltage to the piezostack to maintain the average tip to sample spacing constant.

FIG. 2. Series of line scans across the edge of a 7-μm resist film on silicon as the average fly height is reduced.

FIG. 3. Line scan of the edge of an aluminum film on silicon.

Several structures were profiled to demonstrate the profiling capabilities of the scanning thermal profilometer. Figure 2 contains the profiling results on a 7-μm photoresist film on a silicon substrate. Two interesting features are contained in these line scans. The first is that as the fly height of the probe over the resist edge is reduced, a considerable improvement in lateral resolution is achieved. Secondly, the signal to noise ratio is also improved as the tip approaches the surface. The slight differences in the line scans can be attributed to a lateral drift in the scanning system. The sequential scans do not exactly retrace the same surface area.

The profile of the edge of a 100-nm-thick aluminum film on silicon is shown in Fig. 3. The data demonstrate a depth resolution of approximately 3 nm as determined by the noise seen in the trace, and a lateral resolution of approximately 100 nm as determined by the response of the profiler to the small defects on the aluminum film. The resolution seen is consistent with dimensions of the tip used to profile the structure. Figure 4 demonstrates the repeatability of the data on an 4.5-μm aluminum line. It is clear that most of the features are reproduced upon retrace. Figure 5 is a three-dimensional image of the same structure. It is composed of multiple line scans, each shifted by 200 nm in a direction normal to that of the line scan.

While the servo and scanning system of the STP are similar in concept to the scanning tunneling microscope, the two are very different for the following reasons. Firstly, the STP is based upon a thermal coupling between the tip and surface, while the STM is based on electron tunneling. The thermal interaction is one which can be used on any solid surface, whether metal, semiconductor, or insulator. Even liquid or semiliquid surfaces may be investigated. Secondly,

FIG. 4. Repeated line scans on an aluminum line on silicon.

FIG. 5. Three-dimensional profile of an aluminum line on silicon.

conduction through air makes possible the profiling of surfaces without dependence upon material properties. This is the result of the large difference in thermal properties between air and any solid or liquid. Thirdly, the thermal interaction can be sensed over distances equal to the desired lateral resolution; i.e., it is not necessary to fly the tip at 1 nm when the desired lateral resolution is on the order of 10 or 100 nm. These properties make the STP look attractive for profiling applications. Such applications include microelectronic metrology, biological cell profiling, and the surface characterization of materials.

We would like to acknowledge the help of Chris Jahnes and Jerry Cuomo in the production of the thermocouple tips and of Robert Jackson and Don Merte for their help with the scanning mechanics.

[1]G. Binnig, H. Rohrer, Ch. Gerber, and E. Weibel, Phys. Rev. Lett. **49**, 57 (1982).
[2]G. Binnig, C. F. Quate, and Ch. Gerber, Phys. Rev. Lett. **56**, 930 (1986).
[3]A. Lewis, M. Isaacson, A. Muray, and A. Harootunian, Biophys. J. **41**, 405A (1983).
[4]D. W. Pohl, W. Denk, and M. Lanz, Appl. Phys. Lett. **44**, 651 (1984).

K. Dransfeld and J. Xu, Journal of Microscopy 152, 35-42 (1988), **analysis of heat transfer across the tip-sample spacing. The heat transfer via the air conduction may not be dominated.**

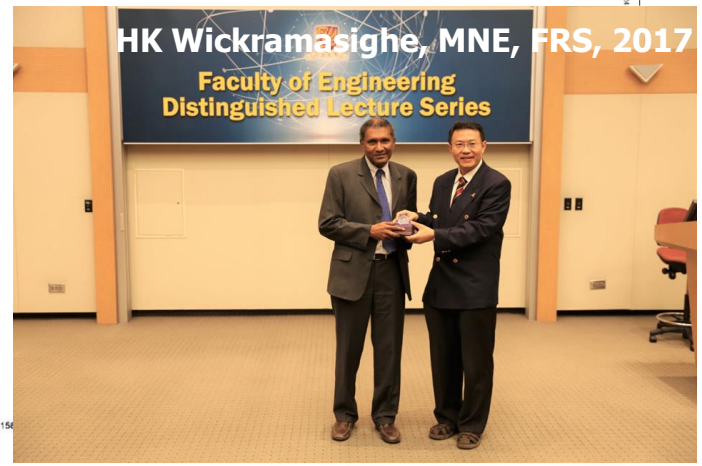

https://en.wikipedia.org/wiki/Scanning_probe_microscopy

Link of NFRHT with SPM in sub-μm

First experimental attempt to NFRHT in sub-μm, in 1990

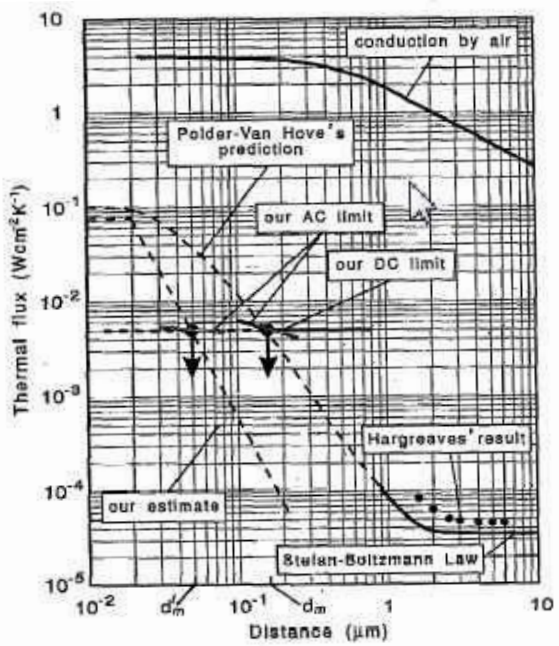

FIG. 2. Distance dependence of thermal flux between two metallic surfaces at room temperature. Under atmospheric pressure, heat conduction by air accounts for the heat transfer. Under vacuum conditions, radiative heat transfer dominates. For $d>3$ μm, the radiative heat transfer is nearly independent of d (Stefan–Boltzmann law). For $d<3$ μm, the theory predicts a strong distance dependence. Hargreaves obtained experimental values of the heat transfer at distances between 1.5 and 6 μm. From our measurements at small distances, an upper limit of heat transfer is indicated by the horizontal lines and the oblique lines. Any thermal coupling above these lines should be detectable when $d > d_m$.

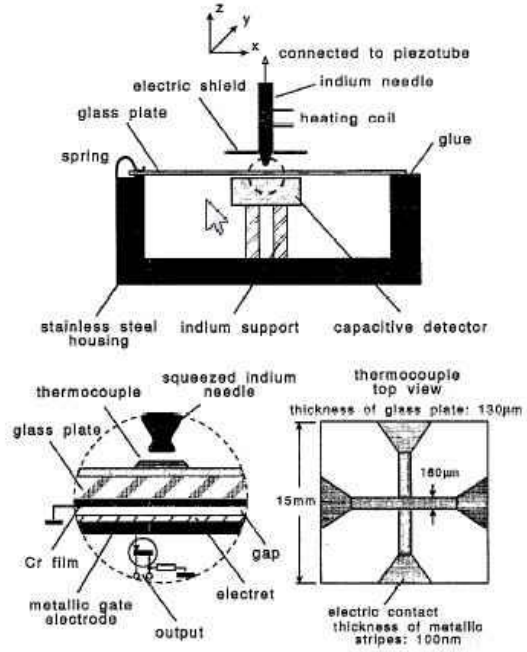

FIG. 5. Experimental setup based on a STM head. The vacuum gap was formed by a squeezed needle and a planar thermocouple. The capacitive force sensor was used to detect mechanical contact between the needle and the thermocouple.

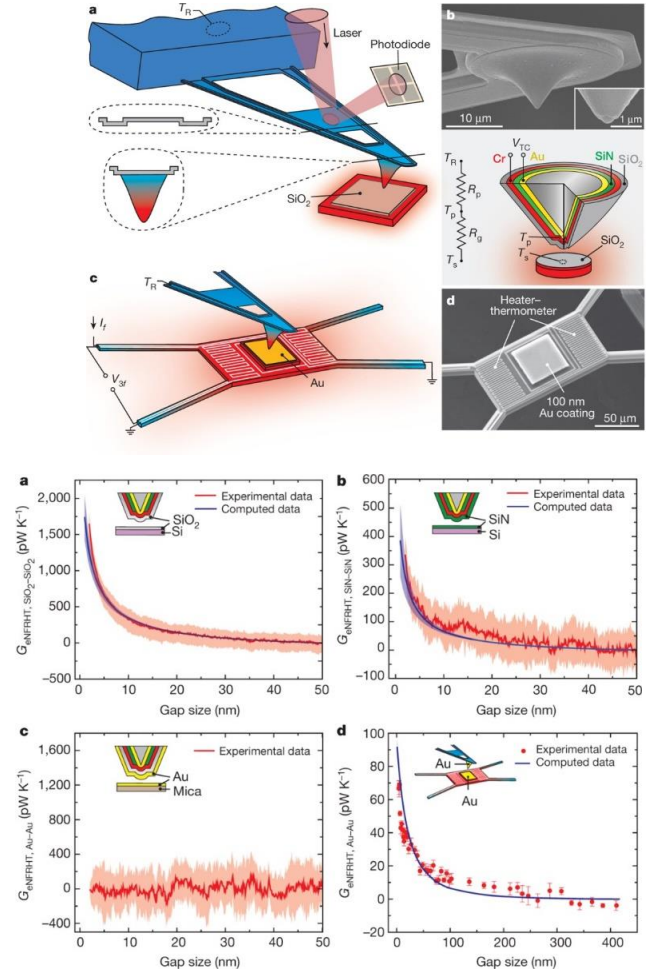

K Kim, B. Song, P. Reddy, *et al. Nature* 1-5 (2015) doi:10.1038/nature16070

nature

K. Dransfeld and J. Xu, J. of Microscopy 152, 35-42 (1988); J. B. Xu, K. Dransfeld, *et al.*, J. App. Phys. 76, 7209 (1994)
J. Xu, K. Dransfeld, *et al.*, J. Vac. Sci. Technol. B12, 2156-2160 (1994); J. B. Xu, K. Dransfeld, *et al.*, Appl. Phys. A-Mater. 59, 155-161 (1994)
J. B. Xu, K. Dransfeld, *et al.*, Rev. Sci. Instrum. 65, 2262-2266 (1994)
J. Xu, K. Dransfeld, *et al.*, Nanosources & Manipulation of Atoms under High Fields and Temperatures Applications 235, 89-100 (1993)

Heat Transfer in Tunneling Junction

Asymmetric Deposition of Thermal Power

Appl. Phys. A 59, 155–161 (1994)

Applied Physics A Solids and Surfaces

Energy-exchange processes by tunneling electrons

J. B. Xu[1,2], **K. Läuger**[2], **R. Möller**[2], **K. Dransfeld**[2], **I. H. Wilson**[1]

[1] Department of Electronic Engineering, the Chinese University of Hong Kong, Shatin, NT, Hong Kong (Fax: +852/603-5558, E-mail: JBXU@ee.cuhk.hk)
[2] Fakultät für Physik, Universität Konstanz, D-78434 Konstanz, Germany

Received 1 October 1993/Accepted 25 March 1994

Abstract. Resistive heating, emission heating or cooling (e.g., the Nottingham effect), and thermal fluctuation radiation are examples of energy exchange processes which are fundamental in electron field emission and in tunneling junctions of scanning tunneling microscopy. These exchange processes are analyzed for both electronic tunneling processes. We first discuss the energy delivered by a monoatomic tip in the field emission process. Strong phonon excitation is expected for field emission currents exceeding 1 nA. Secondly we present a theoretical calculation of the thermal deposition associated with the Nottingham effect in a tunneling junction. The calculation is based on the free electron model for the electrode materials and the tunneling process across a planar vacuum gap. Our results show that the thermal power is deposited *not only* at the electron receiving electrode *but also* at the emitting electrode. This originates from a finite probability for electrons below the Fermi level to tunnel through the tunneling barrier replaced by electrons starting from the Fermi level. The comparison between the calculations and the recent STM measurements is given. Finally we discuss the other energy exchange processes in the tunneling junction, and conclude that the thermal coupling between the tip and the sample of STM is extremely small under UHV conditions. This is important for high temperature STM.

PACS: 61.16, 65.00, 73.40

If electrons tunnel from a sharp metallic tip to a flat metallic electrode or another conducting substrate, two different cases are distinguishable. For a large tip-substrate separation (much larger than the de Broglie wavelength $\lambda_B = h/\sqrt{2meU} = 1.2/\sqrt{U}$ in nm, where U is the applied voltage in volts), electrons can only penetrate the gap when a high electric voltage is applied between the tip and the substrate. This is the typical situation of field emission [1]. However, for a close tip-substrate separation (about λ_B), as realized in scanning tunneling microscopy [2], electrons can tunnel directly across the gap when a small bias voltage is applied. This paper is concerned with the energy dissipation for the two tunneling processes mentioned above [3, 4]. In the first section a brief analysis of energy deposition in field emission will be given. In the remaining sections the energy deposition in a tunneling junction will be discussed in detail.

1 Energy dissipation in the process of field emission

The field emission process can be treated by considering a one-dimensional potential, as shown in Fig. 1. Outside the metal, the potential energy of the electron has some constant value $-(\Phi_0 + E_F)$ relative to zero within the metal. An external field F is applied to draw the electrons from the metal. The positive z-axis is chosen perpendicular to the surface and directed out of the metal, with the

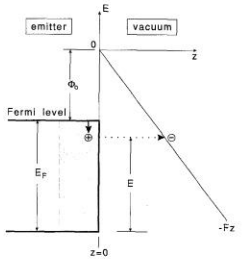

Fig. 1. Potential-energy diagram for field emitted electrons at $T = 0$ K. Φ_0 is the work function of the emitter and F is the externally applied field

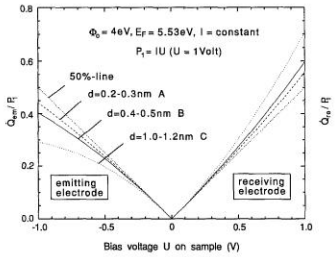

Fig. 3. Calculated fraction of the total power deposited at the emitting electrode *(left)* and at the receiving electrode *(right)* as a function of the bias voltage for constant tunneling current. The total power P_1 is determined by $P_1 = IU$ with $U = 1$ V. For higher bias voltages and larger tunneling distances d, more energy is deposited in the receiving electrode

Neglecting the contribution of the image potential, we obtain for the tunneling probability

$$D(E_z) = \exp\left[-\frac{4\pi}{h} d\sqrt{2m(E_F - E_z + \Phi_0 - eU/2)}\right], \quad (14)$$

where Φ_0 is the work function of the electrons and d is the width of the tunneling gap.

We have calculated numerically the integrals in (11, 12). For gold electrodes, the values of the Fermi energy is 5.53 eV and the work function Φ_0 is 4 eV. The results are shown in Fig. 3.

These results are calculated under the assumption of constant current, which corresponds to the experimental situation [3, 4]. Three curves have been calculated for three gap widths $d = 0.2$, 0.4, and 1 nm, respectively, at a common reference bias voltage of 0.1 V. The variations of d over the voltage range are given in the figure. The values $\dot{Q}_{em}$ and $\dot{Q}_{re}$ are normalized to the total power P_1 at a bias voltage of 1 V.

3 Discussion

To begin with, it would be favourable to review the theoretical calculations in Fig. 3. As mentioned in [3], the tunneling current was kept constant during the experiments. To achieve this in the theoretical calculations, the gap distance must be altered as a function of the bias voltage. In Fig. 3, the range of d in curves A, B and C are 0.2–0.3 nm, 0.4–0.5 nm and 1.0–1.1 nm, respectively. On the basis of the calculations by Lang [23], the absolute gap distance may be estimated from the tunneling resistance for the given parameters of the experiments. This leads to a gap distance of 0.5 nm at a bias voltage of 0.1 V and a tunneling current of 500 nA, which corresponds to curve B in Fig. 3. Curve C represents large gap distances, which corresponds to conventional tunneling conditions in STM. It can be seen from these calculations that the powers deposited at the emitting electrode and the receiving electrode have a nonlinear dependence on the bias voltage, and they are not equal at high bias voltage. This effect we will call 'asymmetry'.

In Fig. 2, the image potential has been omitted. In principle, this potential can be treated within the framework of Simmons [24]. But the calculations are somewhat tedious. However, because an image potential reduces the mean height of the tunneling barrier, we can estimate the heat deposition for the reduced barrier to evaluate the influence of the potential. Calculations show that the asymmetry is thereby enhanced. For example, for $\Phi_0 = 1$ eV and $U = 1$ V, the calculation provides a power ratio of 71% (instead of 60%) at the receiving electrode for curve B in Fig. 3.

The curves in Fig. 3 have been also obtained (for $T = 0$) with the similar procedure used by Engle and Cutler to calculate the inversion temperature of field emission [7]. Although our calculations are restricted to $T = 0$, the cooling effect in the tunneling junction is expected to occur at high temperatures, because the energy levels above E_F become populated and contribute to tunneling. The effects of electrode geometry on the thermal deposition are a matter which requires further theoretical studies. Their calculations are obviously more complex. Miskovsky et al. calculated the effects in the case of field emission [14]. They found that the inversion temperature is higher for the curved tip than for the planar emitter at the same applied voltage.

Now we compare the theoretical results with one of the recent experimental data shown in Fig. 4. The measured data were obtained using a gold tip and sample as a tunneling junction [3]. The experimental data show a good linear dependence of the deposited powers on the bias voltage. With the exception of the results at high

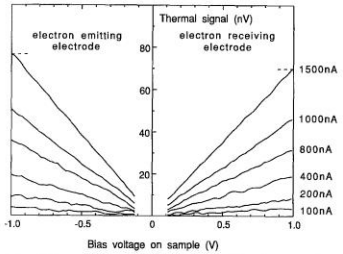

Fig. 4. Measured thermoelectric voltage of the thermocouple as a function of the applied bias voltage. For positive values of U, the sample serves as the receiving electrode and the tip as the emitting electrode. For negative values of U, the sample becomes the emitting electrode and the tip is the receiving electrode, in accordance with Fig. 2. For each curve the average tunneling current is constant. The sensitivity of the thermocouple was 10 μV/K

The discrepancy between the present calculations and the recent measurements in STM can be partially explained by the strong thermal coupling between tip and sample due to adsorbed films in air. Further experimental investigations of the Nottingham effect under UHV conditions, and further theoretical considerations for STM, should contribute a more detailed understanding of the Nottingham effect in STM. An experimental investigation with UHV STM is currently in progress.

Acknowledgements. We wish to thank Profs. C.C. Williams and V.T. Binh for stimulating discussions.

References

1. R. Gomer: *Field Emission and Field Ionization* (Harvard, Cambridge 1961)
2. G. Binning, H. Rohrer: IBM J. Res. Develop. **30**, 355 (1986)
3. J. Xu, R. Möller, K. Läuger, K. Dransfeld, C.C. Williams: In *Nanosources and Manipulation of Atoms under High Fields and Temperatures: Applications*, ed. by V.T. Binh et al. (Kluwer, Dordrecht 1993) pp. 89–100
4. J. Xu: Heat Transfer between two metallic surfaces at small distances. Dissertation, Universität Konstanz (1993)
5. W.W. Dolan, W.P. Dyke, J.K. Trolan: Phys. Rev. **91**, 1054 (1953)
6. W.B. Nottingham: Phys. Rev. **59**, 907 (1941)
7. I. Engle, P.H. Cutler: Surf. Sci. **12**, 208 (1968)
8. M. Drechsler: Z. Naturforsch. **18a**, 1367 (1963)
9. L.W. Swanson, L.C. Crouser, F.M. Charbonnier: Phys. Rev. **151**, 327 (1966)
10. H. Bergeret, A. Septier, M. Drechsler: Phys. Rev. B **31**, 149 (1985)
11. H.-W. Fink: IBM J. Res. Develop. **30**, 460 (1986)
12. J.H. McFee: In *Physical Acoustics IV*, ed. by W.P. Mason, Part A (Academic, New York 1966)
13. R.H. Parmenter: Phys. Rev. **89**, 990 (1953)
14. N.M. Miskovsky, S.H. Park, J. He, P.H. Cutler: J. Vac. Sci. Technol. B **11**, 366 (1993)
15. V.T. Binh, S.T. Purcell, N. Garcia, J. Doglioni: Phys. Rev. Lett. **69**, 2527 (1992)
16. J.W. Gadzuk, E.W. Plummer: Rev. Mod. Phys. **45**, 487 (1973) and references therein
17. F. Flores, P.M. Echenique, R.H. Ritchie: Phys. Rev. B **34**, 2899 (1986)
18. P. Brüesch: *Phonons: Theory and Experiments II*, Springer Ser. Solid-State Sci., Vol. 65 (Springer, Berlin, Heidelberg 1986)
19. H. Heinzelmann, F. Watanabe, G.M. McClelland: Phys. Rev. Lett. **70**, 3611 (1993)
20. M. Kohler: Ann. Phys. (Leipzig) **38**, 542 (1940)
21. J.A. Støvneng, P. Lipavský: Phys. Rev. B **42**, 9214 (1990)
22. J.G. Simmons: J. Appl. Phys. **34**, 1793 (1963)
23. N.D. Lang: Phys. Rev. B **36**, 8173 (1987)
24. J.G. Simmons: J. Appl. Phys. **35**, 2472 (1964)
25. L. Weber, M. Lehr, E. Gmelin: Verh. Dtsch. Phys. Ges. 1005 (1992)
26. U. Gerlach-Meyer, H.-J. Queisser: Phys. Rev. Lett. **51**, 1904 (1983)
27. R. Trzcinski, E. Gmelin, H.-J. Queisser: Phys. Rev. B **35**, 6373 (1987)
28. J.B. Xu, B. Koslowski, R. Möller, K. Dransfeld, I.H. Wilson: J. Vac. Sci. Technol. B (in press)

J. B. Xu, K. Dransfeld, *et al.*, Appl. Phys. A-Mater. 59, 155-161 (1994)

Estimation of Thermovoltage across Vacuum Tunnelling Junction

Proposal to study the thermopower produced by a vacuum-tunneling junction

J. Xu
Department of Electronic Engineering, the Chinese University of Hong Kong, Shatin, N. T., Hong Kong

B. Koslowski, R. Möller, K. Läuger, and K. Dransfeld
Fakultät für Physik, Universität Konstanz, D-78434 Konstanz, Germany

I. H. Wilson
Department of Electronic Engineering, the Chinese University of Hong Kong, Shatin, N. T., Hong Kong

(Received 9 August 1993; accepted 24 January 1994)

This paper elaborates on the idea of using the scanning tunneling microscope in new experiments on thermopower generation by a vacuum-tunneling junction. We first introduce the subject of thermopower generation in metals in the presence of a temperature gradient, emphasizing the physical origins of the thermopower. Then we discuss a thermopower produced in a homogeneous metallic chain containing a tunneling junction. This thermopower is sufficiently large to be measured. Finally, we describe an arrangement to measure the thermopower, especially with the help of the scanning tunneling potentiometry.

I. INTRODUCTION

In recent years, the measurements of thermoelectric voltages generated at microstructures[1,2] and point contacts[3,4] have been the focus of interest of their transport properties. These studies were mostly in the ballistic regime, where the mean free path of the electrons was larger than the size of the microstructure. The Seebeck coefficient or thermopower S is a fundamental transport parameter, like the electrical conductivity σ_e and the thermal conductivity κ. It provides additional information about a system, beyond that obtained from σ_e, since S depends upon the derivatives of the electronic mean free path with respect to energy, rather than just the mean free path itself. In metals S is a sensitive probe of the relative roles of phonon-phonon and phonon-electron interactions, and of the topology of the Fermi surface.

It is well known that a thermoelectric voltage drop ΔU will arise in an open circuit made of two dissimilar metals (heterogeneous chain), if the two junctions are maintained at different temperatures[5] (see Fig. 1). The thermoelectric voltage ΔU is proportional to the temperature difference $\Delta T = T_2 - T_1$, if ΔT is small.

The thermopower S^{AB} is defined by

$$S^{AB} = \lim_{\Delta T \to 0} \left| \frac{\Delta U}{\Delta T} \right|, \tag{1}$$

where $\Delta U = U_b - U_a$ is the thermoelectric voltage produced by the open circuit, and $\Delta T = T_2 - T_1$ the temperature difference between the junctions c and d. The measuring points a and b have the same temperature T_0.

The absolute thermopower of a homogeneous material depends on the material itself. For the two different metals A and B, we have

$$S^{AB} = S^B - S^A, \tag{2}$$

where S^A and S^B are the absolute thermopowers of A and B, respectively. The determination of the absolute thermopower (S^A and/or S^B) is rather difficult.[5] However, relative changes are comparatively easier to measure.

As a starting point for the following discussion, we shall explicitly write the absolute thermopower S (of a metal A) as the sum of two parts: $S = S_e + S_d$. Here the term S_d is the diffusion component, and has its origin in the diffusion of the electrons in metal A due to the presence of a temperature gradient, and the other term S_g is the so-called phonon-drag component. For simplicity, we will drop the superindex A.

Since the conduction electrons in simple metals diffuse from the hot to the cold end, and the electrons have negative charge, the sign of S_d should in general be *negative*. An expression of S_d for simple metals has been derived from the Mott formula:[5]

$$S_d = -\frac{\pi^2}{3}\frac{k}{|e|}\frac{kT}{\sigma_e}\frac{\partial \sigma_e}{\partial E}\bigg|_{E=E_F}, \tag{3}$$

where σ_e is the electrical conductivity, E_F is the Fermi energy, and k is the Boltzmann constant. σ_e can be expressed by[5]

$$\sigma_e = \frac{e^2 l_e(E) S_F(E)}{12\pi^3 \hbar}, \tag{4}$$

where $l_e(E)$ is the electron mean free path and $S_F(E)$ is the total area of the Fermi surface. Inserting σ_e into Eq. (3), one deduces

$$S_d \propto -\frac{1}{\sigma_e}\frac{\partial \sigma_e}{\partial E} = -\frac{\partial \ln \sigma_e}{\partial E} = -\frac{\partial \ln l_e}{\partial E} - \frac{\partial \ln S_F}{\partial E}. \tag{5}$$

The first term is expected to be negative since the more energetic electrons have longer mean free paths. But the second term depends upon the details of the Fermi surface and can be either positive or negative. The second term may even outweigh the first term so that the thermopower may be *positive*. This is the case, for example, for the noble metals such as Au, Ag, and Cu. For the free-electron model, the Fermi

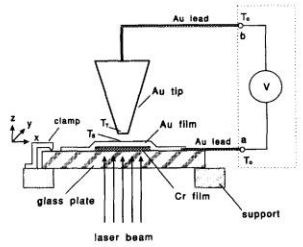

FIG. 4. The experimental arrangement for measuring the thermoelectric voltage produced by a tunneling junction. V is a voltmeter with high input impedance.

moelectric voltage produced by the tunneling junction consisting of an Au tip and an Au substrate under UHV conditions. These experiments are being carried out in Konstanz.

The schematic diagram of the proposed experimental setup is shown in Fig. 4. Two films of Cr and Au are crosswise evaporated onto a glass plate to form a thermocouple.[10,11] Both films have a minimum thickness of 200 nm so that the diffusion process between both metals can be ignored. The width of the films is about 200 μm. The sample (Au film) is heated by a laser beam from the backside through the glass plate. The thick Cr film absorbs ~50% of the optical power and converts it into heat. The thermal resistance from the Cr–Au junction to the surroundings is around 5×10^3 K/W.[11] Thus for a temperature rise of 10 K in the area of the Cr–Au junction an absorbed power of 2 mW is required. This is easily provided by a laser diode. The temperature increase of the sample can, of course, be directly measured by the Cr–Au thermocouple.

To mount the sample, one of its ends should be glued to the metallic support for good thermal contact, and the other be pressed against the support by a metallic spring so as to allow thermal expansion of the glass and reduce any surface bending in the z direction (see Fig. 4).

To control the tip–sample distance and to measure the relevant thermoelectric voltage, the novel technique of "scanning noise potentiometry" proposed by Möller *et al.*[18] and Koslowski[19] could be applied. The thermoelectric voltage is equal to

$$\Delta U = U_b - U_a = \int_{T_S}^{T_T} [S^{Au}(T') - S_d^t(T')]dT' + U_0, \tag{12}$$

where U_0 is the offset voltage in the external circuit without heating. U_0 can be canceled electronically.

According to the discussion in Ref. 11, the thermal coupling due to several mechanisms between tip and sample under UHV conditions is extremely weak, and we can suppose $T_T \approx T_0$. The difference $T_S - T_T$, as mentioned above, is directly measured by the Cr–Au thermocouple.

If the difference between T_T and T_S is not too large, we obtain

$$\Delta U = \int_{T_S}^{T_0} [S^{Au}(T') - S_d^t(T')]dT'$$
$$\approx (T_0 - T_S)[S^{Au}(\bar{T}) - S_d^t(\bar{T})]. \tag{13}$$

Here $S^{Au} = S_d^{Au} + S_g^{Au}$ is the thermopower of bulk gold, and S_d^t is the thermopower of the tunneling junction. $\bar{T} = (T_T + T_S)/2$ is the average temperature of the tunneling junction. At room temperature, $S_g^{Au} \to 0$, $S^{Au} \approx S_d^{Au} \approx 1.9$ μV/K. Combining Eqs. (11) and (13), we obtain

$$\Delta U = (T_0 - T_S)\left(1.9 + \frac{3.76}{\sqrt{\Phi}} z - \frac{19.2}{E_F}\right). \tag{14}$$

For $E_F = 5.53$ eV, $\Phi = 4$ eV, $z = 5$ Å, $T_0 - T_S = -10$ K, we find

$$\Delta U = (U_b - U_a) \approx (1.88z - 1.58)(-10) \approx -78(\mu V). \tag{15}$$

This relatively large value can easily be measured experimentally. It would imply that at room temperature there exists a considerable thermoelectric voltage in a closed homogeneous-gold chain containing a tunneling contact.

At low temperatures, for example, at $\bar{T} = 30$ K, $S_d^{Au} \to 0$, $S^{Au} = S_g^{Au} \approx 1.3$ μV/K.[5] If Eq. (10) is still valid and the parameters for Eq. (15) are the same, we find

$$\Delta U = (U_b - U_a) = (1.3 - 0.35 + 0.188z)(-10)$$
$$\approx -19(\mu V). \tag{16}$$

This thermoelectric voltage should be still measurable. Here the contribution from bulk gold [the first term in Eq. (16)] has the same order of magnitude as the contribution from the tunneling junction (the second and third terms).

A first attempt to measure the thermopower generated by a tunneling junction has recently been made in Konstanz under UHV conditions. The magnitude of the thermopower is indeed detectable. The preliminary result indicate that thermovoltages between 20 and 100 μV can be observed for a temperature difference of approximately 10 K between tip and sample.

IV. CONCLUSIONS

The tunneling junction of a STM can generate a thermopower when a temperature difference is applied to the junction. If the junction is placed in a closed homogeneous chain consisting of one metal throughout only, this thermopower cannot be compensated by the thermopower produced in the remaining parts of the chain. In this paper, we discussed theoretically the thermopower generated in the closed chain made of gold. We find that the magnitude of the thermopower should be measurable at room temperature, if the temperature difference across the junction is of the order of 10 K. We propose an experimental arrangement to measure the thermopower at room temperature by means of scanning tunneling noise potentiometry. A preliminary experiment under UHV conditions indicates that the thermopower produced by a tunneling junction is observable.

ACKNOWLEDGMENT

We appreciate invaluable discussions with M. Jericho.

[1] L. W. Molenkamp, Th. Gravier, H. van Houten, O. J. Buijk, M. A. A. Mabesoone, and C. T. Foxon, Phys. Rev. Lett. **68**, 3765 (1992).
[2] B. L. Gallagher, T. Galloway, P. Beton, J. P. Oxley, S. P. Beaumont, S. Thomas, and C. D. W. Wilkinson, Phys. Rev. Lett. **64**, 2058 (1990).
[3] O. I. Shklyarevskii, A. G. M. Jansen, J. G. H. Hermsen, and P. Wyder, Phys. Rev. Lett. **57**, 1374 (1986).
[4] L. Weber, M. Lehr, and E. Gmelin, Phys. Rev. B **46**, 9511 (1992).
[5] R. D. Barnard, *Thermoelectricity in Metals and Alloys* (Taylor and Francis, London, 1972).
[6] E. N. Bogacheck, I. O. Kulik, A. N. Omel'yanchuk, and A. G. Shkorbatov, JETP Lett. **41**, 633 (1985).
[7] R. Möller, A. Esslinger, and B. Koslowski, J. Vac. Sci. Technol. A **8**, 590 (1990).
[8] J. M. R. Weaver, L. M. Walpita, and H. K. Wickramasinghe, Nature **342**, 783 (1989).
[9] C. C. Williams and H. K. Wickramasinghe, Nature **344**, 317 (1990).
[10] J. Xu, R. Möller, K. Läuger, K. Dransfeld, and C. C. Williams, in *Nanosources and Manipulation of Atoms Under High Fields and Temperatures: Applications*, edited by V. T. Binh *et al.* (Kluwer Academic, Amsterdam, 1993), p. 89–100.
[11] J. Xu, Ph.D. thesis, Universität Konstanz, 1993.
[12] M. Kohler, Ann. Phys. **38**, 542 (1940).
[13] C. R. Leavens and G. C. Aers, Solid State Commun. **61**, 289 (1987).
[14] J. A. Støvneng and P. Lipavský, Phys. Rev. B **42**, 9214 (1990).
[15] R. P. Huebener, Phys. Rev. A **136**, 1740 (1964).
[16] R. F. Moreland and R. R. Bourassa, Phys. Rev. B **12**, 3991 (1975).
[17] Y. Kuk, in *Scanning Tunneling Microscopy I*, edited by H.-J. Güntherodt and R. Wiesendanger (Springer, Berlin, 1992), pp. 17–37.
[18] R. Möller, C. Baur, A. Esslinger, and P. Kurz, J. Vac. Sci. Technol. B **9**, 609 (1991).
[19] B. Koslowski, Ph.D. thesis, Universität Konstanz, 1993.

J. B. Xu, K. Dransfeld, *et al.*, J. Vac. Sci. Technol. B12, 2156-2160 (1994)

Measurement of Thermovoltage across the Junction

PHYSICAL REVIEW B VOLUME 52, NUMBER 19 15 NOVEMBER 1995-I

Thermovoltage across a vacuum barrier investigated by scanning tunneling microscopy: Imaging of standing electron waves

D. Hoffmann, J. Y. Grand, and R. Möller
4. Physikalisches Institut, Universität Stuttgart, Pfaffenwaldring 57, 70550 Stuttgart, Germany

A. Rettenberger and K. Läuger
Fakultät für Physik, Universität Konstanz, Postfach 5560 M675, 78434 Konstanz, Germany
(Received 20 July 1995)

The thermovoltage of a vacuum barrier has been studied by heating the tip of a scanning tunneling microscope. It is extremely sensitive to minor variations of the electronic structure of the sample. As an example an electronic surface state on Cu(111) has been investigated. The reflection at step edges and other defects leads to an interference pattern modulating the thermovoltage by up to 2 μV/K. The findings are well described by a numerical calculation which confirms that the latter differs from a map of the electronic density of states.

Thermovoltages result from transport phenomena if an electric conductor is submitted to a temperature gradient. A special case arises if the conductor is formed by a vacuum barrier which allows electronic tunneling. The thermovoltage is given by the bias which is needed to balance forward and backward tunneling. Therefore a measurement of this quantity represents a critical test for the theoretical description of the tunneling process and the involved electronic states. Since tunneling occurs from occupied to unoccupied states only electrons in the small range of about $+/-$ 2 kT around the Fermi level may contribute in the absence of any external bias. In consequence the thermovoltage depends crucially on the density of states of both electrodes in the vicinity of the Fermi level.

Williams and Wickramasinghe[1] performed an experiment at ambient conditions analyzing the thermovoltage of a scanning tunneling microscope (STM). They found a lateral variation on MoS_2 between the Mo and S atoms.

We present an investigation of the thermovoltage across a vacuum barrier. Our measurements show that this quantity is extremely susceptible to minor variations of the electronic structure of both electrodes. This sensitivity, combined with extreme lateral resolution which can be obtained by using a STM, will make a promising tool in surface science.

For metallic sample surfaces and tunneling tips the observed thermovoltage, i.e., the thermovoltage per temperature difference, is about one order of magnitude larger than the values for metallic bulk.[2] In addition it is negative even for Au, Ag, and Cu samples with positive bulk values for the thermopower. Its absolute value depends on several parameters, e.g., the crystallographic orientation of the surface.

A particularly interesting example to analyze how the thermovoltage depends on the electronic system is found for the (111) surfaces of noble metals. They are known to support electronic surface states representing an almost free two-dimensional electron gas which is reflected at monoatomic steps and other defects.[3] By tunneling spectroscopy performed at low temperature, Crommie, Lutz, and Eigler[4] succeeded in imaging the electronic density of these waves on Cu(111) for different types of confinement. Hasegawa and Avouris[5] showed for Au(111) and Ag(111) that even at room temperature standing waves of the surface states can be observed; however, the coherence length is reduced due to the thermal energy spread.

Our experiments show that standing electron waves of surface states, e.g., on Cu(111), lead to a modulation of the thermovoltage observed in STM. Moreover the thermovoltage does not yield the same information as tunneling spectroscopy; it is related in a more subtle way to the electronic density of states of the tip and sample. A careful analysis of the data yields k as well as dE/dk of the surface state at E_F.

Experiments have been performed by a STM operated in ultrahigh vacuum. A temperature difference between tip and sample of about 10 K has been achieved by heating the shaft of the tip by laser irradiation of about 50 mW (568 nm).[6] Stable steady-state conditions with little thermal drift have been achieved by a constant laser output and a sufficient time for the system to equilibrate (several hours). The way the experiment is conducted excludes heating of the sample. The coupling across the vacuum barrier by radiation and by the tunneling electrons can be completely neglected in comparison to the thermal conductance of tip and sample.[7]

To measure the thermovoltage the STM has been operated in a potentiometry mode relying on the thermal noise of the vacuum barrier.[8] The square of the spectral density of the latter is proportional to the conductance of the tunneling gap, hence it shows the same exponential distance dependence on the gap width as the tunneling current in normal STM operation. However, it is independent of the bias voltage and does not disappear at 0 V. This permits us to use a second feedback loop to adjust the external bias such that the net current vanishes. The technique yields a typical resolution of about 3 μV. Without heating, the observed potential is constant within a few μV. To verify the experimental results which are presented, the direction and speed of the scan have been varied.

0163-1829/95/52(19)/13796(3)/$06.00

Cu(111) has been prepared by evaporating 200 nm of Cu onto a mica substrate heated to 550 K. The sample is transferred in vacuum to the STM. The tunneling tips have been electrochemically etched from a tungsten wire. They have been cleaned *in situ* by field emission and covered with copper by a controlled touch with the copper surface shortly before the measurement.

Figure 1 shows the topography of a small area of a Cu(111) surface and the thermovoltage which has been measured simultaneously. To enhance the visualization of the thermal signal, Fig. 1(c) shows a shaded representation of the data. The area is characterized by a strip of a single additional layer of copper with a width of 10 nm. Approximately in the center of the area is a small defect which can hardly be recognized in the topography. Its nature cannot be deduced from our data; however, it strongly influences the thermovoltage. The latter shows a wavy signal which looks like an interference pattern caused by the monoatomic steps and the defect near the center. Beside the structure parallel to the steps, additional features in a perpendicular direction can be observed in the vicinity of the defect.

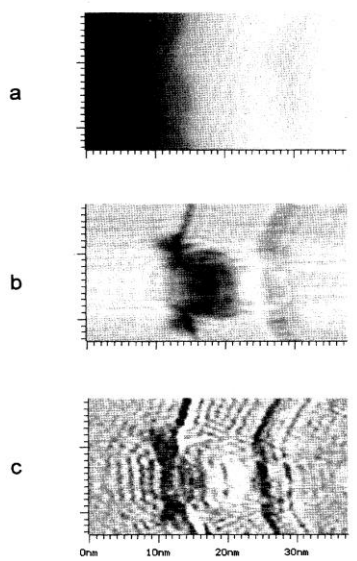

FIG. 1. Topography and thermovoltage for a Cu(111) surface. (a) Gray scale representation of the topography obtained at an average current noise of 5 pA. (b) Gray scale representation of the thermovoltage at the sample for a temperature difference of about 10 K. The thermovoltage is about -50 μV on the flat part, and decreases by about 50 μV at a step. (c) Shaded representation of the thermovoltage.

Figure 2, curves a and b, shows cross sections taken to the left of the first step in the upper part of Fig. 1. The position has been chosen because no other defects are close by. The topography is represented by a; the monoatomic step can be well recognized. The measured thermovoltage is given by b. The periodicity of the signal is approximately 15 Å; about 4–5 oscillations can be resolved. At the step itself an additional contribution to V_{th} of about -60 μV appears which is probably due to the modification of the projected bulk states in the vicinity of the step.[2]

To explain thermoelectric effects observed in STM, the tunneling current caused by the difference of the Fermi distributions of both electrodes has to be analyzed. This current will charge the electrodes till the tunneling current caused by the resulting bias voltage equals the first one. As outlined by Støvneng and Lipavský[9] the thermovoltage V_{th} at the electrode with the higher temperature is given by the ratio of the thermal-induced tunneling current to the conductance of the tunneling barrier:

$$V_{th} = -\frac{I_{th}}{\sigma} .$$

The thermally generated tunneling current at zero bias is

$$I_{th} = a \int \rho_T \rho_S \left[f\left(\frac{E}{kT_T}\right) - f\left(\frac{E}{kT_S}\right) \right] dE ,$$

where a is a constant; ρ_T is the electronic density of states of the tip at its surface; and ρ_S is the density of states of the sample taken at the tip surface, and thus contains the decay of the wave functions into the vacuum, and hence

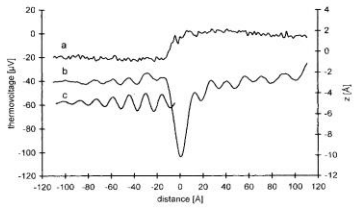

FIG. 2. Cross section through the interference pattern normal to a step edge. (Curve a) topography of a section of a single line of Fig. 1. (Curve b) measured thermovoltage. (Curve c) calculated thermovoltage. (Curve d) calculated tunneling conductance.

nneling probability. f is the Fermi distribution, E energy, k is Boltzmann's constant, and T_T and T_S e temperature of the tip and sample, respectively. onductance is given by

$$= -\tfrac{1}{2} ea \int \rho_T \rho_S \frac{\partial}{\partial E} \left[f\left(\frac{E}{kT_T}\right) + f\left(\frac{E}{kT_S}\right) \right] dE ,$$

e is the elementary charge.
solve the above integrals in an analytical form, eng and Lipavský used several approximations, unfortunately cannot be applied to our problem. ovide a more quantitative understanding of our re- we have numerically evaluated the thermovolt- ssuming that ρ_S, the total density of states for the le, is given by the sum of the projected bulk states ne surface state. The density of the latter can be de- d by a Bessel function[4]

$$_{SS} = g[1 - J_0(2k_{\parallel}x)]e^{-2\alpha z} ,$$

the k vector parallel to the surface $1/\hbar)\sqrt{2m^*(E-E_S)}$ and the decay length of the onic wave function into the vacuum $/\hbar)\sqrt{2m(\phi - E) + \hbar^2 k_{\parallel}^2}$, using m^* the effective on mass E_S the energy at the band edge for the surface. z is the coordinate normal to the surface, and arallel to the surface and perpendicular to the step. ls of the calculation will be published elsewhere.[10] calculation yields a large thermovoltage $-I_{th}/\sigma$ with a small modulation due to the surface V_{th} is negative since I_{th} and σ are positive. It is slightly influenced by the choice of parameters for of the tip, the projected bulk states, or the relative t of the surface state. Only the offset and the ll amplitude of the oscillation are affected. Howev- relative amplitude of the maxima and minima de- strongly on dE/dk, the slope of the dispersion relation of the surface state. Trace c in Fig. 2 shows the result of the calculation. For comparison with the experiment the data have been scaled in the vertical direction by an arbitrary factor. Within the experimental errors the periodicity as well as the envelope of the oscillations is well described. The best agreement with the experimental data is found for the surface state using the parameters $m^* = 0.46$ m and $E_S = -0.39$ eV given by Kevan and Gaylord.[11] To compare with data obtained by tunneling spectroscopy, the calculated conductance which corresponds to dI/dV is plotted in curve d. While the periodicity is the same the envelope strongly differs, i.e., it decreases monotonically. In addition there is a phase shift relative to the thermovoltage which approaches $\pi/2$ with increasing distance from the step.

In summary the lateral variation of the thermal-induced voltage across a vacuum barrier has been investigated. It allows us to map details of the electronic structure of the surface. This was demonstrated for the example of interference structures of the two-dimensional (2D) electron gas of a surface state on the Cu(111) surface. The periodicity of the observed modulation agrees with the data of Crommie, Lutz, and Eigler,[4] who measured the tunneling conductance by dI/dV spectroscopy at low temperature. However, the envelope and the phase of the oscillations in the thermovoltage is completely different. The latter is given by the ratio between the thermally generated tunneling current and the tunneling conductance. Numerical calculations reveal that the amplitude of the oscillations depends crucially on dE/dk for the surface state at the Fermi energy. A good agreement with the experimental data is obtained by using parameters known from photoemission experiments.

The authors would like to thank C. Baur and B. Koslowski as well as P. Leiderer and K. Dransfeld for stimulating discussions.

Williams and H. K. Wickramasinghe, Nature **344**, 317 0).
offmann, A. Rettenberg, J. Y. Grand, K. Läuger, P. Leid-, K. Dransfeld, and R. Möller, Thin Solid Films **264**, 223 5) (see also B. Koslowski, Dissertation, University of stance, 1993).
Davis, M. P. Everson, R. C. Jaklevic, and W. Shen, Phys. . B **43**, 3821 (1991).
Crommie, C. P. Lutz, and D. M. Eigler, Nature **524**, 363 3).
asegawa and Ph. Avouris, Phys. Rev. Lett. **71**, 1071 3).
[6]The temperature has been measured in a separate experiment by using a small thermocouple of negligible thermal conductance attached to the tunneling tip.
[7]J. B. Xu, K. Läuger, R. Möller, K. Dransfeld, and I. H. Wilson, J. Appl. Phys. **76**, 7209 (1994).
[8]R. Möller, C. Baur, A. Esslinger, U. Graf, and P. Kürz, J. Vac. Sci. Technol. B **9**, 609 (1991).
[9]J. A. Støvneng and P. Lipavský, Phys. Rev. B **42**, 9214 (1990).
[10]D. Hoffmann, A. Rettenberger, K. Läuger, J. Y. Grand, and R. Möller (unpublished).
[11]S. D. Kevan and R. H. Gaylord, Phys. Rev. B **36**, 5809 (1987).

D. Hofmann, J. Y. Grand, R. Moller, A. Rettenberger, K. Lauger, Phys. Rev. B. 52, 13796-13798 (1995)

Recent Measurement of Thermovoltage

Confined Friedel oscillations on Au(111) terraces probed by thermovoltage scanning tunneling microscopy

Kai Sotthewes,* Michiel Nijmeijer, and Harold J. W. Zandvliet
Physics of Interfaces and Nanomaterials, MESA+ Institute for Nanotechnology, University of Twente, P.O. Box 217, 7500 AE Enschede, The Netherlands

(Received 29 January 2021; revised 7 June 2021; accepted 11 June 2021; published 29 June 2021)

The spatial dependence of the local density of states at the Fermi level of a stepped Au(111) surface is studied by thermovoltage scanning tunneling microscopy. The periodicity of the standing waves is not given by $\lambda_F/2 =$ 1.8 nm, as expected based on the band diagram of Au(111), but rather varies between 1.5 and 2.1 nm depending on the exact width of the terraces. This counterintuitive result can be understood by considering the superposition of incident and reflected electron waves, which have a periodicity of $\lambda_F/2$. The change in periodicity is a direct consequence of the decaying nature of the Friedel oscillations.

DOI: 10.1103/PhysRevB.103.245311

I. INTRODUCTION

Standing waves are ubiquitous in optical, electronic, and mechanical experiments. On the nanoscale, electron standing wave patterns have been extensively studied by scanning tunneling microscopy (STM) since the seminal work of Crommie *et al.* [1,2]. These authors used the STM to drag individual iron atoms on a copper substrate to a predefined position. One of the nanostructures they assembled via atomic manipulation was a circle consisting of 48 iron atoms. This circle of iron atoms, also referred to as a quantum corral, acts as a barrier for the surface state electrons at the Fermi level. As the incoming and outgoing electron waves interfere with each other, a circular standing wave pattern develops inside the quantum corral. This electron density modulation of the surface is referred to as a Friedel oscillation and is given by

$$\rho_s(r,E) = \rho_b + C\frac{\cos(2k_F|r| + \delta)}{|r|^D}, \quad (1)$$

where k_F is the Fermi wave vector, ρ_b the bulk contribution to the electron density, δ a phase factor, D the dimensionality of the electron system, and $|r|$ the distance from the scattering center.

There are various ways to measure Friedel oscillations with STM. For metals it is usually sufficient to make a topographic map at a small sample bias, as in this case only the electrons in the vicinity of the Fermi level contribute to the tunnel current [1–3]. In order to measure the dispersion relation of the surface state electrons, the differential conductivity (dI/dV), which is proportional to the local density of states (LDOS), is measured as a function of the bias voltage (V) [4–9]. Alternatively, one can make a spatial map of the thermovoltage (V_{th}) that arises if a temperature gradient is applied across the scanning tunneling microscopy junction. The thermovoltage, which is proportional to the derivative of the LDOS to the energy, provides direct information on the spatial variation of the Friedel oscillations [10–13].

To date the vast majority of scanning tunneling microscopy studies have been focused on electron standing wave patterns near defects or steps on noble metal surfaces that possess a two-dimensional surface state, such as Au(111), Ag(111), and Cu(111) [1–6,12,14–18]. During the last few years, however, the technique has also been applied to more diverse materials, such as semiconductors [19], topological insulators [20], two-dimensional materials [21], and ferroelectric materials [9].

The confinement of surface state electrons on terraces owing to the presence of step edges has been studied in quite some detail [4,6–8,22]. The standing wave patterns are well described by the Fabry-Pérot resonator model for terrace widths L in the range of $\lambda_F/2$ to $3\lambda_F/2$, where λ_F is the Fermi wavelength [4,6]. λ_F can be determined from the dispersion of the Au(111) surface state and is equal to $\lambda_F = 3.6$ nm. For terrace widths smaller than $\lambda_F/2$, the confinement changes from terrace modulation to step modulation [7,22].

So far, for terrace widths exceeding $\lambda_F/2$, a systematic study of the interference pattern as a function of the terrace width is still lacking. In this paper, we probe the interference pattern for electrons confined on terraces with $L > 3\lambda_F/2$ using thermovoltage STM. Surprisingly, the measured wavelength of the standing waves is altered and no longer equal to $\lambda_F/2$. The confinement influences the observed oscillations for terrace widths $L > 3\lambda_F/2$. We will show that at these length scales the decaying nature of the Friedel oscillations plays a pivotal role. The oscillations in this regime are formed by the interference of several waves formed by the superposition of incident and reflected electron waves at the step edges of the Au(111) surface. The waves have a wave vector equal to k_F, similar as for an infinitely large terrace, but the wave vector of the resulting interference pattern varies depending on the exact terrace width.

II. EXPERIMENTAL DETAILS

The experiments are performed with a RHK Technology UHV3000 variable temperature STM equipped with R9 hardware and a home-built thermovoltage module [13]. The tip is kept at room temperature ($T_T = 293$ K), while the sample is cooled down to $T_S = 220$ K. During the thermovoltage measurement, the tip-sample distance (Δz) is reduced by 0.3 nm with respect to the set point used in the topographic measurement. The sample used in these experiments consists of a 200-nm-thick Au(111) layer on mica purchased from Phasis (Geneva, Switzerland).

III. RESULTS AND DISCUSSION

A thermovoltage arises between the tip and surface if a temperature gradient is applied across the STM tunnel junction. V_{th} is the voltage needed to compensate for the thermally generated tunneling current. The thermally generated tunneling current is caused by inequalities in the Fermi-Dirac distributions, as well as differences in the LDOS at the Fermi levels of tip and sample, and has two opposite contributions with energies above and below the Fermi level. Støvneng and Lipavský [23] derived the following expression for V_{th} within the Tersoff-Hamann [24] approximation:

$$V_{th} = \frac{\pi^2 k_B^2 T_m \Delta T}{3e}\left[\frac{1}{\rho_t}\frac{\partial \rho_t}{\partial E} + \frac{1}{\rho_s}\frac{\partial \rho_s}{\partial E} + \frac{z}{\hbar}\sqrt{\frac{2m_0}{\phi}}\right], \quad (2)$$

where k_B is the Boltzmann constant, $\hbar$ is the reduced Planck constant, m_0 is the electron mass, e is the electron charge, ϕ is the work function, z is the tip-sample distance, and ρ_t and ρ_s are the local density of states of the tip and sample, respectively. $T_m = \frac{1}{2}(T_t + T_s)$ is the mean temperature with the tip (T_t) and sample (T_s) temperature and $\Delta T = T_t - T_s$ the temperature difference. Since ρ_t and z are assumed to be constant, the dominant term for the spatial variation of V_{th} is given by $\frac{1}{\rho_s}\frac{\partial \rho_s}{\partial E}$. The latter results in a high sensitivity in the LDOS modulations around E_F.

The LDOS $\rho_s(r,E)$ of electrons with wave vector $k(E)$ scattered at a monatomic step can be calculated by summing up all states (surface and bulk states) at energy E [1],

$$\rho_s(x,E) = \rho_b(E) + L_0[1 - RJ_0[2k(E)x]], \quad (3)$$

where $L_0 = m^*/(\pi\hbar^2)$, x the distance from the step, $\rho_b(E)$ the bulk LDOS (assumed to be independent of x and y), R the reflectivity of the step [$R = 0.4$ for Au(111)] [12,25], $k^2 = 2m^*E/\hbar^2$, and J_0 the zero-order Bessel function. Note here, that for the thermovoltage measurements, the energy is equal to the Fermi energy and therefore constant and hence $\rho_b(E)$ is a constant and $k(E)$ is equal to k_F.

Equation (3) is only valid in the regime where the LDOS is linear at the Fermi level, which is only in the direct vicinity of the step edge. Therefore Eq. (2) is no longer applicable because the LDOS is no longer linear around E_F [26]. A spatial dependent expression is derived in Ref. [26] for $V_{th}(x)$ based on the following approximations [26,27]: (i) $eV_{th} \ll k_B T_s$, (ii) $4k_B T_s \partial\rho_s/\partial E \ll \rho_s$, and (iii) $4k_B T_s s \ll \varepsilon_0$ and is given by

$$V_{th}(x) = \frac{CJ_1(2k_F x)h_Z(x)}{1 - CJ_0(2k_F x)h_N(x)}, \quad (4)$$

$$h_Z(x) = \frac{\varepsilon_0}{ek_F}\left(\frac{s_s}{\sinh(s_s x)} - \frac{s_t}{\sinh(s_t x)}\right);$$

$$h_N(x) = \frac{1}{2}\left(\frac{s_s x}{\sinh(s_s x)} + \frac{s_t x}{\sinh(s_t x)}\right) \quad (5)$$

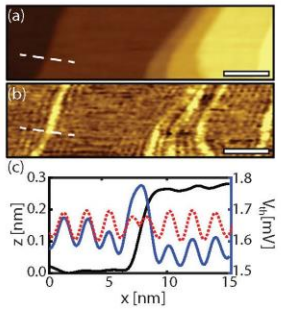

FIG. 1. (a) Topography image (75×21 nm^2, scale bar is 13 nm) of Au(111) showing a stepped Au(111) surface. The tunneling parameters are 300 mV and 300 pA. (b) The corresponding thermovoltage map for $T_T = 293$ K, $T_S = 220$ K, and $\Delta z = 0.3$ nm, showing surface electron interference patterns. (c) The height (left, black) and V_{th} (right, blue) profile measured simultaneously along the dashed line in (a) and (b). The red dashed line is the model described by Eq. (4), using $k_F = 1.74$ nm^{-1}.

with $C = PR = 0.2$. P is the surface state contribution with respect to the bulk and is experimentally determined to be $P = 0.5$ [1,28]. $s_s = \pi k_B T_s k_F/\varepsilon_0$ and $s_t = \pi k_B T_t k_F/\varepsilon_0$ with ε_0 the energy minimum of the surface state (-0.41 eV for Au(111) [29,30]).

Figure 1 shows the topography and the simultaneously obtained thermovoltage map of the Au(111) surface. In the thermovoltage map [see Fig. 1(b)] the step edges show up as 200 μV high peaks with respect to the average thermovoltage value of the terrace. The increase in the thermovoltage at the step is a result of the enhanced coupling of the tunneling electrons with the bulk states [10,11]. In the vicinity of step edges, the thermovoltage shows a spatially decaying oscillating behavior, which can be attributed to electronic standing waves. These Friedel oscillations have a periodicity of 1.8 nm [see Fig. 1(c)]. Since no bias is applied, we are dealing with Fermi electrons. Using the dispersion relation of the surface state of Au(111) [29,30],

$$E = \varepsilon_0 + \frac{\hbar^2 k^2}{2m^*} \quad (6)$$

with $\varepsilon_0 = -0.41$ eV and $m^* = 0.28$, we find a corresponding wave vector of 1.74 nm^{-1} ($\lambda_F = 3.6$ nm). In good agreement with the experimental observations and previous studies [3], this leads to a periodicity of 1.8 nm ($\lambda_F/2$) in the LDOS at E_F.

The red line in Fig. 1(c) is the model as described by Eq. (4) and qualitatively fits the measured Friedel oscillations. In order to fit the model, the effective boundary location is taken close to the midpoint of the rise in the topological scan and at the maximum of the thermovoltage measurement [5]. The first oscillation is completely covered by the signal originating from the step.

Figure 2(a) shows the topography of a stepped Au(111) surface. The terrace width varies between 3.5 and 10 nm, which is in the range of λ_F to $3\lambda_F$. In the corresponding thermovoltage map [Fig. 2(b)], the electron standing waves are clearly visible. The number of observed oscillations depends on the terrace width. In Fig. 3(a) the number of peaks (P_N) and the periodicity ($\tilde{\lambda}_{in} = 2\lambda_{in}/\lambda_F$, where λ_{in} is the measured periodicity) are plotted as a function of the terrace width (L). P_N increases stepwise as a function of L. In contrast to the *particle-in-a-box* model, oscillations exist for every terrace width, except for $L < 4$ nm. For $L < \lambda_F$ no oscillations are observed in agreement with previous studies due to the conversion from terrace modulation to step modulation [7,22]. The width of the plateaus is approximately equal to the $\lambda_F/2$. The measured wavelength of the oscillations (λ_{in}) decreases from 2.1 to 1.5 nm ($\tilde{\lambda}_{in}$ varies between 1.2 and 0.8) as L increases and is centered around 1.8 nm, which is equal to $\lambda_F/2$. When P_N increases, the wavelength first rapidly increases to decrease again with increasing terrace width. This is unexpected as k (and thus λ) is determined by the band diagram and the energy at which the measurement is performed [see Eq. (6)]. Similar to a large terrace (as in Fig. 1), the wavelength is expected to be equal to $\lambda_F/2 = 1.8$ nm with a deviation for terrace widths close to $1.5\lambda_F$ [7].

The observed interference pattern and the relation between L, P_N, and λ_{in} cannot be properly described by the Fabry-Pérot resonator model [4] as oscillations exist for all terrace widths. Therefore, a model is proposed that relies on the interference of decaying standing waves in the LDOS. For electrons in confinement, two steps are involved and therefore several (depending on the number of reflections that are taken into account) wave functions should be considered compared to the two for the single step model [26]. This leads to the following spatial dependent expression for $V_{th}(x)$ (see the Appendix for the complete derivation):

$$V_{th}(x) = \frac{CJ_1(2k_F x)h_{z1}(x) + CJ_1[2k_F(L-x)]h_{z2}(x)}{1 - CJ_0(2k_F x)h_{n1}(x) - CJ_0[2k_F(L-x)]h_{n2}(x)} \quad (7)$$

with

$$h_{z1}(x) = \frac{\varepsilon_F}{ek_F}\left[\frac{s_s}{\sinh(s_s x)} - \frac{s_t}{\sinh(s_t x)}\right]; \quad h_{n1}(x) = \frac{1}{2}\left[\frac{s_t x}{\sinh(s_t x)} + \frac{s_s x}{\sinh(s_s x)}\right], \quad (8)$$

$$h_{z2}(x) = \frac{\varepsilon_F}{ek_F}\left[\frac{s_s}{\sinh[s_s(L-x)]} - \frac{s_t}{\sinh[s_t(L-x)]}\right]; \quad h_{n2}(x) = \frac{1}{2}\left[\frac{s_t(L-x)}{\sinh[s_t(L-x)]} + \frac{s_s(L-x)}{\sinh[s_s(L-x)]}\right] \quad (9)$$

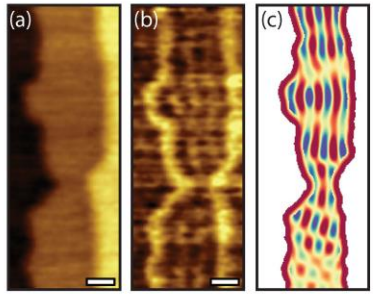

FIG. 2. (a) Topography image (30×12 nm^2, scale bar 3 nm) of Au(111) showing a stepped Au(111) surface. The tunneling parameters are 300 mV and 300 pA. (b) The simultaneously recorded thermovoltage map for $T_T = 293$ K, $T_S = 220$ K, and $\Delta z = 0.3$ nm, showing surface electron interference patterns confined between the steps. (c) Simulated thermovoltage image based on the interference between two Friedel oscillations. The oscillations are simulated using Eq. (7).

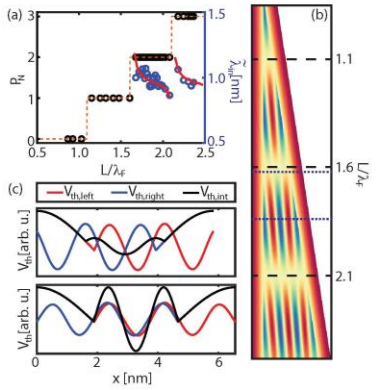

FIG. 3. (a) The number of interference peaks (P_N, left, black) and the peak periodicity ($\tilde{\lambda}_{in} = [2\lambda_{in}/\lambda_F]$, right, blue) as a function of the terrace width (L). The orange (P_N) and red ($\tilde{\lambda}_{in}$) lines are fits based on the model described by Eq. (7). (b) Simulated thermovoltage map [based on Eq. (7)] for an increasing terrace width L. L is varied between 3 and 10 nm. The dashed black lines coincide with the steps in (a). (c) The left (blue line) and right (red line) Friedel oscillation and the resulting interference wave (black line) based on Eq. (7) for (top) $L = 5.9$ nm ($L/\lambda_F = 1.64$) and (bottom) $L = 6.5$ nm ($L/\lambda_F = 1.8$), corresponding to position of the blue dotted line in (b).

*Corresponding author: k.sotthewes@utwente.nl

K. Sotthewes, M. Nijmeijer, H. J. W. Zandvliet, Phys. Rev. B. 103, 245311 (2021)

Figs of Nanotech & Thermal S&E

Jean-Jacques Greffet
Institut d'Optique
Université Paris-Saclay, France

- Ligsystems (mainly 1988-2000)
- Theory of near-field microscopy imaging (1995-2005)
- Thermal radiation at the nanoscale (1997-)
- Nanoantennas (2005-)
- Quantum plasmonics (2009-)
- Light emitting metasurfaces (2018-ht scattering by periodic and random)

Gang Chen
Dept of Mechanical Engineering,
MIT, USA

- nanoscale thermal transport and energy conversion phenomena
- applications in energy storage and conversion,
- thermal management
- water treatment and desalination

Arun Majumdar, Depts of Mechanical Engineering, Energy Science and Engineering, Stanford, USA

- S & T of nanoscale materials and devices,
- energy conversion, transport and storage
- biomolecular analysis.
- redox reactions and systems to a sustainable energy future
- multidimensional nanoscale imaging and microscopy
- AI techniques to develop and deliver energy and climate solutions.

Greffet and Chen started their ventures on NFRHT since 2000, after our attempts in 1990's, with successful results

Radiative Heat Transfer between Sphere and Substrate

APPLIED PHYSICS LETTERS VOLUME 78, NUMBER 19 7 MAY 2001

Nanoscale radiative heat transfer between a small particle and a plane surface

Jean-Philippe Mulet,[a] Karl Joulain, Rémi Carminati, and Jean-Jacques Greffet
Laboratoire d'Energétique Moléculaire et Macroscopique, Combustion, Ecole Centrale Paris, Centre National de la Recherche Scientifique, 92295, Châtenay-Malabry Cedex, France

(Received 20 December 2000; accepted for publication 7 March 2001)

We study the radiative heat transfer between a small dielectric particle, considered as a point-like dipole, and a surface. In the framework of electrodynamics and using the fluctuation-dissipation theorem, we can evaluate the energy exchange in the near field, which is dominated by the contribution of tunneling waves. The transfer is enhanced by several orders of magnitude if the surface or the particle can support resonant surface waves. An application to local heating is discussed. © *2001 American Institute of Physics.* [DOI: 10.1063/1.1370118]

Questions about radiative heat transfer (RHT) at nanoscales have been raised by recent developments of nanotechnology.[1] Design of micro- and nanostructures requires a thorough understanding of physical phenomena involved in radiative energy exchange, when their sizes become comparable to the thermal mean free path or the thermal radiation wavelength.[2,3] Modeling RHT between two semi-infinite bodies[4–7] or between a tip and a substrate[8] is a challenging problem for all near-field microscopes (scanning tuneling microscope, atomic force microscope) or for scanning thermal microscopes.[9] Our work deals with the problem of RHT between a small particle—considered as a point-like dipole—and a very close plane interface. This particle could be a single molecule, a dust particle, or a model for the tip of a microscope probe. Using an electromagnetic approach, in the dipolar approximation, we have derived the expression of the radiative heat power exchanged between the particle and the semi-infinite medium. We show that the transfer increases at small distances and can be enhanced by several orders of magnitude (in comparison with the transfer at large distances) if the particle or the bulk support resonant surface waves. Results of numerical simulations are presented and an application to local heating is discussed.

In this part, we focus on the derivation of the radiative power exchanged between a small particle (of spherical shape) and a semi-infinite medium. The geometry of the problem is presented in Fig. 1: the upper medium $z>0$ is vacuum ($\varepsilon=1$). A particle (P) of radius a and dielectric constant (frequency dependent) $\varepsilon_P(\omega)=\varepsilon'_P(\omega)+i\varepsilon''_P(\omega)$ is held at temperature T_P. The lower medium $z<0$, is filled by a homogeneous, isotropic material (bulk) of dielectric constant $\varepsilon_B(\omega)=\varepsilon'_B(\omega)+i\varepsilon''_B(\omega)$ and held at temperature T_B. The center of the particle is at a distance d above the interface.

We first calculate the mean power $P_{\rm abs}^{B\to P}(\omega)$ radiated by the bulk at a given frequency ω and absorbed by the particle. We assume that the bulk is in local thermodynamic equilibrium at uniform temperature $T_B\neq 0$, so that there are fluctuating currents inside the bulk due to thermal fluctuations. These currents inside the bulk radiate an electromagnetic field that illuminates the particle. An elementary fluctuating current $\mathbf{j}_f(\mathbf{r}',\omega)$ at frequency ω, radiates at point $\mathbf{r}$ inside the particle, an incident electric field $\mathbf{E}_{\rm inc}(\mathbf{r},\omega)$ given by

$$\mathbf{E}_{\rm inc}(\mathbf{r},\omega)=(i\omega\mu_0)\int_B \vec{\mathbf{G}}(\mathbf{r},\mathbf{r}',\omega)\mathbf{j}_f(\mathbf{r}',\omega)d^3\mathbf{r}', \quad (1)$$

where μ_0 is the magnetic permeability of vacuum and $\vec{\mathbf{G}}$ is the Green tensor[10] of a system constituted by two semi-infinite media whose dielectric constants are either 1 if $z\geqslant 0$ or $\varepsilon_B(\omega)$ if $z<0$. Let us now assume that $\mathbf{E}_{\rm inc}(\mathbf{r},\omega)$ is uniform inside the particle. This amounts to use a dipolar approximation, whose validity in the near field has already been discussed.[11] Provided that this condition is satisfied, the small particle behaves as a point-like dipole $\mathbf{p}_{\rm ind}(\mathbf{r}_P,\omega)$ induced by the incident field $\mathbf{E}_{\rm inc}(\mathbf{r}_P,\omega)$. These quantities are related by: $\mathbf{p}_{\rm ind}(\mathbf{r}_P,\omega)=\varepsilon_0\alpha(\omega)\mathbf{E}_{\rm inc}(\mathbf{r}_P,\omega)$, where ε_0 is the dielectric permittivity of vacuum and $\alpha(\omega)$ is the particle polarizability. For a spherical particle of dielectric constant $\varepsilon_P(\omega)$, we used the Clausius–Mossotti polarizability[12]

$$\alpha(\omega)=4\pi a^3\left[\frac{\varepsilon_P(\omega)-1}{\varepsilon_P(\omega)+2}\right]. \quad (2)$$

A more precise model,[13] taking into account the interaction between the dipole and its image through the interface, leads to the introduction of an effective polarizability. We have verified that, when the distance d is larger than the particle radius a, the correction to Eq. (2) is negligible. Since

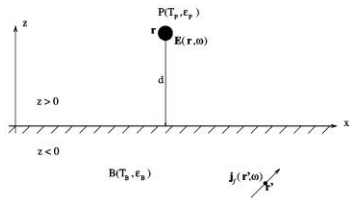

FIG. 1. Geometry of the system.

[a]Electronic mail: jpmulet@em2c.ecp.fr

0003-6951/2001/78(19)/2931/3/$18.00

we did our calculation for a distance d larger than $2a$, we will consider that Eq. (2) is a good approximation for the polarizability in our problem.

We now evaluate the mean radiative power $P_{\rm abs}^{B\to P}(\omega)$ dissipated inside the particle. Since the scattered power is negligible,[14] this quantity is given by: $P_{\rm abs}^{B\to P}(\omega)=\mathrm{Re}\{\langle -i\omega\mathbf{p}_{\rm ind}(\mathbf{r}_P,\omega)\cdot\mathbf{E}^*_{\rm inc}(\mathbf{r}_P,\omega)\rangle\}$, where the brackets denote a statistical ensemble average over the fluctuations of the currents inside the bulk. The components $\langle|E_{{\rm ind},i}(\mathbf{r}_P,\omega)|^2\rangle$ $(i=x,y,z)$ depend only on the distance d and are given by[10,15,16]

$$\langle|E_{{\rm inc},i}(\mathbf{r}_P,\omega)|^2\rangle=2\frac{\mu_0^2\varepsilon_0\omega^3}{\pi}\mathrm{Im}[\varepsilon_B(\omega)]\Theta(\omega,T_B)\times\sum_{j=x,y,z}\int_B|G_{i,j}(\mathbf{r}_P,\mathbf{r}',\omega)|^2d^3\mathbf{r}', \quad (3)$$

where $\Theta(\omega,T_B)=\hbar\omega/[\exp(\hbar\omega/k_BT_B)-1]$ is the mean energy of a quantum oscillator in thermal equilibrium at temperature T_B, $2\pi\hbar$ is Planck's constant, and k_B is Boltzmann's constant. Finally, we find the expression of the mean power radiated by the bulk and absorbed by the particle at frequency ω

$$P_{\rm abs}^{B\to P}(\mathbf{r}_P,\omega)=\frac{2}{\pi}\frac{\omega^4}{c^4}\mathrm{Im}[\varepsilon_B(\omega)]\mathrm{Im}[\alpha(\omega)]\Theta(\omega,T_B)\times\sum_{i,j=x,y,z}\int_B|G_{i,j}(\mathbf{r}_P,\mathbf{r}',\omega)|^2d^3\mathbf{r}'. \quad (4)$$

We now consider the fluctuating currents inside the particle at temperature T_P that illuminate the bulk. Using the same formalism, we can calculate the power *locally* dissipated per unit volume, at a point $\mathbf{r}$ inside the bulk, by the following relation: $P_{\rm abs}^{P\to B}(\mathbf{r},\omega)=\mathrm{Re}\{\langle\mathbf{j}_{\rm ind}(\mathbf{r},\omega)\cdot\mathbf{E}^*_{\rm inc}(\mathbf{r},\omega)\rangle\}$. It reads

$$P_{\rm abs}^{P\to B}(\mathbf{r},\omega)=\frac{2}{\pi}\frac{\omega^4}{c^4}\mathrm{Im}[\varepsilon_B(\omega)]\mathrm{Im}[\alpha(\omega)]\Theta(\omega,T_P)\times\sum_{i,j=x,y,z}|G_{i,j}(\mathbf{r},\mathbf{r}_P,\omega)|^2. \quad (5)$$

In this part, we present some numerical results obtained with a particle and a surface of silicon carbide (SiC). The optical properties of this material can be described using an oscillator model[17]

$$\varepsilon_B(\omega)=\varepsilon_P(\omega)=\varepsilon(\omega)=\varepsilon_\infty\left(1+\frac{\omega_L^2-\omega_T^2}{\omega_T^2-\omega^2-i\Gamma\omega}\right) \quad (6)$$

with $\varepsilon_\infty=6.7$, $\omega_L=969\,\mathrm{cm}^{-1}$, $\omega_T=793\,\mathrm{cm}^{-1}$, and $\Gamma=4.76\,\mathrm{s}^{-1}$. The bulk can support resonant surface waves, called surface phonon polaritons, that produce a peak in the density of states at frequency ω_B where $\varepsilon(\omega_B)$ satisfies the relation $\varepsilon'(\omega_B)=-1$. The spherical particle supports volume phonon polaritons at ω_P where $\varepsilon(\omega_P)$ satisfies the relation $\varepsilon'(\omega_P)=-2$. Using Eq. (6), we find: $\omega_B=178.7\times10^{12}\,\mathrm{rad\,s}^{-1}$ and $\omega_P=175.6\times10^{12}\,\mathrm{rad\,s}^{-1}$.

In Fig. 2, we plot $P_{\rm abs}^{B\to P}(\omega)$ for a spherical particle of radius $a=5$ nm at different distances d above the surface.

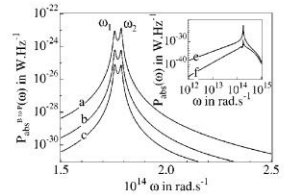

FIG. 2. Mean power radiated by the bulk (at $T_B=300$ K) and absorbed by the particle (of radius $a=5$ nm) vs frequency: (a) $d=20$ nm; (b) $d=50$ nm; (c) $d=100$ nm. The inset (log–log scale) shows the spectrum of the absorbed power between 10^{12} and $10^{15}\,\mathrm{rad\,s}^{-1}$; (e) $d=20$ nm; and (f) $d=1$ mm.

held at temperature $T_B=300$ K. We note that the figure displays two remarkable peaks at frequency $\omega_1\approx175.6\times10^{12}\,\mathrm{rad\,s}^{-1}$ and $\omega_2\approx178.7\times10^{12}\,\mathrm{rad\,s}^{-1}$. These two peaks are related to the resonant surface waves: the first corresponds to the resonance of the particle which presents a larger absorption at this frequency; the second is due to a huge increase of electromagnetic energy density close to the surface, demonstrated recently.[16] An asymptotic expansion of Eq. (4) for small distance d yields the radiative power spectrum

$$P_{\rm abs}^{B\to P}(d,\omega)\sim\frac{1}{4\pi^2d^3}\times4\pi a^3\underbrace{\frac{3\varepsilon''(\omega)}{|\varepsilon(\omega)+2|^2}}_{\text{particle}}\underbrace{\frac{\varepsilon''(\omega)}{|\varepsilon(\omega)+1|^2}}_{\text{bulk}}\Theta(\omega,T_B). \quad (7)$$

At this point, we must emphasize that, whereas those surface waves are evanescent waves, an energy exchange between the bulk and the particle takes place because the particle lies in the region (up to many micrometers) where the evanescent field is large, so that there is an efficient coupling between them. The inset of the figure shows (in log–log scale) the spectrum of the absorbed power between 10^{12} and $10^{15}\,\mathrm{rad\,s}^{-1}$ at two different distances $d=20$ nm and $d=1$ mm. It is seen that the RHT is almost monochromatic and is larger in the near field. If the particle and the bulk

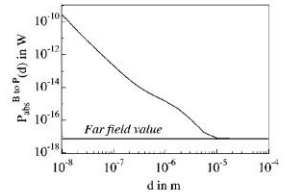

FIG. 3. Total power radiated by the bulk (at $T_B=300$ K) and absorbed by the particle (of radius $a=5$ nm) vs distance.

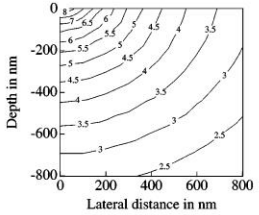

FIG. 4. Deposited power per unit volume inside the bulk. The particle has a radius $a=5$ nm and is held at temperature $T_P=300$ K.

were constituted by two different materials, the RHT spectrum would feature two separate sharp peaks at two different resonance frequencies.

Figure 3 shows the integrated power absorbed by the same particle versus distance d (the substrate is still held at temperature $T_B=300$ K). The near-field RHT increases as $1/d^3$ and is larger at small distances by several orders of magnitude than the far-field one. Indeed, for $d=10$ nm, $P_{\rm abs}\approx2.6\times10^{-10}$ W and for $d=10\,\mu$m, $P_{\rm abs}\approx8.9\times10^{-18}$ W. This enhancement comes from the contribution of evanescent waves to the energy exchange. Therefore, this contribution cannot be neglected in a near-field calculation. This phenomenon occurs when the materials can support resonant surface waves like III–V or II–VI semiconductors and because the resonant frequencies take place in the far IR region (up to 10 μm) where the characteristic wavelength of thermal emission at $T\approx300$ K is 10 μm. A lot of materials, like oxides or glass, can also support resonant surface waves in the IR or the visible region.

Reciprocity requires that the same enhanced RHT appears when the particle illuminates the surface. This situation may help us in understanding the radiative heat exchange between a nanotip (like those used in near-field microscopy) and a sample. It is interesting to study how the energy radiated by the tip is dissipated in the sample. To answer this question, we calculated—using Eq. (5)—the total power (integrated over the frequencies) dissipated per unit volume for different points in the sample. Figure 4 displays a map, in log scale, of the dissipation rate in the case of a 10 nm diameter sphere of SiC at $T_P=300$ K situated at 100 nm above a sample of SiC. It is seen that the energy is dissipated on a scale comparable to the tip–sample distance. The dissipation per unit volume decreases very fast (as $1/r^6$) with the distance r between the source and the point of the sample where the dissipation is considered (the isocontour labeled with a "6" corresponds to the points where the dissipation per unit volume is $10^6\,\mathrm{W\,m}^{-3}$). The amount of energy locally deposited is as large as $100\,\mathrm{MW\,m}^{-3}$.

In this letter, we have shown that nanoscale RHT between a sample and a small particle is almost monochromatic and can be enhanced by several orders of magnitude when the materials involved support resonant surface waves. When illuminated by the particle, the distribution of power inside the sample extends over distances of the same order as the particle-sample separation. These results should have broad applications in near-field microscopy, in design of nanostructures and in high density storage processes by local heating.

[1] A. R. Abramson and C. L. Tien, Microscale Thermophys. Eng. **3**, 229 (1999).
[2] G. Chen, Microscale Thermophys. Eng. **1**, 215 (1997).
[3] J. B. Pendry, J. Mod. Opt. **45**, 2389 (1998).
[4] E. G. Cravalho, C. L. Tien, and R. P. Caren, J. Heat Transfer **89**, 351 (1967).
[5] C. M. Hargreaves, Phys. Rev. Lett. **30A**, 491 (1969).
[6] D. Polder and M. Van Hove, Phys. Rev. B **4**, 3303 (1971).
[7] J. L. Loomis and H. J. Maris, Phys. Rev. B **50**, 18 517 (1994).
[8] K. Dransfeld and J. Xu, J. Microsc. **152**, 35 (1988).
[9] C. C. Williams and H. K. Wickramasinghe, Appl. Phys. Lett. **49**, 1587 (1986).
[10] R. Carminati and J. J. Greffet, Phys. Rev. Lett. **82**, 1660 (1999).
[11] P. C. Chaumet, A. Rahmani, F. de Fornel, and J. P. Dufour, Phys. Rev. B **58**, 2310 (1998).
[12] J. D. Jackson, *Classical Electrodynamics*, 2nd Ed. (Wiley, New York, 1975), Sec. 4.4.
[13] F. Pincemin, A. Sentenac, and J. J. Greffet, J. Opt. Soc. Am. A **11**, 1117 (1994).
[14] B. T. Draine, Astrophys. J. **333**, 848 (1988).
[15] S. M. Rytov, Yu. A. Kravtsov, and V. I. Tatarskii, *Principles of Statistical Radiophysics* (Springer, Berlin, 1989).
[16] A. V. Shchegrov, K. Joulain, R. Carminati, and J. J. Greffet, Phys. Rev. Lett. **85**, 1548 (2000).
[17] E. W. Palik, *Handbook of Optical Constants of Solids* (Academic, San Diego, CA, 1985).

J. P. Mulet, K. Joulain, R. Carminati, J. J. Greffet, Appl. Phys. Lett. 78, 2931–2933 (2001)

Near-Field Heat Transfer in a SThM

Near-Field Heat Transfer in a Scanning Thermal Microscope

Achim Kittel, Wolfgang Müller-Hirsch, Jürgen Parisi, Svend-Age Biehs, Daniel Reddig, and Martin Holthaus
Institut für Physik, Carl von Ossietzky Universität, D-26111 Oldenburg, Germany
(Received 14 July 2005; published 22 November 2005)

We present measurements of the near-field heat transfer between the tip of a thermal profiler and planar material surfaces under ultrahigh vacuum conditions. For tip-sample distances below 10^{-8} m, our results differ markedly from the prediction of fluctuating electrodynamics. We argue that these differences are due to the existence of a material-dependent small length scale below which the macroscopic description of the dielectric properties fails, and discuss a heuristic model which yields fair agreement with the available data. These results are of importance for the quantitative interpretation of signals obtained by scanning thermal microscopes capable of detecting local temperature variations on surfaces.

DOI: 10.1103/PhysRevLett.95.224301 PACS numbers: 05.40.−a, 03.50.De, 44.40.+a, 78.20.Ci

Radiative heat transfer between macroscopic bodies increases strongly when their spacing is made smaller than the dominant wavelength λ_{th} of thermal radiation. This effect, caused by evanescent electromagnetic fields existing close to the surface of the bodies, was already studied theoretically in 1971 by Polder and van Hove for the model of two infinitely extended, planar surfaces separated by a vacuum gap [1], and was reinvestigated later by Loomis and Maris [2] and Volokitin and Persson [3,4]. While early pioneering measurements with flat chromium bodies had to remain restricted to gap widths above 1 μm [5], and later studies employing an indium needle in close proximity to a planar thermocouple remained inconclusive [6], an unambiguous demonstration of near-field heat transfer under ultrahigh vacuum conditions, and thus in the absence of disturbing moisture films covering the surfaces, was given in Ref. [7].

The theoretical treatment of radiative near-field heat transfer is based on fluctuating electrodynamics [8]. Within this framework, the macroscopic Maxwell equations are augmented by fluctuating currents inside each body, constituting stochastic sources of the electric and magnetic fields $\mathbf{E}$ and $\mathbf{H}$. The individual frequency components $\mathbf{j}(\mathbf{r},\omega)$ of these currents are considered as Gaussian stochastic variables. According to the fluctuation-dissipation theorem, their correlation function reads [9]

$$\langle j_\alpha(\mathbf{r},\omega) j^*_\beta(\mathbf{r}',\omega')\rangle = \frac{\omega}{\pi} E(\omega,\beta)\epsilon''(\omega)\delta_{\alpha\beta}\delta(\mathbf{r}-\mathbf{r}') \times \delta(\omega-\omega'), \quad (1)$$

where $E(\omega,\beta) = \hbar\omega/[\exp(\beta\hbar\omega)-1]$, with the usual inverse temperature variable $\beta = 1/(k_B T)$; the angular brackets indicate an ensemble average. Moreover, $\epsilon''(\omega)$ denotes the imaginary part of the complex dielectric function $\epsilon(\omega) = \epsilon'(\omega) + i\epsilon''(\omega)$. It describes the dissipative properties of the material under consideration, which is assumed to be homogeneous and nonmagnetic. Thus, Eq. (1) contains the idealization that stochastic sources residing at different points $\mathbf{r}$, $\mathbf{r}'$ are uncorrelated, no matter how small their distance may be. Applied to a material occupying the half-space $z<0$, facing the vacuum in the complementary half-space $z>0$, these propositions can be evaluated to yield the electromagnetic energy density in the distance z above the surface, giving [10]

$$\begin{aligned}\langle u(z)\rangle &= \frac{\epsilon_0}{2}\langle \mathbf{E}^2\rangle + \frac{\mu_0}{2}\langle \mathbf{H}^2\rangle \\ &= \int_0^\infty d\omega \int_0^\infty d\kappa[\rho_{\mathbf{E}}(\omega,\kappa,\beta,z) + \rho_{\mathbf{H}}(\omega,\kappa,\beta,z)] \\ &= \int_0^\infty d\omega \frac{E(\omega,\beta)\omega^2}{2\pi^2 c^3} \\ &\quad\times\left\{\int_0^1 d\kappa \frac{\kappa}{p}[1+\kappa^2\,\mathrm{Re}(r_\parallel e^{2iz\omega p/c})] \right. \\ &\quad\left. + \int_1^\infty d\kappa \frac{\kappa^3}{|p|}\,\mathrm{Im}(r_\parallel) e^{-2z\omega|p|/c} + X_\perp\right\}. \end{aligned} \quad (2)$$

Here, the densities $\rho_{\mathbf{E}}$ and $\rho_{\mathbf{H}}$ symbolically specify the electric and magnetic contribution, respectively; $r_\parallel$ denotes the Fresnel amplitude reflection coefficient for TM modes with a wave vector of magnitude $\omega\kappa/c$ parallel to the surface. The symbol $X_\perp$ abbreviates the corresponding terms for TE modes. The wave vector oriented normal to the surface, of magnitude $\omega p/c$, distinguishes propagating modes with real $p = \sqrt{1-\kappa^2}$ for $\kappa \le 1$ from evanescent modes with imaginary $p = i\sqrt{\kappa^2-1}$ for $\kappa > 1$.

Expression (2) for the energy density, obtained strictly within the framework of macroscopic electrodynamics, diverges for small distances z from the surface; for $z/\lambda_{\text{th}} \ll 1$, one finds the power law $\langle u(z)\rangle \propto z^{-3}$ [8]. Hence, it has been suggested that also the energy dissipated in the tip of a tiny probe close to the surface should scale inversely proportional to the cube of the tip-sample distance [11,12]. However, the entailing divergence clearly is not borne out by the actual physics [13–15]. The divergence may formally be avoided by replacing the upper boundary of integration, $\kappa = \infty$ in Eq. (2), by a finite cutoff κ_c, thereby excluding the problematic large-wave number contributions to the "evanescent" part of the energy density.

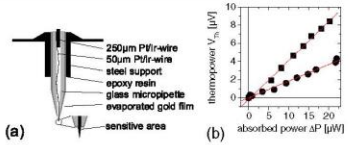

FIG. 1 (color online). (a) Cross section of the micropipette glued into a tip holder. The thermoelectric voltage V_{th} builds up between the inner platinum wire and the outer gold film. The tunnel potential is applied between the sample and the grounded gold film. (b) Dependence of the thermovoltage on the absorbed power ΔP of calibrating laser light for two different sensors.

ficient of the scanner. Results of such measurements are depicted in Fig. 2 for a sample consisting of a gold layer, and in Fig. 3 for a sample of GaN. In both cases, the sensor with $R_{\text{th}} = 54$ K/mW has been employed. During these measurements, we have carefully checked that the cross talk between the tunnel current signal and the thermovoltage remains negligibly small. The absence of interference is indicated by the fact that the tunnel current decreases strongly in a range of distances where the observed thermovoltage stays almost constant.

A theoretical discussion of the heat transfer between an idealized tip and a flat surface, which may serve as a guideline for the analysis of our data, has been given by Mulet *et al.* [12]. These authors have modeled the tip by a small dielectric sphere of radius r and assumed the incident electric field to be uniform inside the sphere, so that it acts as a pointlike dipole. If the temperature of the sample is significantly lower than that of the tip, as in our case, the heat current flowing back from the sample to the tip can be neglected. The total flux between the surface and the tip then is determined entirely by the current directed from the tip to the sample, according to

$$\Delta P = \int_0^\infty d\omega \int_0^\infty d\kappa\alpha(\omega)\rho_{\mathbf{E}}(\omega,\kappa,\beta,z), \quad (3)$$

where $\alpha(\omega) = 2\omega(4\pi r^3)\epsilon''_{\text{tip}}/|\epsilon_{\text{tip}}+2|^2$ describes the dielectric properties of the sphere, and the temperature entering $\rho_{\mathbf{E}}$ is that of the tip. Taking this expression at a representative frequency ω_0, one has $\Delta P \approx \alpha(\omega_0)\epsilon_0\langle \mathbf{E}^2\rangle/2$, so that, within the scope of the model, the heat flux registered by the tip should be proportional to the electrical energy density of the flat sample, evaluated, however, at the temperature of the tip.

For distances larger than about 10^{-8} m, our experimentally observed heat transfer is, to good accuracy, proportional to the *total* energy density as given by Eq. (2), not to the electric field contribution alone. Since the constant of proportionality, which carries the dimension of area times velocity, may differ substantially from $\alpha(\omega_0)$, we focus on the scaled energy density $\Delta P_{\text{th}} := \pi a^2 c\langle u(z)\rangle$, where c is the velocity of light, and employ the effective sensor area πa^2 as a fitting parameter. Modeling the dielectric function $\epsilon(\omega)$ for Au by a Drude ansatz with parameters taken from Ref. [19], and that for GaN by the "reststrahlen" formula with parameters from Ref. [20], we obtain the dashed lines in Figs. 2 and 3, setting $a = 60$ nm. This value is in accordance with scanning electron microscopy studies of the tip and describes *both* experimental data sets for $z \gtrsim 10$ nm, as it should. The latter fact also indicates that the use of Eq. (2), i.e., the neglect of the field's distortion by the tip, is justified here.

In the case of GaN, the theoretical curve for ΔP_{th} diverges as z^{-3} for sensor-sample distances below 10 nm. In contrast, for Au this familiar behavior would become apparent only at substantially smaller z [3]. However, the experimental data clearly show a different trend, leveling off to values which for the smallest accessible distances are significantly lower than ΔP_{th}. We interpret this finding as

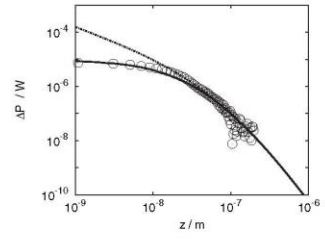

FIG. 2. Measured heat current ΔP (in Watts) between the microscope tip and a gold layer (circles) vs tip-sample distance z. The dashed line, which coincides with the solid one for larger z, corresponds to the prediction ΔP_{th} of standard fluctuating electrodynamics, based on Eq. (2). The solid line is obtained from Eq. (5) with the modified dielectric function (4), setting $L = L_{\text{tip}} = 1.2\times10^{-8}$ m.

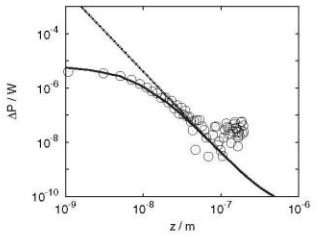

FIG. 3. As Fig. 2 for a sample of GaN, setting $L = 1.0\times10^{-10}$ m and $L_{\text{tip}} = 1.2\times10^{-8}$ m.

evidence for the short-distance deficiency of the macroscopic theory, as expressed by the deltalike correlation function (1) of the stochastic source currents: In a real sample, there is some finite correlation length L.

In principle, one should then also account for nonlocal effects, which requires distinguishing a transversal and a longitudinal part of the permittivity [21]. We do not resort to the systematic theory of such effects here, but propose a qualitative approach: Since it appears necessary to smooth out the correlation function (1) on short distances, one might introduce an appropriate modification of the imaginary part of $\epsilon(\omega)$. However, then the Kramers-Kronig relation requires a corresponding modification of the real part. Hence, a heuristically motivated, plausible ansatz for an effective permittivity depending explicitly on the transversal wave number is

$$\bar{\epsilon}(\omega,\kappa) := 1 + [\epsilon'(\omega)-1]f(\kappa) + i\epsilon''(\omega)f(\kappa), \quad (4)$$

where the function $f(\kappa)$ accounts for the lateral correlations, such that it approaches unity and thereby restores the local case when $\omega\kappa/c \ll L^{-1}$, but vanishes for large-wave numbers, when $\omega\kappa/c \gg L^{-1}$. As a convenient guess, we take a Gaussian $f(\kappa) = \exp[-(L\omega\kappa/c)^2]$ and consider L as a parameter to be determined by fitting the data. When evaluating the Maxwell equations for systems with plane translational invariance [1], we replace $\epsilon(\omega)$ by $\bar{\epsilon}(\omega,\kappa)$. The energy density can then again be obtained from Eq. (2), if the reflection coefficients $r_\parallel$ and $r_\perp$ are adapted in this manner.

Besides the dielectric properties of the sample, also those of the sensor enter into the data, as exemplified by the dipole model (3). Hence, we have to introduce both a correlation length L of the sample and a further correlation length L_{tip} of the sensor, and parametrize the experimentally observed heat current in the form

$$\frac{\widetilde{\Delta P}}{\pi a^2 c} = \int_0^\infty d\omega \int_0^\infty d\kappa e^{-(L_{\text{tip}}\omega\kappa/c)^2} \times[\rho_{\mathbf{E}}(\omega,\kappa) + \rho_{\mathbf{H}}(\omega,\kappa)]. \quad (5)$$

Using this ansatz (5), we finally obtain the solid curves in Figs. 2 and 3, setting $L = 1.2\times10^{-8}$ m for Au and $L = 1.0\times10^{-10}$ m for GaN, while $L_{\text{tip}} = 1.2\times10^{-8}$ m in both cases. These curves capture the experimental data quite well, thus lending strong support to our line of reasoning. It is also encouraging to observe that the numerical value of L obtained for Au indeed turns out to be on the order of the mean free path of electrons in metals, whereas that for GaN is considerably shorter, as it should. Although the thermally relevant component of our sensor probably is confined to the Au layer, its correlation length does not necessarily have to coincide with that of the gold sample, as it actually does in our case, but might be geometrically restricted in alternative setups.

In summary, we have obtained experimental data for the near-field heat transfer between a thermal profiler and flat material surfaces under UHV conditions. We have reached the extreme near-field regime, where the variation of the heat transfer rate with the distance between microscope tip and sample differs distinctly from the divergent behavior predicted by standard macroscopic fluctuating electrodynamics, and have interpreted our observations in terms of finite microscopic correlations inside the materials. While the shortcomings of the macroscopic theory are, in principle, well known [8,9], their manifestation in an actual experiment indicates a still unexplored potential of thermal microscopy as a new, quantitative tool for the nanometer-scale investigation of solids.

[1] D. Polder and M. van Hove, Phys. Rev. B **4**, 3303 (1971).
[2] J.J. Loomis and H.J. Maris, Phys. Rev. B **50**, 18517 (1994).
[3] A.I. Volokitin and B.N.J. Persson, Phys. Rev. B **63**, 205404 (2001).
[4] A.I. Volokitin and B.N.J. Persson, Phys. Rev. B **69**, 045417 (2004).
[5] C.M. Hargreaves, Phys. Lett. **30A**, 491 (1969).
[6] J.-B. Xu, K. Läuger, R. Möller, K. Dransfeld, and I.H. Wilson, J. Appl. Phys. **76**, 7209 (1994).
[7] W. Müller-Hirsch, A. Kraft, M. Hirsch, J. Parisi, and A. Kittel, J. Vac. Sci. Technol. A **17**, 1205 (1999).
[8] S.M. Rytov, Yu.A. Kravtsov, and V.I. Tatarskii, *Principles of Statistical Radiophysics* (Springer, New York, 1989), Vol. 3.
[9] E.M. Lifshitz and L.P. Pitaevskii, *Statistical Physics*, Landau-Lifshitz, Course of Theoretical Physics Vol. 9, Pt. 2 (Butterworth-Heinemann, Oxford, 2002).
[10] K. Joulain, R. Carminati, J.-P. Mulet, and J.-J. Greffet, Phys. Rev. B **68**, 245405 (2003).
[11] I.A. Dorofeyev, J. Phys. D **31**, 600 (1998).
[12] J.-P. Mulet, K. Joulain, R. Carminati, and J.-J. Greffet, Appl. Phys. Lett. **78**, 2931 (2001).
[13] J.L. Pan, Opt. Lett. **25**, 369 (2000).
[14] J.-P. Mulet, K. Joulain, R. Carminati, and J.-J. Greffet, Opt. Lett. **26**, 480 (2001).
[15] J.L. Pan, Opt. Lett. **26**, 482 (2001).
[16] L. Libioulle, Y. Houbion, and J.M. Gilles, Rev. Sci. Instrum. **66**, 97 (1995).
[17] M. Gotoh, K.D. Hill, and E.G. Murdock, Rev. Sci. Instrum. **62**, 2778 (1991).
[18] J. Bass, J. Dugdale, C. Foiles, and A. Myers, in *Electrical Resistivity, Thermoelectrical Power and Optical Properties*, Landolt-Bornstein, Metals: Electronic Transport Phenomena, Group III, Vol. 15, Pt. b (Springer, Berlin, 1985).
[19] N.W. Ashcroft and N.D. Mermin, *Solid State Physics* (Harcourt, Fort Worth, 1976).
[20] S. Adachi, *Handbook on Physical Properties of Semiconductors* (Kluwer, Boston, 2004).
[21] V. Ginzburg, *Applications of Electrodynamics in Theoretical Physics and Astrophysics* (Gordon and Breach, New York, 1989).

A. Kittel, W. Müller-Hirsch, J. Parisi, S. A. Biehs, D. Reddig, M. Holthaus, Phys. Rev. Lett. 95 (22), Art. No. 224301, (Nov. 2005)

Proof of NFRHT within sub-μm

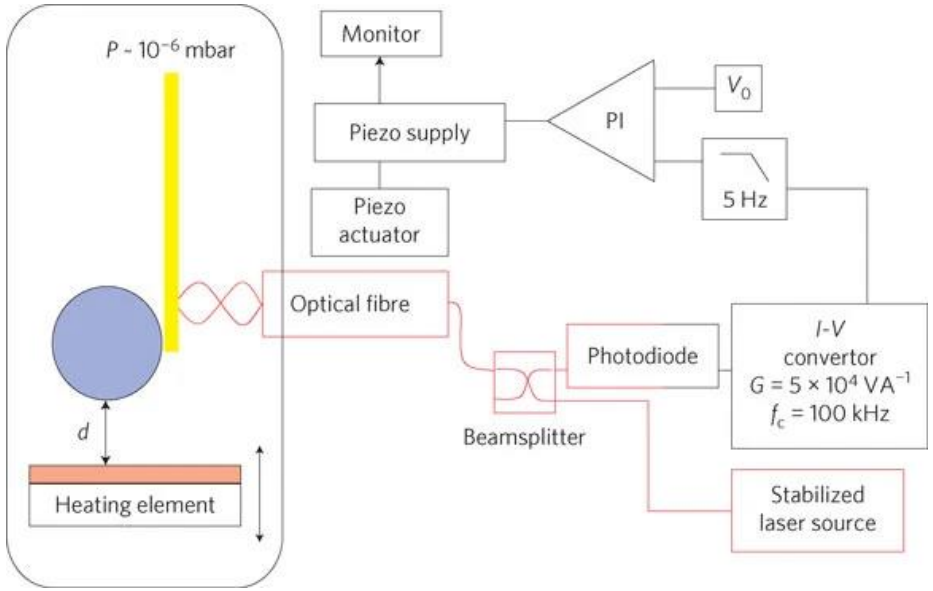

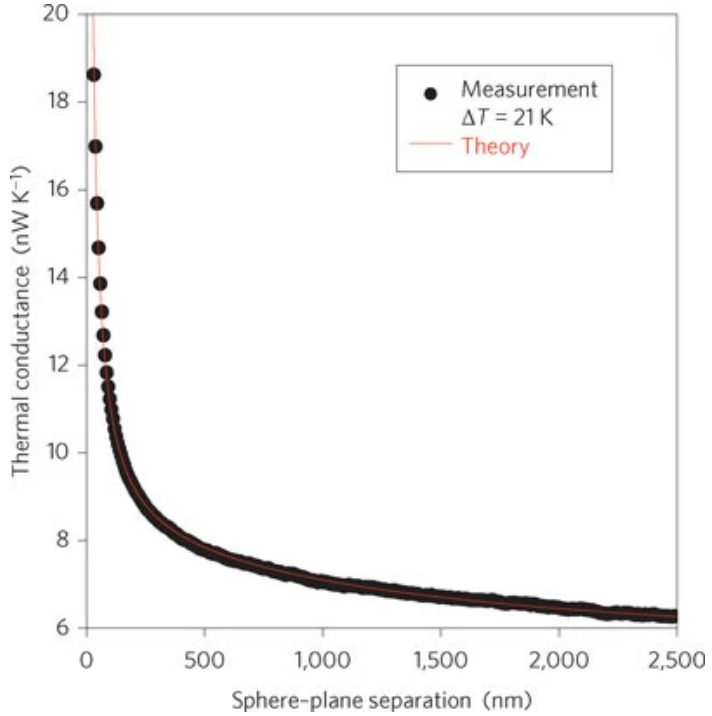

(Red lines are used for the optical part and black lines for the electrical part of the setup.) Reflection of the laser beam on the cantilever produces an interference pattern. A feedback loop keeps the bimorph–optical fibre distance constant by applying a voltage to a piezoelectric actuator holding the optical fibre. The feedback loop and the thermally stabilized laser maintain spurious heating from the laser constant, and ensure that flux variations are only due to the conductance variations as the separation d is changed, with constant temperature difference ΔT between the sphere and the plate. The plate is heated and mounted on a piezoelectric actuator. The measured signal is the voltage applied to the fibre-actuator supply.

The black dots represent experimental data and the red line the theoretical model. The temperature difference between the plate and the sphere is 21 K. The distance shift used in the comparison is b = 31.8 nm and the cantilever response coefficient used in the comparison is H = 2.162 nW nm^{-1}.

E. Rousseau, A. Siria, G. Jourdan, S. Volz, F. Comin, J. Chevrier & Jean-Jacques Greffet, Radiative heat transfer at the nanoscale, Nature Photonics 3, 514–517 (Aug. 2009)

Proof of NFRHT within sub-μm

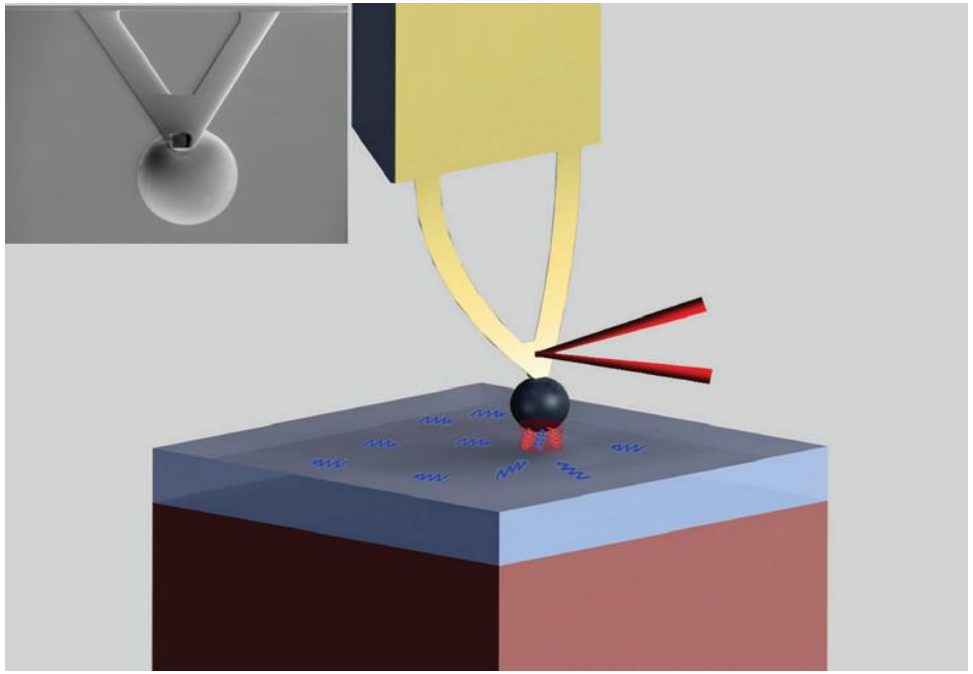

Schematic diagram of experimental setup. The thermal sensor is a silicon nitride AFM cantilever coated with a 70 nm gold film. A laser beam (650 nm wavelength, 3 mW output power) is focused on the tip of the cantilever and reflected onto a PSD. Application of voltage to the piezoelectric translation stage results in the movement of the substrate toward the sphere. In near-field, surface phonon polaritons can tunnel through the gap and they thus significantly contribute to the radiative heat transfer. The "cooling" effect on the cantilever due to the enhanced near-field radiation leads to the bending of the cantilever. Inset: A scanning electron microscope image of a glass sphere mounted on an AFM cantilever.

S. Shen, A. Narayanaswamy, G. Chen, Surface Phonon Polaritons Mediated Energy Transfer between Nanoscale Gaps, Nano Letters 9 (8), 2909-2913 (Aug 2009)

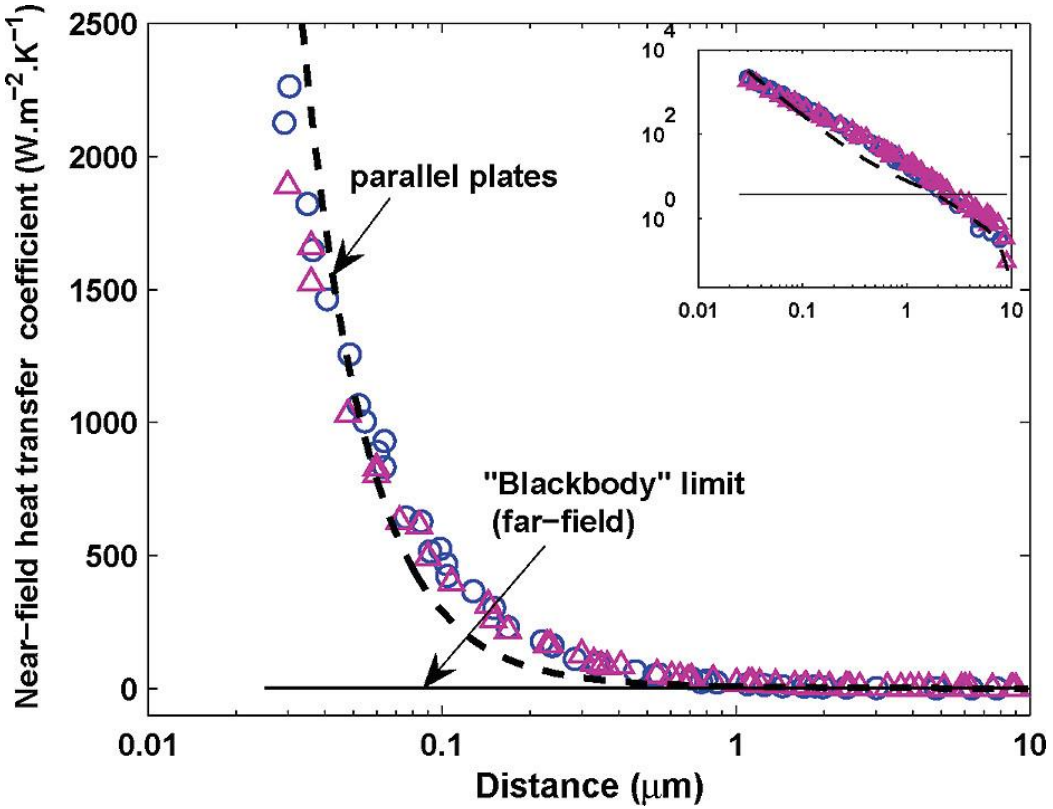

Equivalent sphere−plate near-field heat transfer coefficients normalized to the area 2πRd versus the gap distance for a 100 μm (blue circles) and a 50 μm (violet triangles) diameter sphere. The flat line is the limit predicted by Planck's blackbody radiation law. The dashed line is the near-field heat transfer coefficients obtained after subtracting the far-field part taken from Figure 1C. Inset: the plot on a log−log scale.

Proof of NFRHT within sub-μm

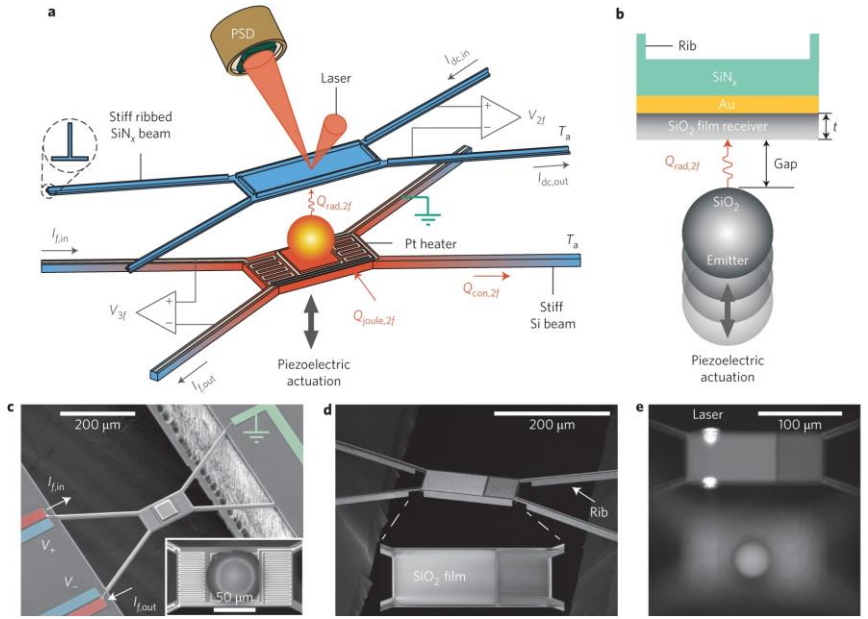

a, Schematic of the experimental set-up. The emitter consists of a suspended silicon platform, with an attached silica sphere and an integrated electrical heater–thermometer. The receiver is a stiff silicon nitride platform coated with gold and a silica film of suitably chosen thickness. A laser (reflected off the receiver, see also e) and a position-sensitive detector (PSD) enable optical detection of emitter–receiver contact formation with nanometre resolution. A sinusoidal electrical current (If,in = If,out), at f = 1 Hz, is supplied to the emitter's resistor, resulting in Joule heating with amplitude Qjoule,2f and frequency 2 Hz. This is partly conducted through the beams (Qcon,2f) and partly radiated to the emitter (Qrad,2f). The emitter's temperature oscillations are quantified by measuring the third harmonic of the voltage (V3f) across the resistor. The receiver's temperature oscillations are measured by supplying a dc current (Idc,in = Idc,out) through the receiver's resistor and by monitoring the voltage output at 2f (V2f) across it. Ta is the ambient temperature. b, Schematic cross-section of the planar receiver region and the spherical silica emitter. The gold layer is ~100 nm thick, and the thickness t of the SiO2 film varies from 50 nm to 3 μm for different receiver devices.

Bai Song, P. Reddy & Edgar Meyhofer, et al. Nature Nanotechnology 10, 253–258 (2015)

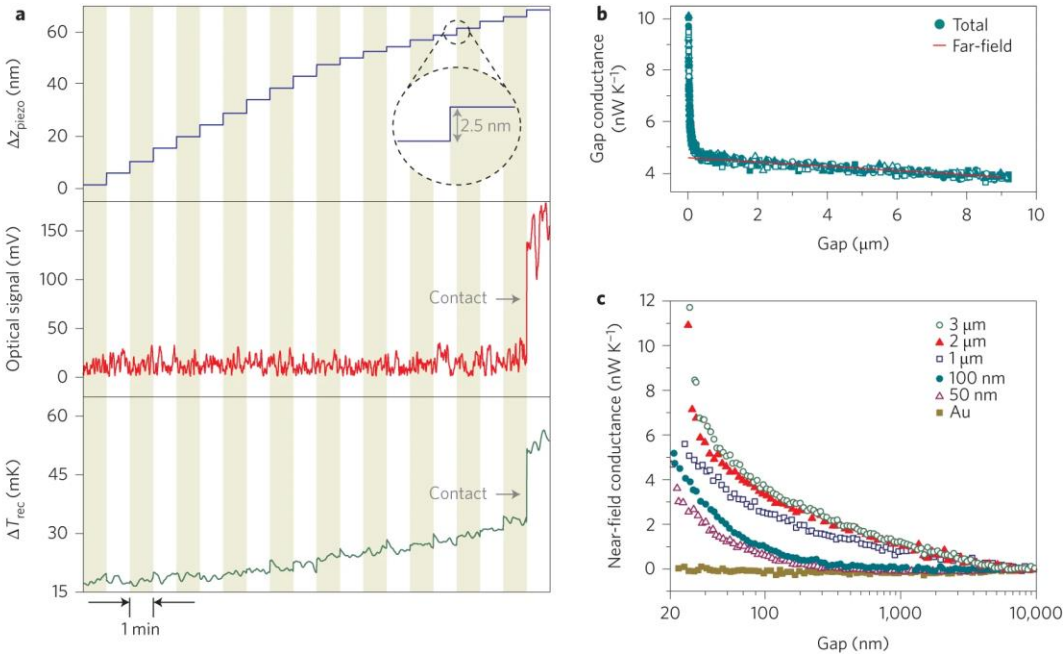

a, Simultaneous recording of displacement, Δz, of the emitter towards the receiver (top), optical contact signal (middle) and temperature increase in the receiver (bottom). During the final approach, piezo displacement steps of ~2.5 nm were used. b, Contribution of far-field radiation to the radiative thermal conductance across the gap for a representative film (100 nm). The solid red line describes the predicted far-field radiation, which increases weakly (<1 nW K−1) with decreasing gap size due to the associated change in view factor. As expected, the measured data (multiple runs, green symbols) agree well with the far-field prediction for gaps from 1 to 10 μm. c, Near-field thermal conductance as a function of film thicknesses. Data for each film thickness represent an average of ~10 different data sets. See Supplementary Fig. 7 for information about the standard deviation of the data.

Near-Field Heat Transfer (NFHT)

Thermal fluctuation dissipation theory: $$< j_l(\mathbf{r},\omega)\, j_m^*(\mathbf{r}',\omega) > = \frac{4}{\pi}\epsilon_0\epsilon''(\omega)\omega\Theta_0(\omega,T)\delta_{lm}\delta(\mathbf{r}-\mathbf{r}')$$

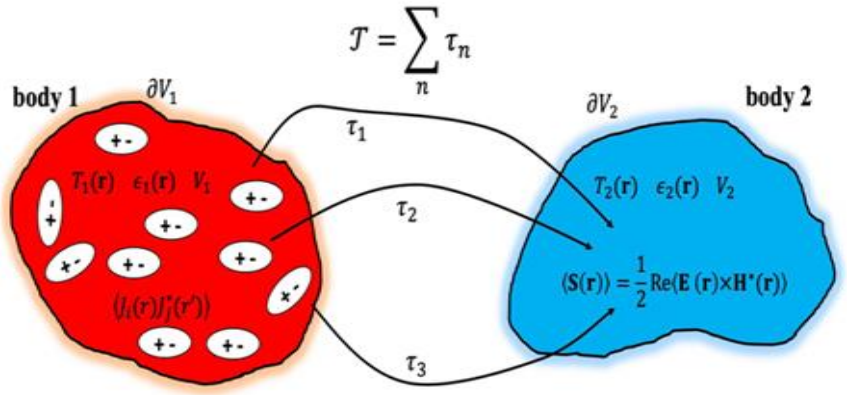

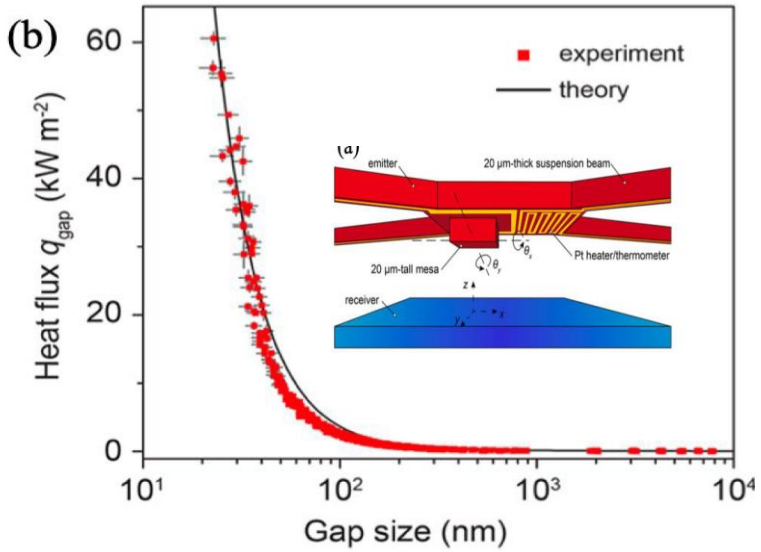

- Tunneling of evanescent waves
- Super-Planckian radiation

Near-field condition: $d << \lambda_{th} = \hbar c/k_B T$

$d >> \lambda_{tm}$

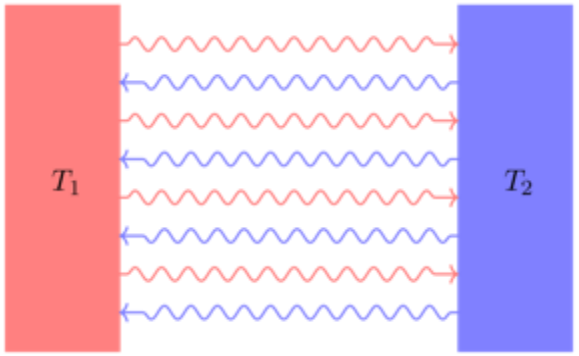

$d << \lambda_{tm}$

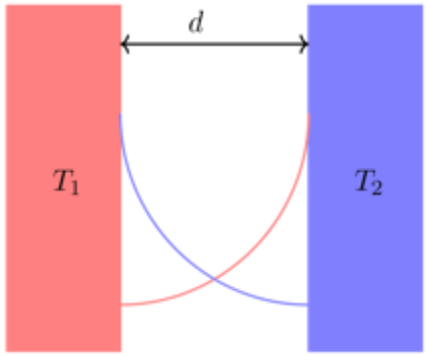

Fiorino, et al., Nat. Nanotechn. 13, 806 (2018).

T(K)	λ_{th} (μm)
1	2298.8
300	7.6
500	4.6
1000	2.3

Optical Surface Engn for Radiation

Motivation: Control thermal emission via light-matter interaction

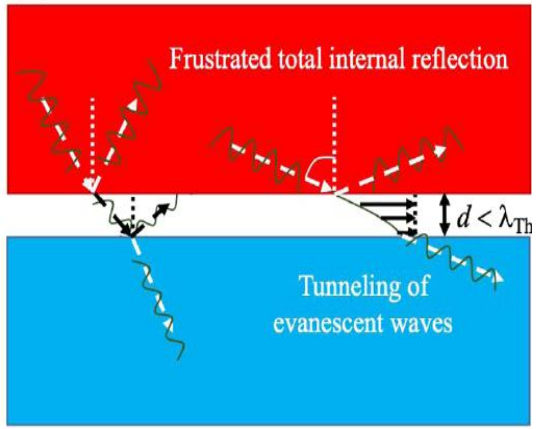

SA Biehs, et al., RMP 93, 025009 (2021)

Heat transfer possibility:

$$\tau_\alpha(\omega,\kappa,d) = \begin{cases} \dfrac{(1-|r_1^\alpha|^2)(1-|r_2^\alpha|^2)}{|D^\alpha|^2}, & \kappa < k_0, \\ \dfrac{4\mathrm{Im}(r_1^\alpha)\mathrm{Im}(r_2^\alpha)e^{-2|q_v|d}}{|D^\alpha|^2}, & \kappa > k_0, \end{cases}$$

- **Functional emission surfaces with a wavelength-scale thickness**
- **Optical surface engineering (μ, ε, surface density, harvesting, etc.)**

Metamaterials

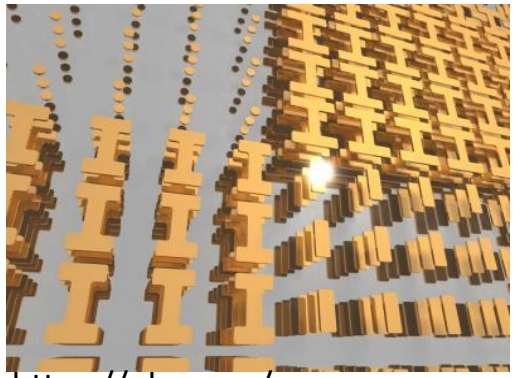

https://phys.org/news

New properties

Metasurface

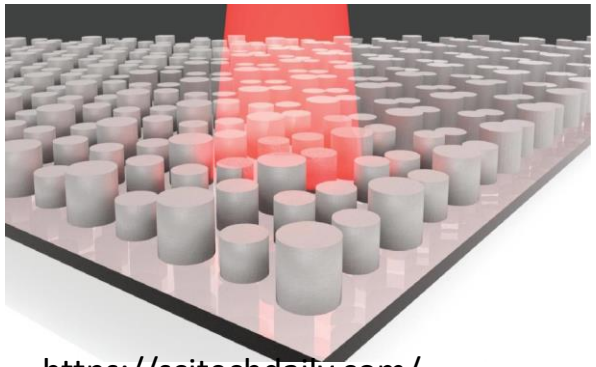

https://scitechdaily.com/

Resonance; parametric control

2D materials

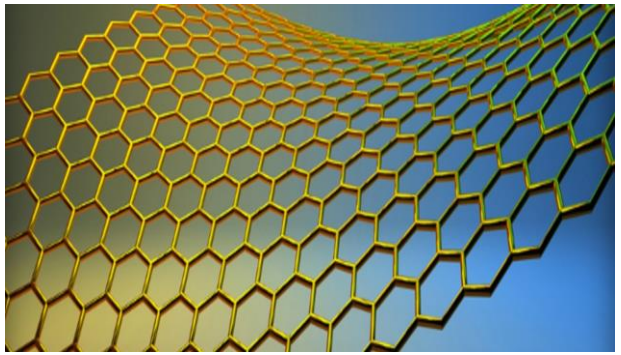

https://physics.berkeley.edu/news

Polariton, energy transfer

High Surface DOS of Natural Naterials

Near-field interaction

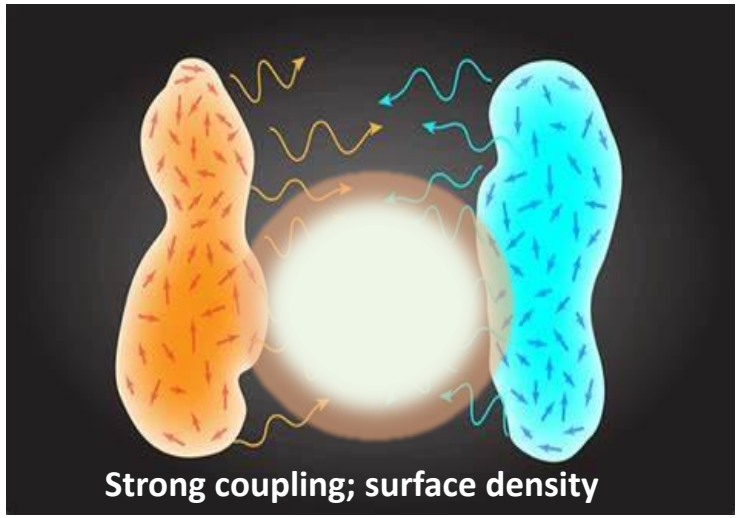

Emission spectrum

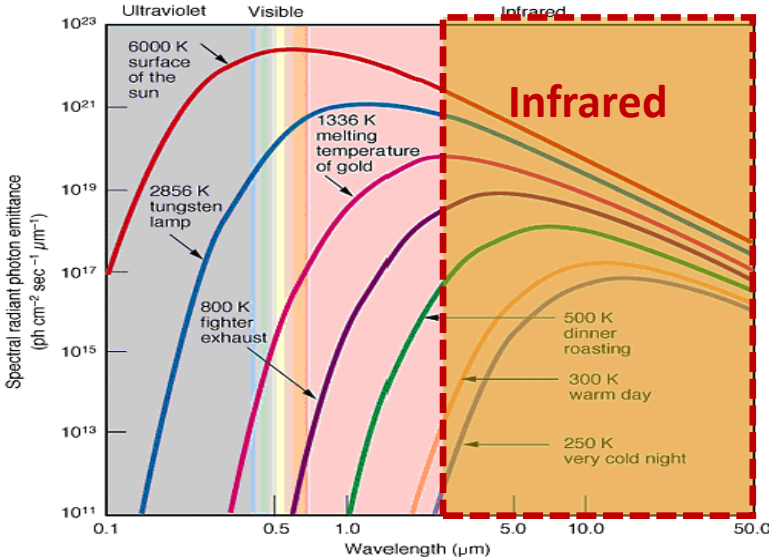

I. Plasmon/phonon polaritons
e.g., graphene, SiC,…

$$\sigma_{\text{intra}}(\omega) = \frac{\mathrm{i}e^2|E_{\mathrm{F}}|}{\pi\hbar(\omega + \mathrm{i}\tau_g^{-1})}$$

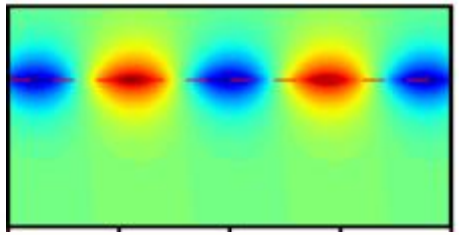

II. Hyperbolic materials: e.g., BN

$$\varepsilon_{h,\perp(\parallel)} = \varepsilon_{\infty,\perp(\parallel)} + \varepsilon_{\infty,\perp(\parallel)} \frac{\omega_{\mathrm{LO},\perp(\parallel)}^2 - \omega_{\mathrm{TO},\perp(\parallel)}^2}{\omega_{\mathrm{TO},\perp(\parallel)} - \omega^2 - \mathrm{i}\omega\gamma_{\perp(\parallel)}},$$

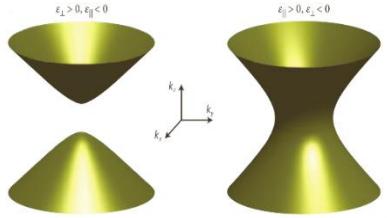

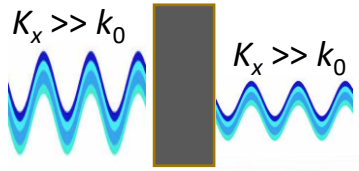

NFHT bw Monolayer Graphene Sheets

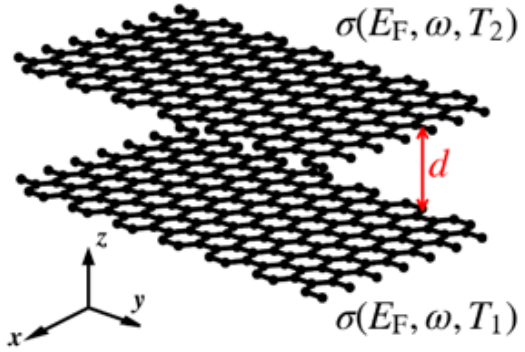

Drude model for graphene (THz to far-IR):

$$\sigma_{\text{intra}}(\omega) = \frac{\mathrm{i}e^2|E_F|}{\pi\hbar(\omega + \mathrm{i}\tau_g^{-1})}$$

Heat flux between two semi-infinite planes:

$$h(T_1, T_2, d) = \int_0^\infty \frac{\mathrm{d}\omega}{4\pi^2}[\Theta(\omega, T_1) - \Theta(\omega, T_2)] \int_0^\infty \mathrm{d}kk[\tau_s(\omega, k) + \tau_p(\omega, k)]$$

Cut-off wave number: $k_x < \pi/d$

Dispersion diagram

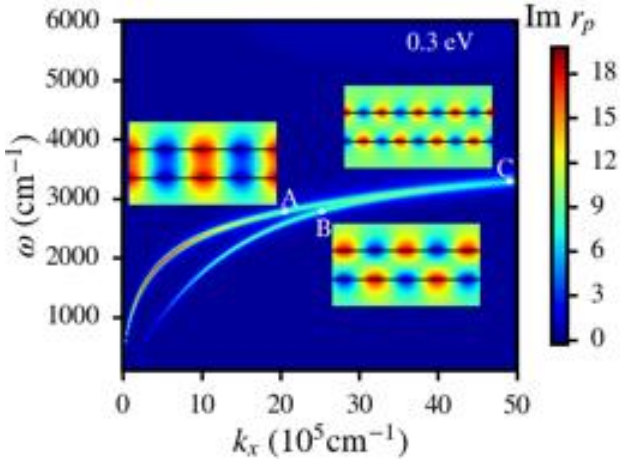

Energy transmission coefficient

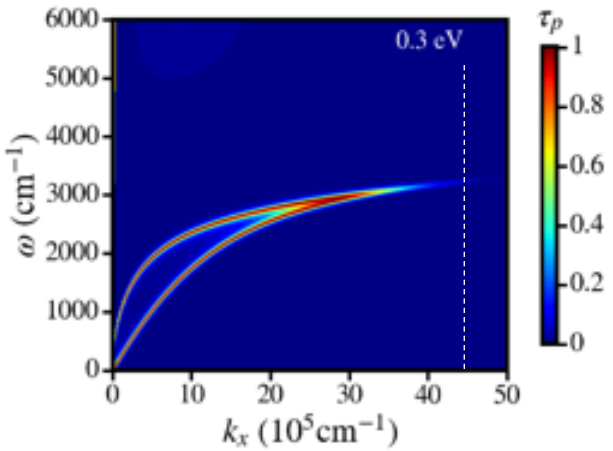

Heat flux vs gap

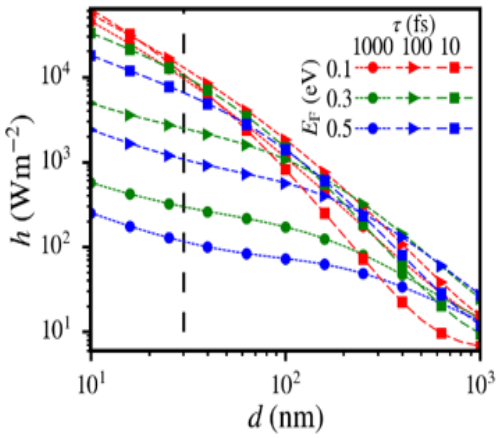

Ge Yin, et al., **Yungui Ma***, Appl. Phys. Exp. **12**, 1222001 (2016).

NFRHT bw Gra-hBN Heterostructures

Nature hyperbolic material: e.g., h-BN

$$\varepsilon_{h,\perp(\parallel)} = \varepsilon_{\infty,\perp(\parallel)} + \varepsilon_{\infty,\perp(\parallel)} \frac{\omega^2_{\mathrm{LO},\perp(\parallel)} - \omega^2_{\mathrm{TO},\perp(\parallel)}}{\omega_{\mathrm{TO},\perp(\parallel)} - \omega^2 - \mathrm{i}\omega\gamma_{\perp(\parallel)}},$$

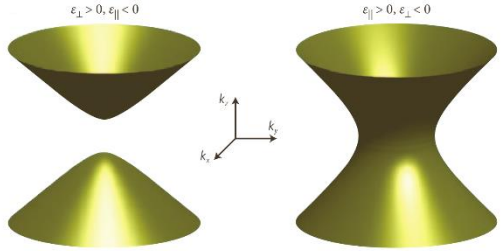

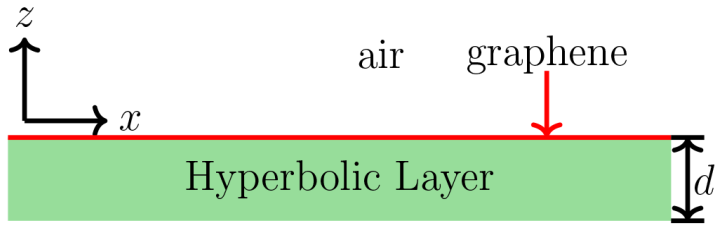

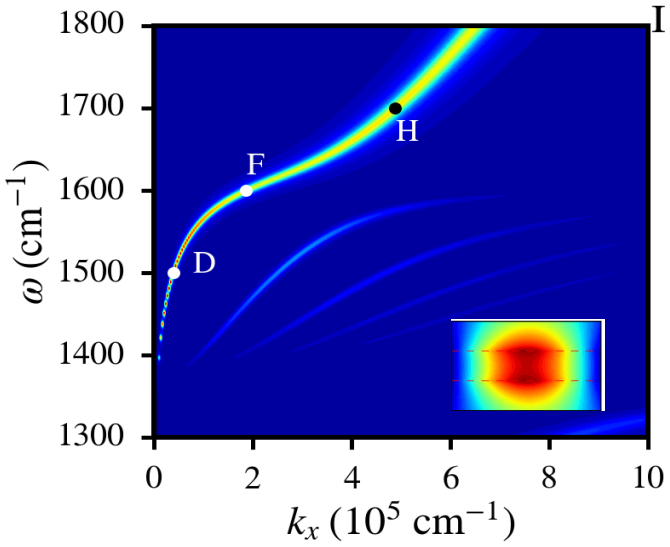

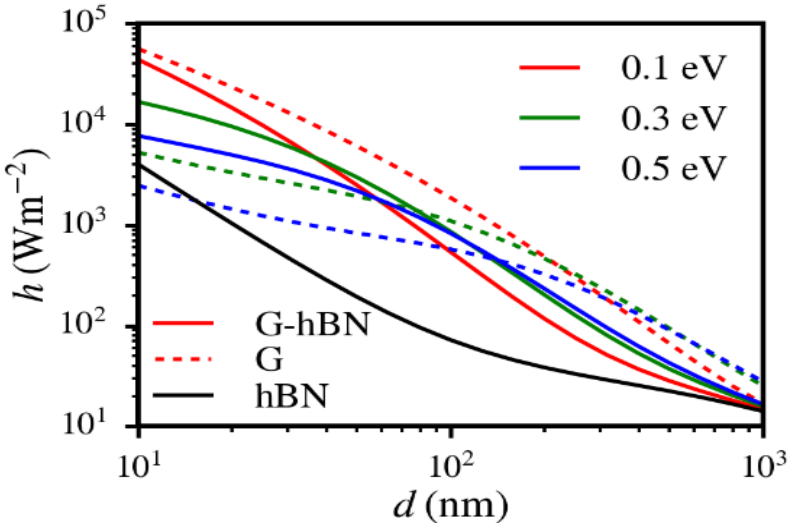

Plasmon-phonon polariton coupling could further enhance the heat flux!

Ge Yin, et al., **Yungui Ma***, Chin. Phys. B **25**, 114216 (2016)

NFRHT bw Monolayer hBN Sheets

Breakdown of optical phonons' splitting in 2D materials

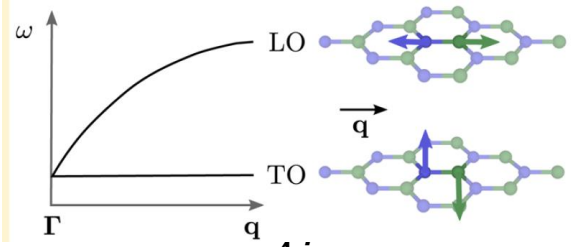

$$\sigma_{\mathrm{hBN}}(\omega) = \frac{-4i\varepsilon_0\varepsilon_{\mathrm{en}}\omega\omega_{\mathrm{TO}}v_{\mathrm{g}}}{\omega_{\mathrm{TO}}^2 - \omega^2 - i\omega\tau^{-1}}$$

F. Sohier, et al., Nano Lett 17, 3758(2017)

Transmission possibility spectrum

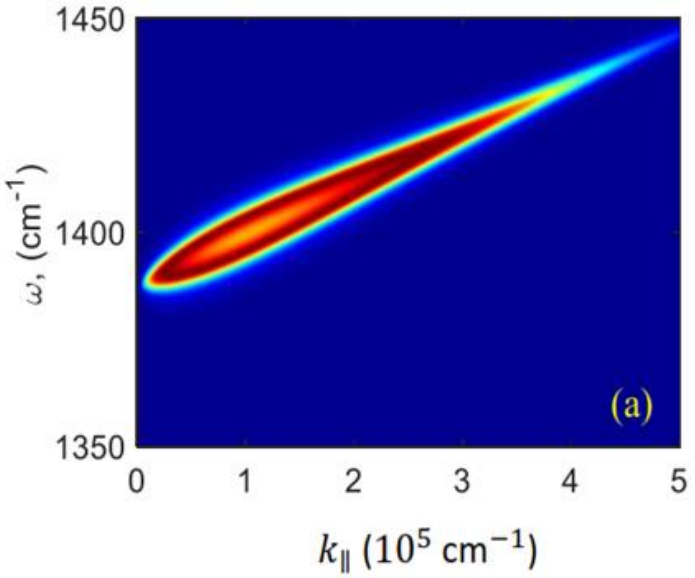

Surface DOS at z = 15 nm

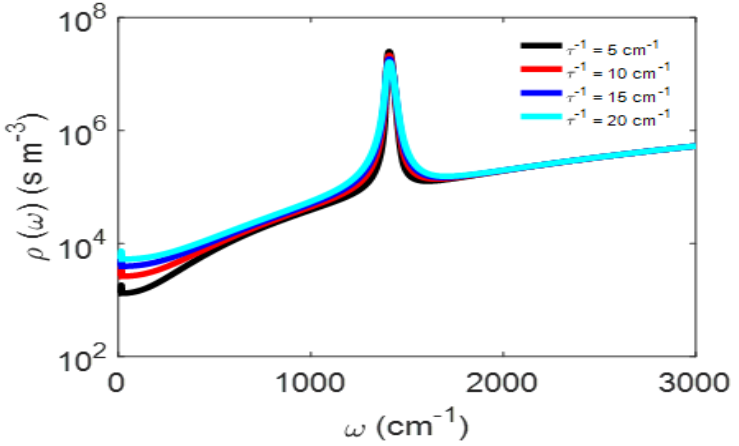

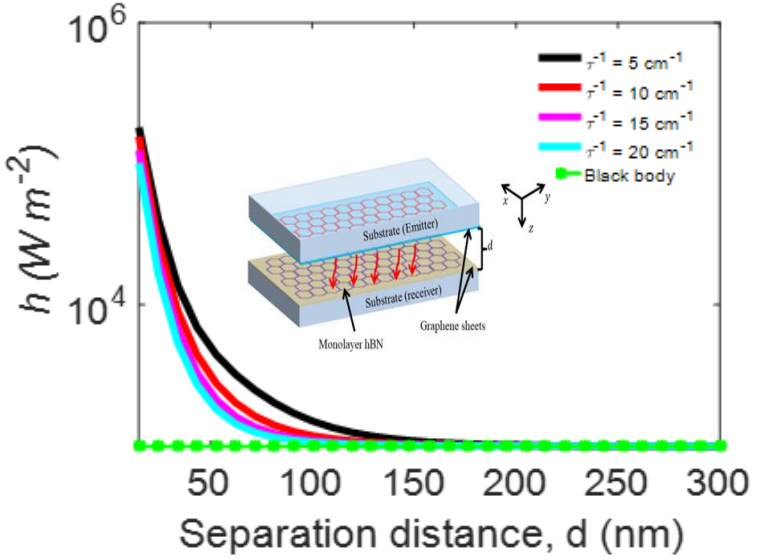

Naeem Iqbal, et al., **Yungui Ma***, International Journal of Thermal Sciences 172,107315 (2022)

Measure NFRHT bw Graphene Sheets

Schematic of measurement setup

sample area: 2 cm×2 cm

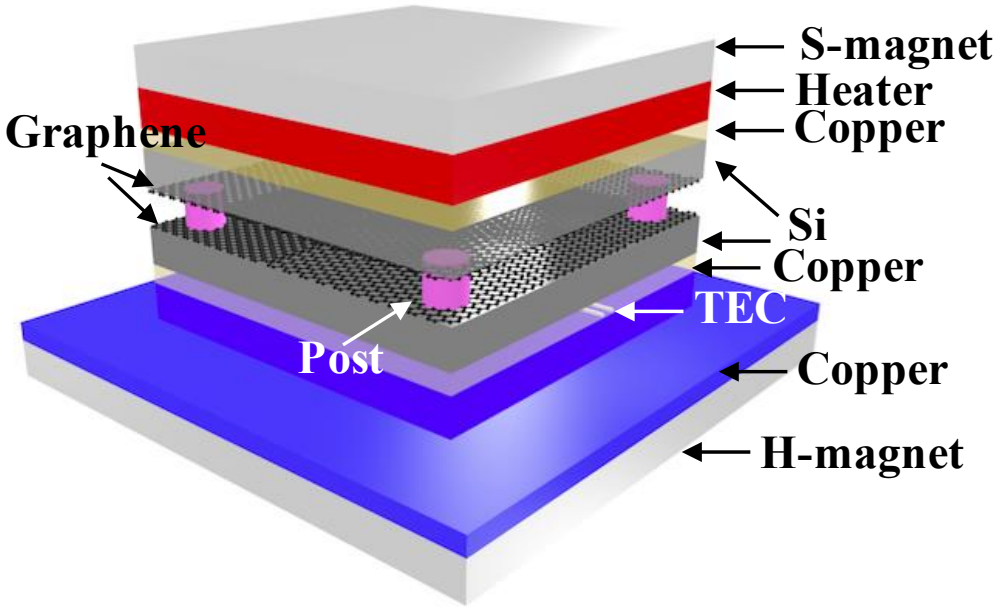

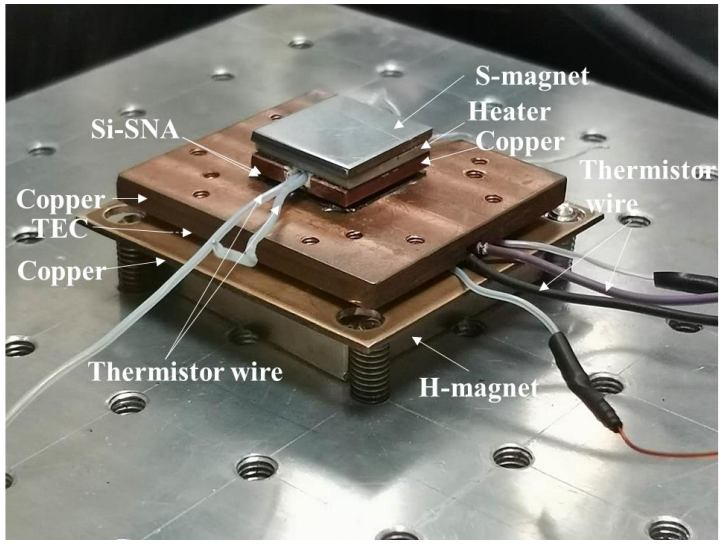

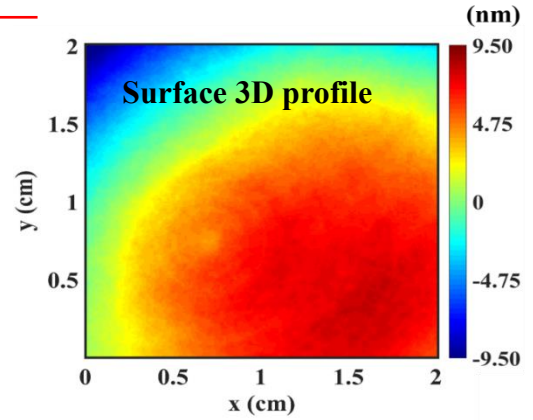

The color represents the profile variations of the wafer along the *z*-axis measured by a Laser interferometer (ZYGO OMP-035/M)

Magnet clamp + super flat
Silicon wafer + post separation

Jiang Yang, et al**., Yungui Ma***, Nature Comm. 9, 4033 (2018).

Measure NFRHT bw Graphene Sheets

(1) Measurement I: graphene on intrinsic Si

Super-Planckian near-field thermal radiation; classic theory for 2D materials!

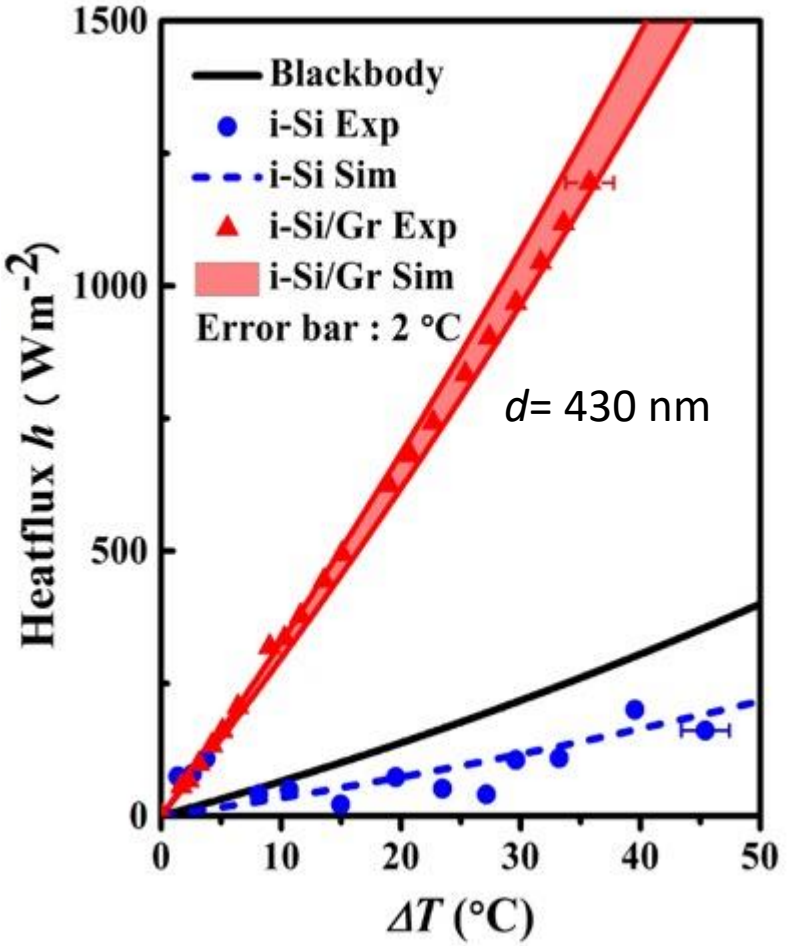

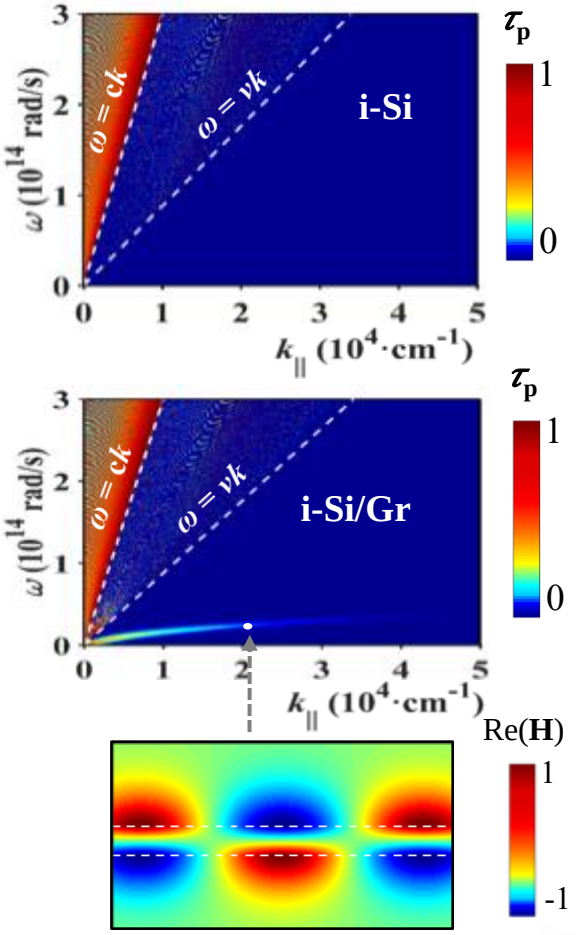

Jiang Yang, et al., **Yungui Ma***, Nature Comm. 9, 4033 (2018).

Measure NFRHT bw Graphene Sheets

Charge transfer between graphene and Si

Previous results: a Schottky junction will be formed at the interface of graphene and doped silicon, modulating the Fermi level and plasmonic properties of graphene

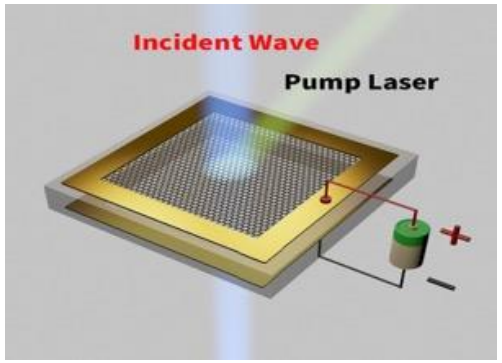

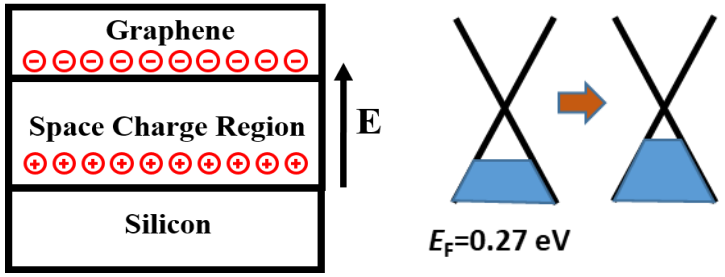

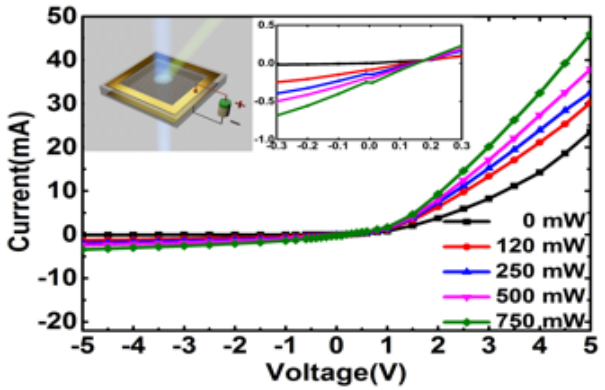

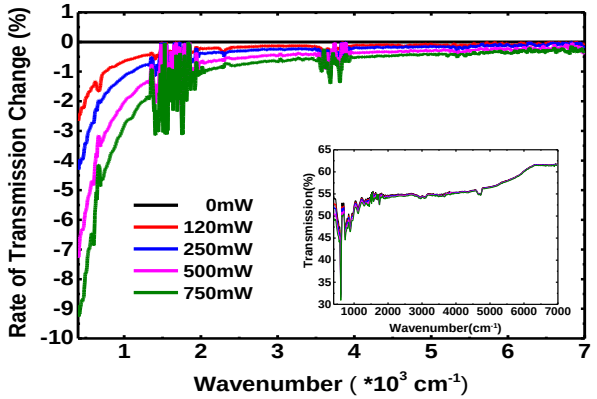

J. Yuan, et al., **Yungui Ma***, Modulation of Far-Infrared Light Transmission by Graphene-Silicon Schottky Junction, Optical Materials Express 6, 3908-3915 (2016).

Measure NFRHT bw Graphene Sheets

(2) Measurement II: graphene on doped Si

Measured heat flux

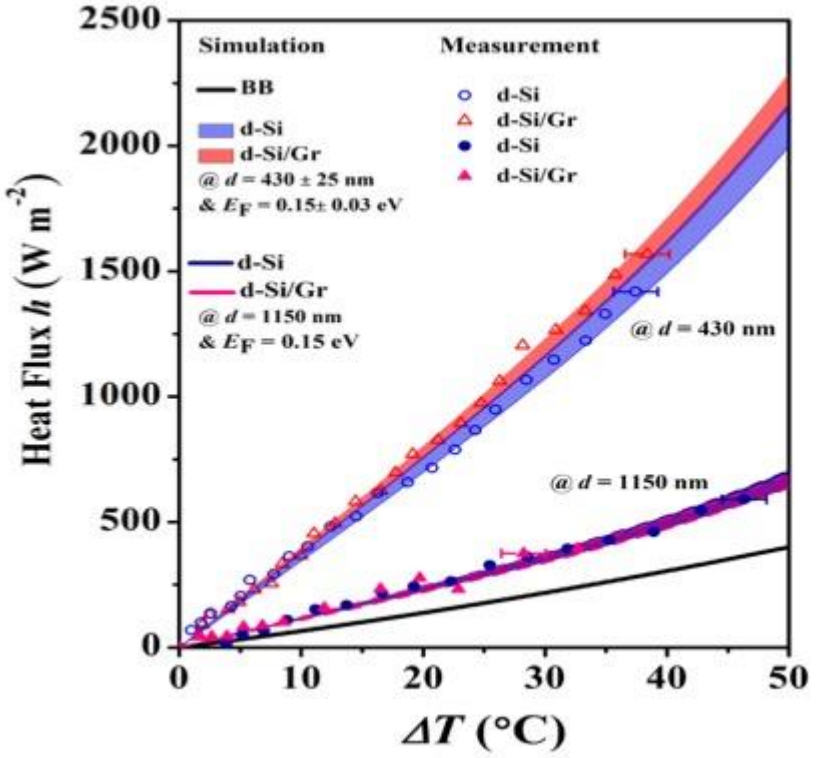

Calculated transfer possibility

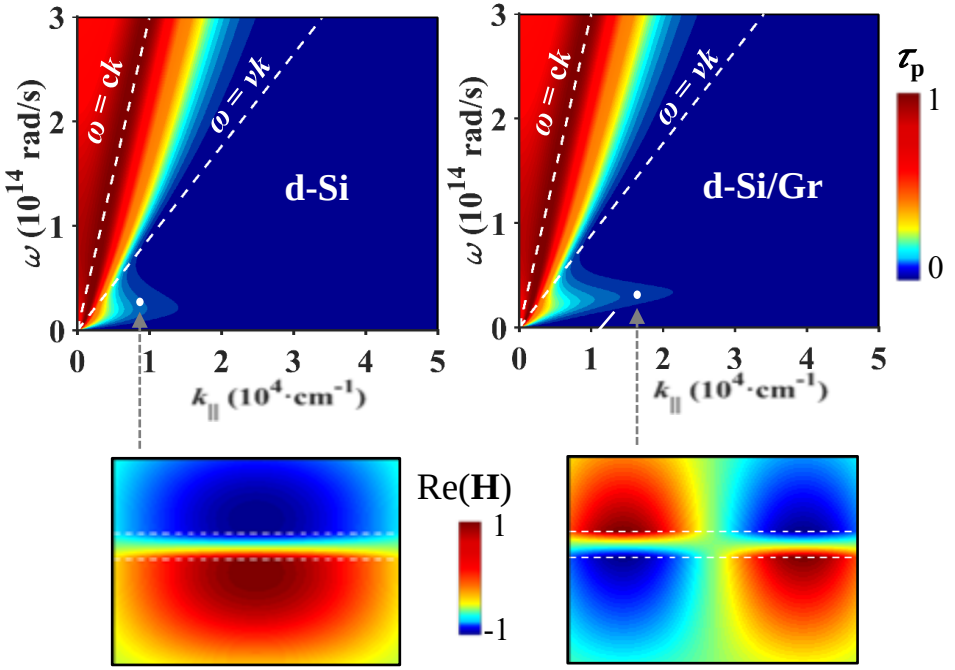

Short conclusions:

- ❖ Super blackbody radiation is found between doped silicon surfaces
- ❖ Covering the graphene layer will further enhance the heat transfer efficiency, which will become more obvious for smaller gaps.

Jiang Yang, et al., **Yungui Ma***, Nature Comm. 9, 4033 (2018).

NFRHT bw Gr-SiC Heterostructures

- SiC: support phonon polaritons with high quality (low loss) around 780 cm^{-1}
- SiC/Gr: Hybridization of phonon & photon surface modes with broadband response

All-optical measurement

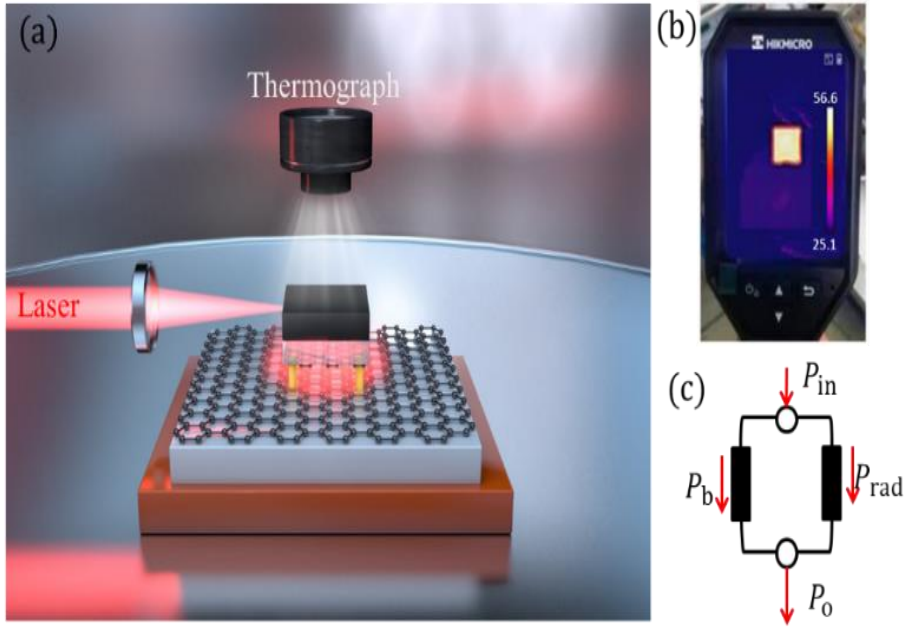

Simplified setup by all-optics

Theoretical calculation

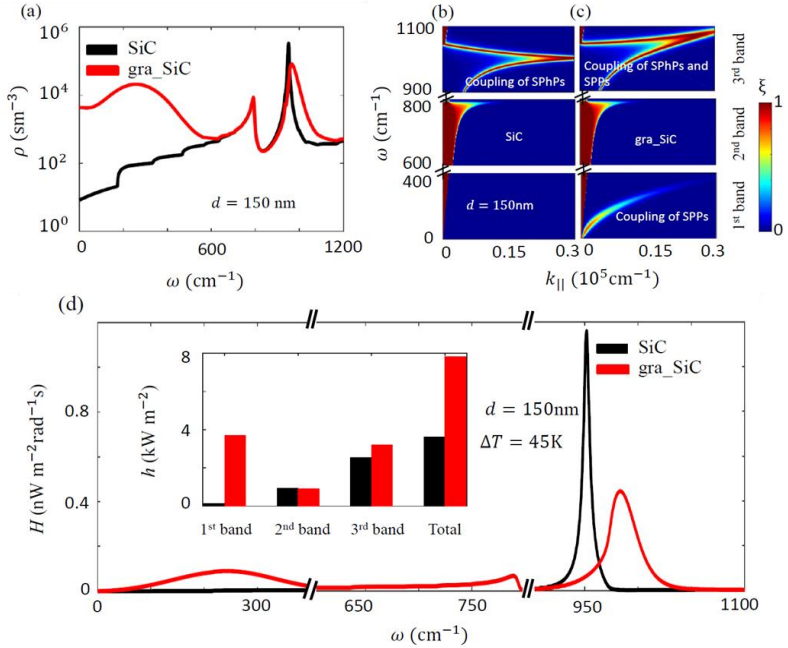

Enhanced contributions from three sub-bands

Naeem Iqbal, et al., **Jianbin Xu, Yungui Ma*,** Physical Review Applied 19, 024019 (2023).

NFRHT bw Gr-SiC Heterostructures

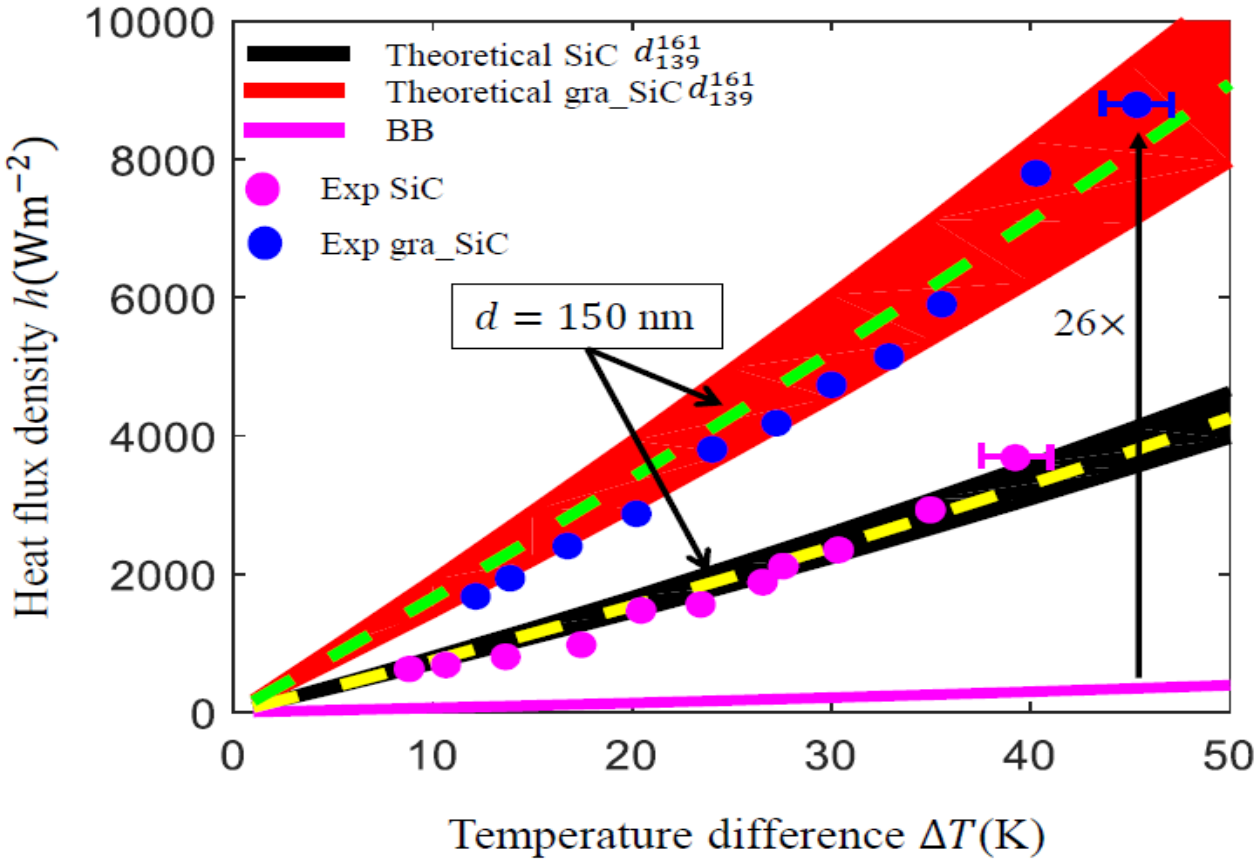

26 fold enhancement of radiation flux is obtained compared with the blackbody radiation at 150 nm! Good agreement between theory and experiment.

Naeem Iqbal, et al., **Jianbin Xu**, **Yungui Ma*,** Physical Review Applied 19, 024019 (2023).

Rapid Transient NFRHT Measurement

Question: a transient all-optical measurement is technically reliable?

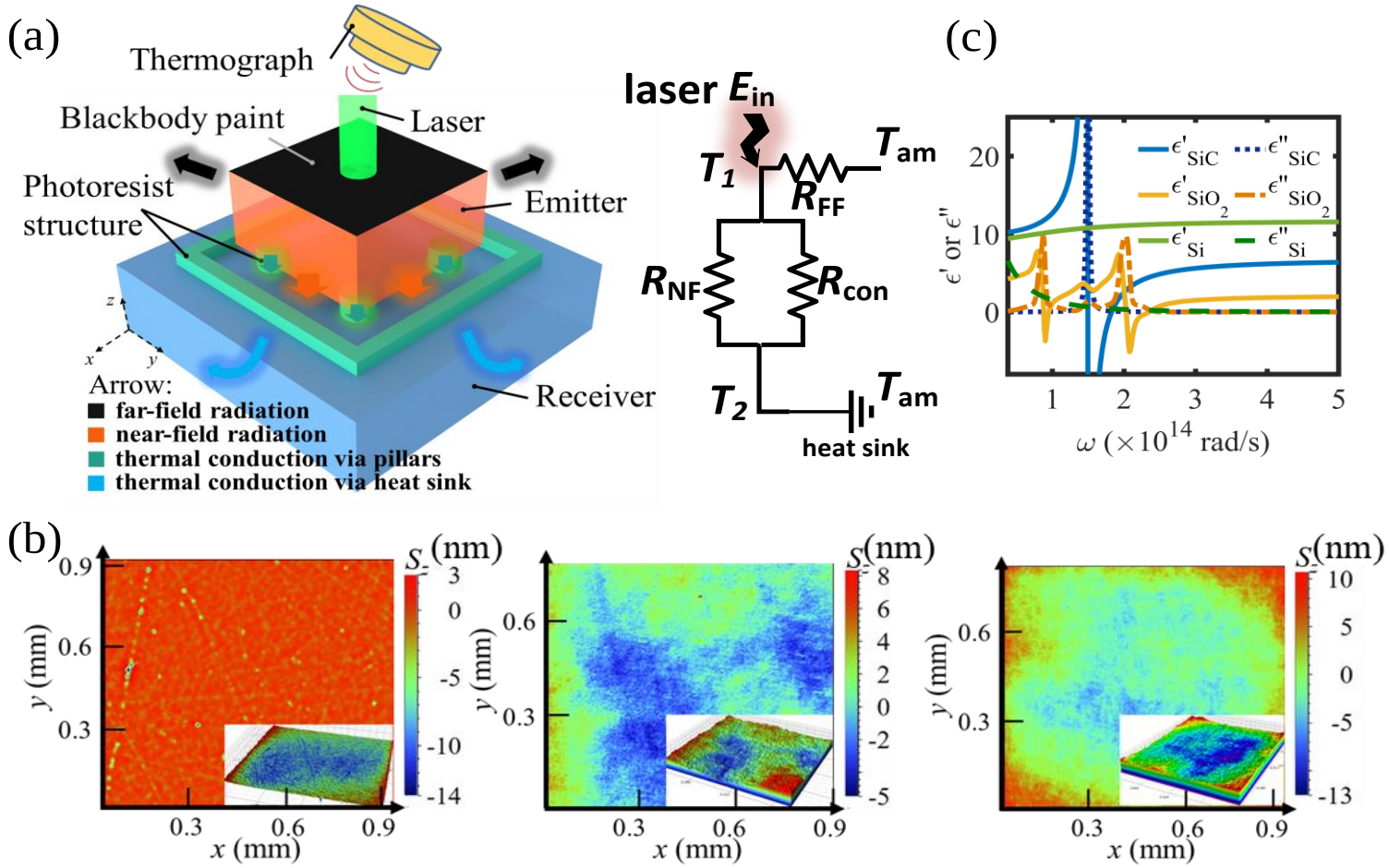

Sen Zhang, et al., Jianbin Xu and Yungui Ma*, Transient Measurement of Near-field Thermal Radiation between Macroscopic Objects, Nanoscale 16, 1167-117 (2024).

Rapid Transient NFRHT Measurement

Calibration in particular for the conduction channel

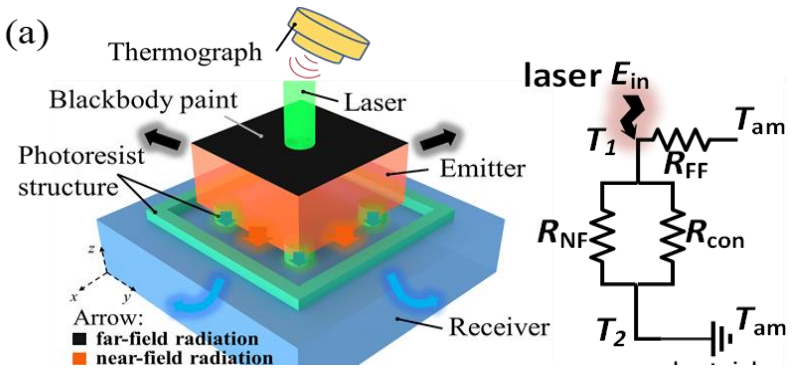

$$Q_{out}(t) \equiv c_i m_i \mathrm{d}T_1/\mathrm{d}t$$

$$Q_{out}(t) = Q_{FF}(t) + Q_{con}(t) + Q_{NF}(t)$$

$$Q_{FF} = A_{FF} \times S_{FF}\sigma(T_1^4 - T_2^4)$$

$$Q_{con} = A_{con} \times \frac{S_{con}k(T_1 - T_2)}{d}$$

$$Q_{NF} = A_{NF} \times \frac{1}{4\pi^2}\int_0^\infty [\Theta(\omega, T_1) - \Theta(\omega, T_2)]\, H(\omega, d)\mathrm{d}\omega$$

Samples:

- Single-body emitter
- Substrate/vacuum/ Al film coated substrate
- Photoresist nanopillar spacers

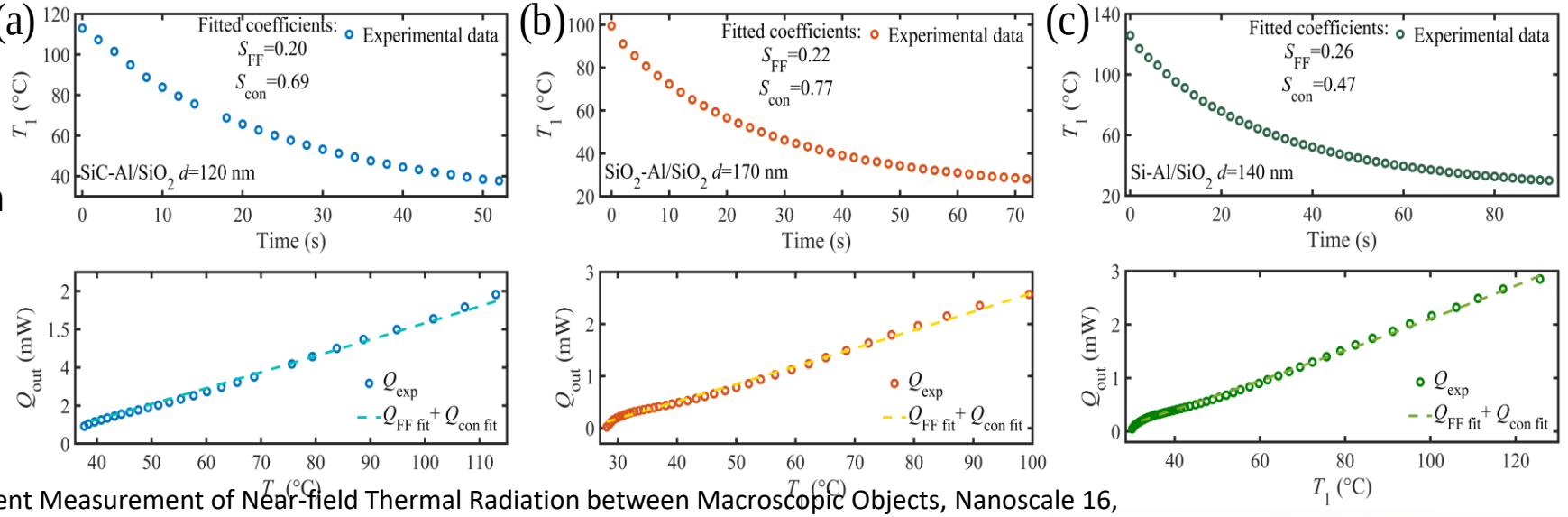

Sen Zhang, et al., Jianbin Xu and Yungui Ma*, Transient Measurement of Near-field Thermal Radiation between Macroscopic Objects, Nanoscale 16, 1167-117 (2024).

Rapid Transient NFRHT Measurement

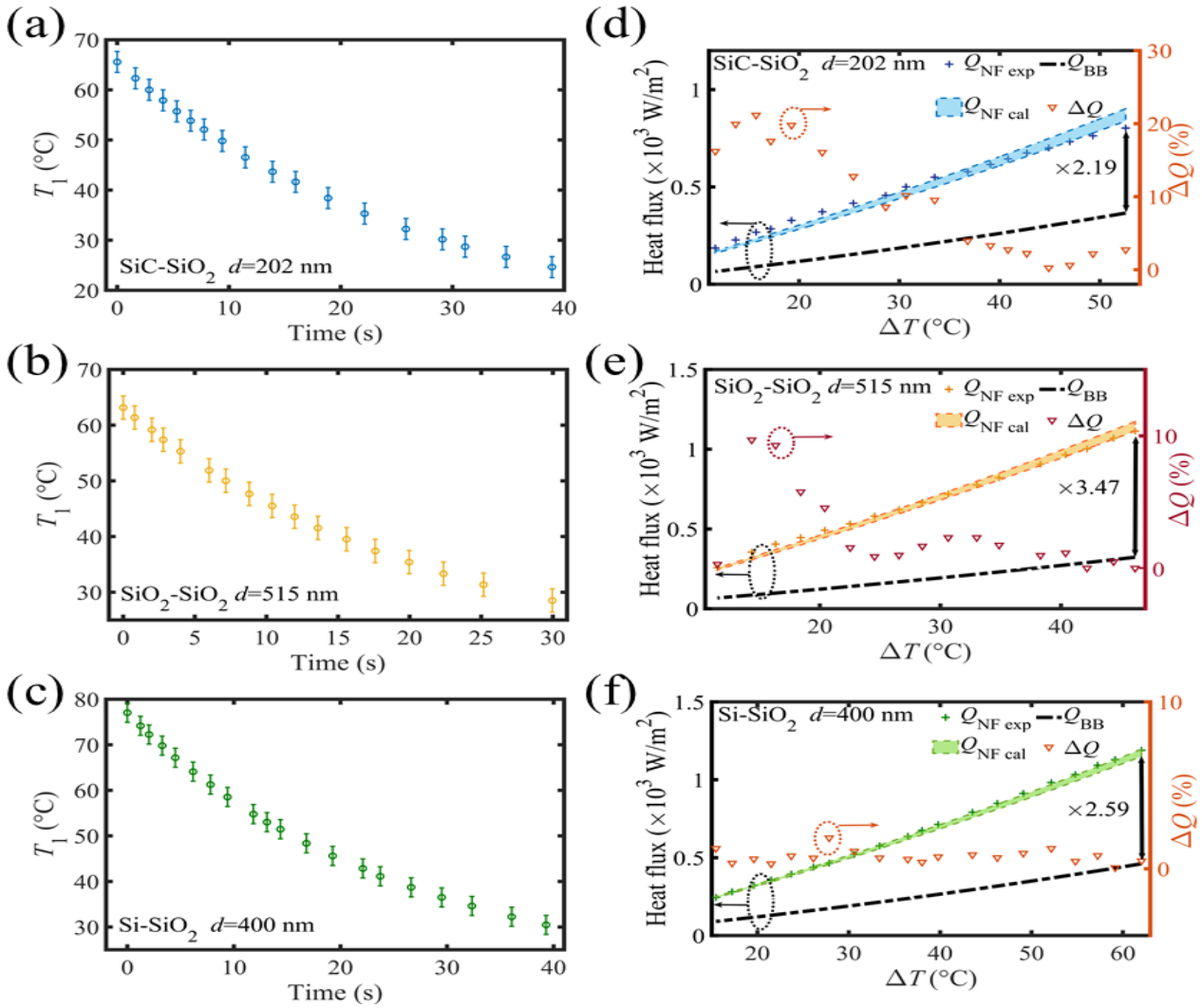

Sen Zhang, et al., Jianbin Xu and Yungui Ma*, Transient Measurement of Near-field Thermal Radiation between Macroscopic Objects, Nanoscale 16, 1167-117 (2024).

Smart Radiative *Temp* Management

- Incorporate phase-change material (VO_2) to have temperature dependent emissivity
- Able to automatically maintain the temperatures without energy consumption

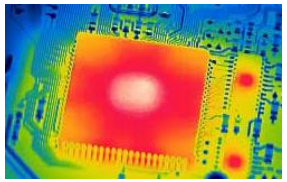

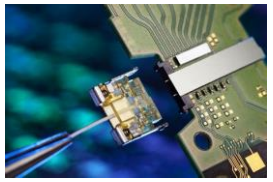

Sample structure

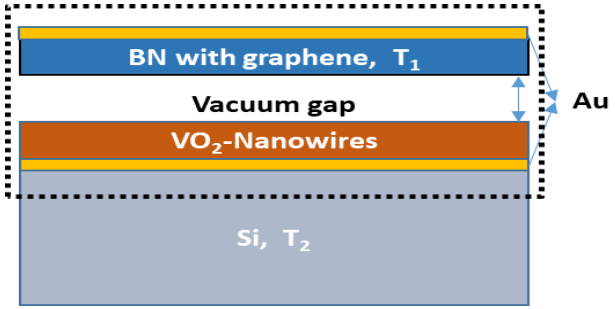

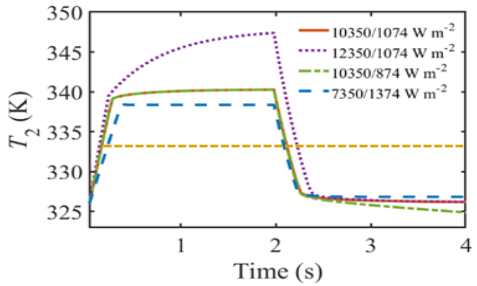

Homeostasis with one-order magnitude change of load power!

Sen Zhang, et al., **Yungui Ma***, J Appl Phys 132, 223104 (2022)

Far-field radiative smart coat

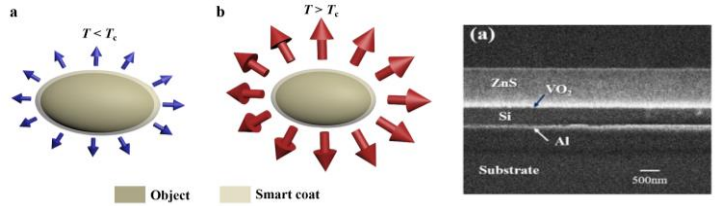

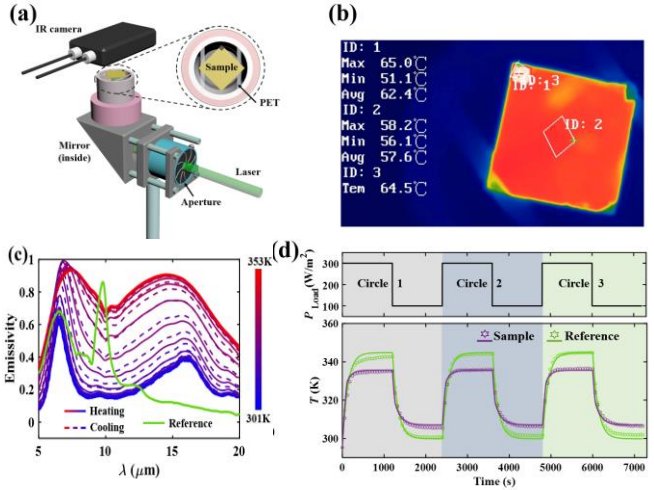

Yongdi Dang, et al., **Jianbin Xu*** and **Yungui Ma*,** Radiative Thermal Coats for Passive Temperature Management, Appl Phys Lett 123, 222201 (2023).

Radiative Thermal Transistor

Key ideas: Negative radiative thermal resistance

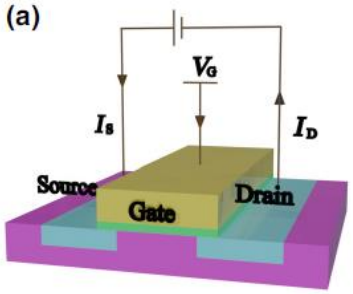

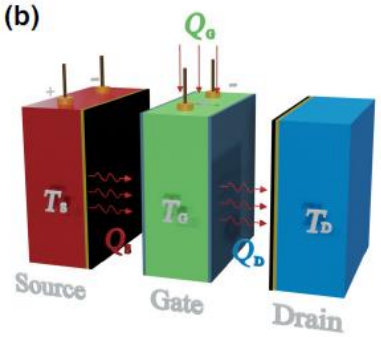

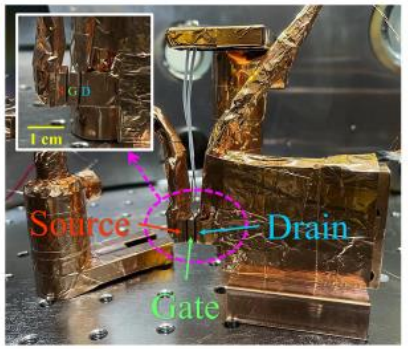

VO_2 film/Si surfaces

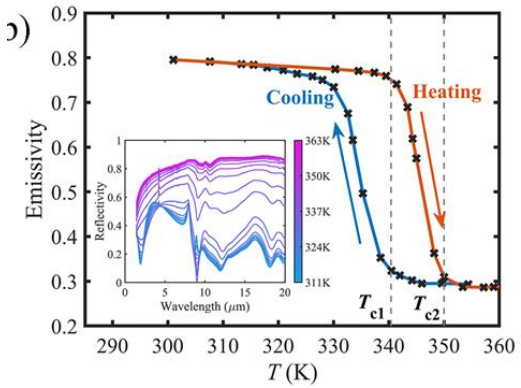

Amplification factors

$\eta_S = 14.3$ and $\eta_D = 1.7$

$$\alpha_{S,D} = \left|\frac{\partial Q_{S,D}}{\partial Q_G}\right| = \left|\frac{1}{R_{S,D}}\frac{R_S R_D}{R_S + R_D}\right|$$

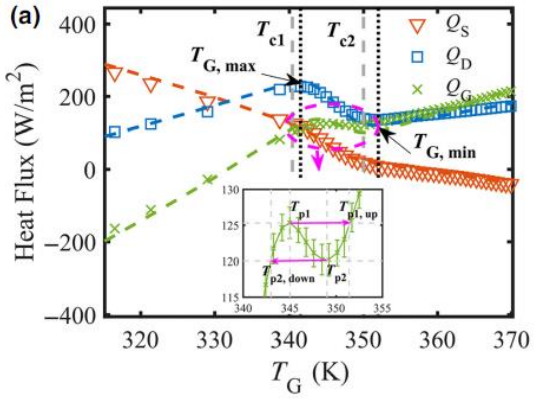

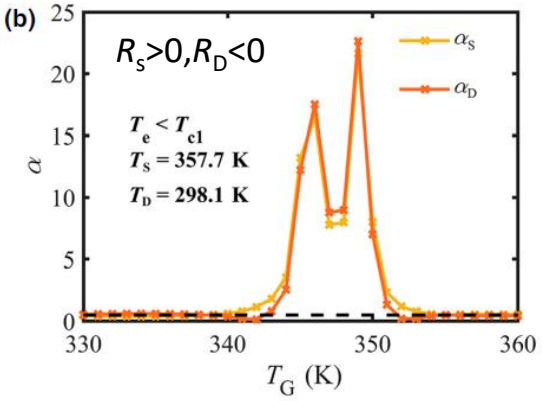

Yuxuan Li, et al., **Jianbin Xu** and **Yungui Ma***, Phys Rev Appl 20, 024061 (2023).

Radiative Thermal Transistor

Metasurfaced enabled gate design: achieve a strong heat-flux amplification; works by cooling down the gate.

$R_s<0$, $R_D>0$

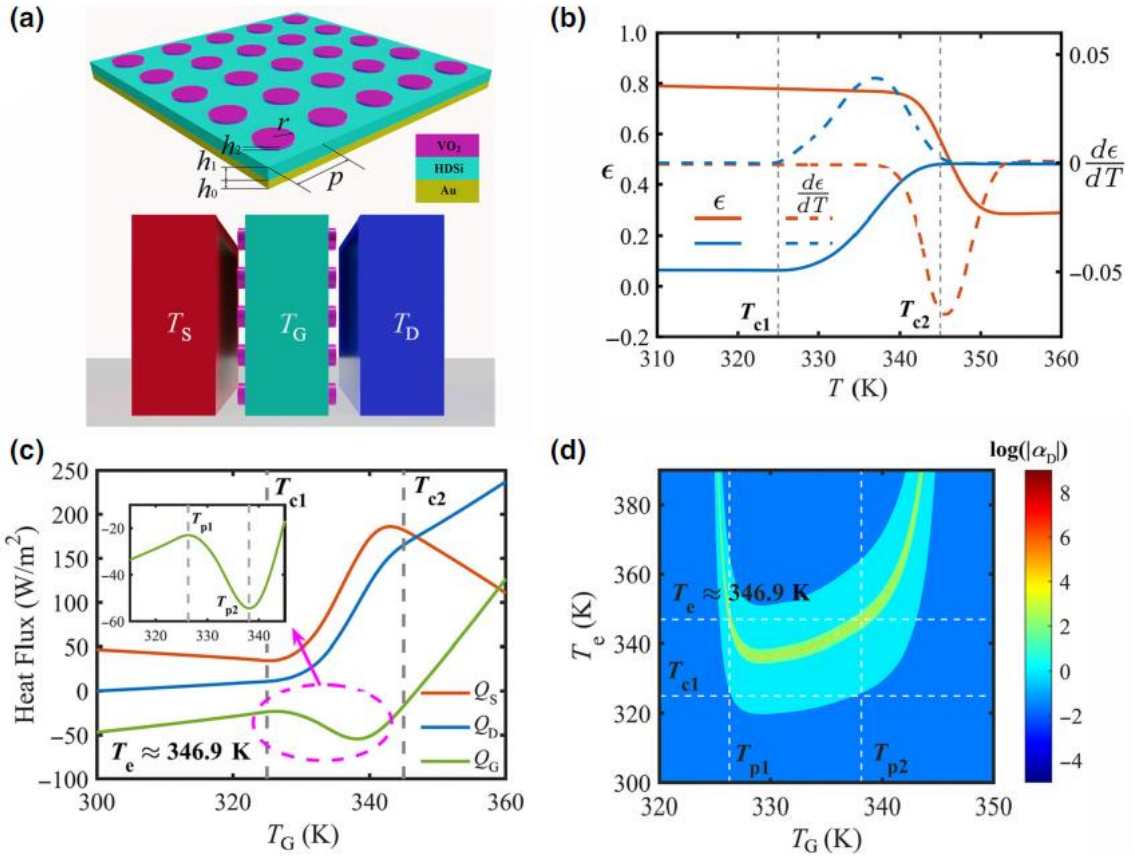

Yuxuan Li, et al., **Jianbin Xu** and **Yungui Ma*,** Phys Rev Appl 20, 024061 (2023).

Summary & Outlook

- A historical overview of near-field radiative heat transfer (NFRHT) has been deliberated from a personal viewpoint, by connecting several key conjunctures through personal interactions, particularly via progress of nanotechnology and nanofabrication
- Recent results of NFRTH in 2D materials are articulated
- New measurement techniques are developed via extensive optics
- NFRHT between artificial surfaces are experimentally characterized
- Potential applications in temperature management and logic thermal elements are explored
- Perspectives: NFRTH in twisted photonic structures, NF-to-FF superlens, radiative motor, nonreciprocal radiation, ……

Tang, L., Corrêa, L.M., Francoeur, M. et al. Corner- and edge-mode enhancement of near-field radiative heat transfer. Nature (2024), https://doi.org/10.1038/s41586-024-07279-2, https://www.nature.com/articles/s41586-024-07279-2

A few Books and Reviews on NFRHT

1. K. Joulain, J. P. Mulet, F. Marquier, R. Carminati, Jean-Jacques Greffet, Surface electromagnetic waves thermally excited: Radiative heat transfer, coherence properties and Casimir forces revisited in the near field, Surface Science Reports, 57 (3-4), 59-112 (May 2005); DOI10.1016/j.surfrep.2004.12.002

2. A. I. Volokitin, and B. N. J. Persson, Near-field radiative heat transfer and noncontact friction, Reviews of Modern Physics, 79 (4), 1291-1329 (Oct-Dec 2007)

3. A. I. Volokitin, and B. N. J. Persson, Electromagnetic Fluctuations at the Nanoscale, Springer, 2017

4. Zhuomin M. Zhang, Nano/Microscale Heat Transfer, Springer 2020, 2nd Ed.; 2007, 1st Ed.

5. Y. Li, W. Li, C. W. Qiu, et al., Transforming heat transfer with thermal metamaterials and devices, Nature Materials Review, 6 (6), 488-507 (2021)

6. J. Chen, X. F. Xu, J. Zhou, B. W. Li, Reviews of Modern Physics 94, APRIL–JUNE 2022

7. M. Pascale, M. Giteau, G. T. Papadakis, Perspective on near-field radiative heat transfer, Appl. Phys. Lett. 122, 100501 (2023)

Acknowledgement

- Funding Support from AoE/P701/20 highly appreciated

Postdocs and Students:

Dr. Z. F. Chen
Dr. F. H. Shen
Dr. J. W. Ma
Dr. X. Bai
Mr. J. S. Zhu
Ms. X. Y. Zhao

Postdocs and Students:

Dr. Naeem Iqbal
Dr. Ge Yin
Mr. Shen Zhang
Mr. Yongdi Dang
Ms. Yuxuan Li
Ms. Xinran Li
Ms. Wei Du
Mr. Jiang Yang
Mr. Yang Fu

Collaborators:

Prof. Yungui Ma, ZJU
Prof. Philippe Ben-Abdallah, CNRS
Prof. Bing-Feng Ju, ZJU

Hong Kong PhD Fellowship Scheme

Established by the Research Grants Council (RGC) in 2009, the **Hong Kong PhD Fellowship Scheme (HKPFS)** aims at attracting the best and brightest students in the world to pursue their PhD programmes in Hong Kong's universities.

Website

www.gs.cuhk.edu.hk/hkpfs

CUHK Vice-Chancellor's HKPFS Scholarship

Tuition Fee Waiver
for the whole normative study period

Stipend
Up to HK$1.32 Million*
(approx. US$169,840)

Lodging Award
Up to HK$100,000*#
(approx. US$12,800)

Conference and Research-related Travel Allowance
Up to HK$85,200*
(approx. US$10,923)

1st Year Hostel Fee Waiver
and Guaranteed On-campus Accommodation*^

Totalling

up to HK$ 1.72 Million (~US$221,000)
financial assistance during the normative study period

* During the student's normative study period.
^ HKPFS awardees who submit hall applications and complete registration procedures in a timely manner.
# An award of HK$40,000 for lodging in the first year of study and HK$20,000 in subsequent years during the normative study period.

Hong Kong PhD Fellowship Scheme

Eligibility

Candidates who are seeking admission as new full-time PhD students in Hong Kong universities funded by the University Grants Committee (UGC), irrespective of their country of origin, prior work experience and ethnic background, are eligible to apply.

Timeline

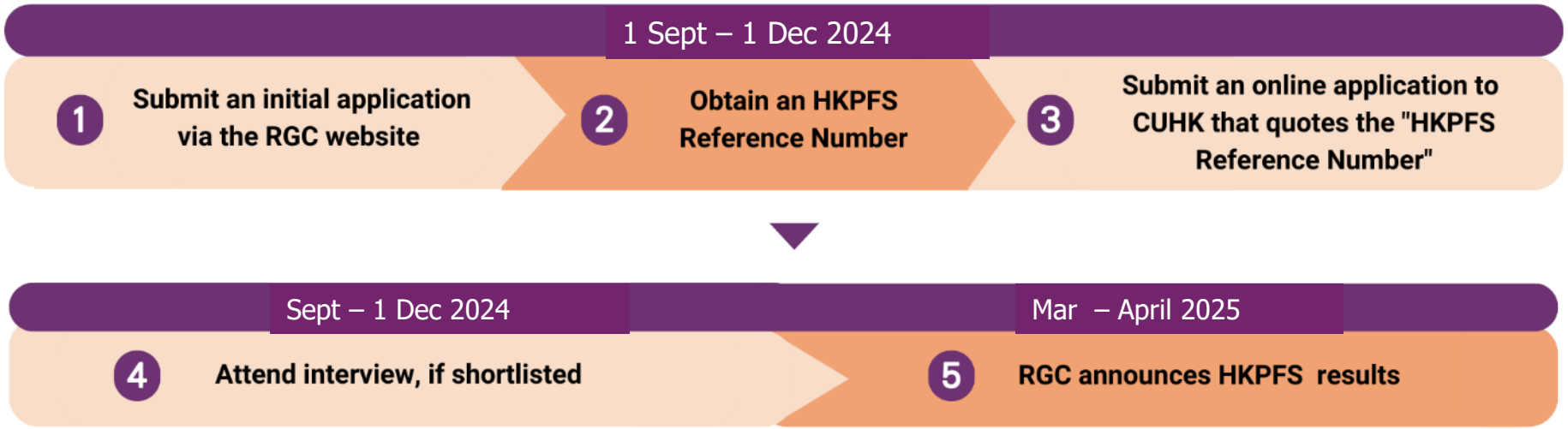

Chinese University of Hong Kong

香港中文大學